WWW.AMPELMANN.NL

Master of Science Thesis

Design of a lightweight FRP T-boom for an offshore gangway, and development of a fatigue model for prediction of its service life

Koushik Subramanian

Faculty of Aerospace Engineering · Delft University of Technology

Design of a lightweight FRP T-boom for an offshore gangway, and development of a fatigue model for prediction of its service life

Master of Science Thesis

For obtaining the degree of Master of Science in Aerospace Engineering
at Delft University of Technology

Koushik Subramanian

20 May 2016

Faculty of Aerospace Engineering · Delft University of Technology

The work in this thesis was supported by Ampelmann Operations. Their cooperation is gratefully acknowledged.

Copyright © Koushik Subramanian
All rights reserved.

Delft University of Technology
Faculty of Aerospace Engineering
Department of Aerospace Structures and Materials

GRADUATION COMMITTEE

Dated: 20 May 2016

Chair holder:

Dr. Christos Kassapoglou

Committee members:

Dr. Dimitrios Zarouchas

Ir. Koen van Valkenhoef

Dr. Miguel A. Gutiérrez

Dr. ir. Sonell Shroff

Executive Summary

The high stiffness to weight ratio of Fibre Reinforced Polymer (FRP) or composites have been beneficially utilized in improving the performance and reducing the weight of various structures conventionally designed using metals. Recently, composites have found their use in design of more than 100-m long wind turbine blades because of their high stiffness to weight ratio leading to an equally strong, but possibly longer wind turbine blade. Another such application is the gangway of the Ampelmann system used to transfer personnel safely from and to the offshore platform at sea.

The Ampelmann system uses a stabilized gangway to facilitate the safe and easy transfer of personnel from and to the offshore structure. The existing gangway is a steel truss based structure. It is anticipated that by substituting steel with composites, a significantly lighter and more durable design can be made. The focus of this thesis is a composite design of the Telescoping boom (T-boom) of the Ampelmann gangway GXL, and, and predict its life time by adapting a fatigue model for an offshore environment.

The first phase of the project involves a preliminary composite based design of this T-boom, by studying various design concepts and material systems applicable for the structure. This involves challenges such as the lack of standards for composite designs, the certification problems associated with offshore composite parts; the varying, random nature of the service loads, and the harsh operational environment. Since there are no applicable standards for an offshore composite gangway, FRP bridge design specifications are used to determine certain design requirements. A static finite element analysis and dynamic analysis of the composite T-boom is subsequently performed to determine whether the structure satisfies the design requirements.

Following this, a fatigue model is adapted to predict the life of the composite T-boom. Because the structure will operate in an offshore environment, this task presents two difficulties. Firstly, the load spectra dictating fatigue behaviour are varying and random. Secondly, most fatigue models do not incorporate the effect of conditions like temperature extremes, humidity, and exposure to UV radiation. In an offshore environment, the effect of these factors on the fatigue life cannot be ignored. Hence, a modified version of the Kassapoglou's model which considers the effect of moisture and temperature, is developed. The advantage of the modified Kassapoglou's model is that it is simple and requires minimal experimental effort.

The new design resulted in a preliminary weight and cost savings of 45% and 38% respectively, as compared to the original steel-based truss structure. Due to certain limitations of the fatigue model, the fatigue life of T-boom in not estimated in the study. The significance of this thesis is twofold namely a) it bridges the knowledge gap of the use of composites in an offshore environment b) a first of its kind modified fatigue model incorporating the effects of moisture and temperature is developed.

Table of Contents

List of Acronyms **xxi**

List of Symbols **xxiii**

Acknowledgments **xxvii**

1 Introduction **1**

1.1 Ampelmann system : An overview 1

1.2 Composite gangway: Benefits and challenges 3

1.3 Core requirements of Ampelmann 3

1.3.1 Research objective 4

1.4 Master thesis: Workflow 4

1.5 Readers guide 5

2 Literature study **7**

2.1 Gangway: Existing design 7

2.2 Preliminary load cases for the composite T-boom 8

2.2.1 Normal Operation- Starting/Ending (NO-SE) 9

2.2.2 Normal Operation- People Transfer (NO-PT) 9

2.2.3 Normal Operation- Cargo Transfer (NO-CT) 9

2.2.4 Emergency Operation- 3 People Transfer (EO-3PT) 9

2.2.5 Emergency Operation- Extra Length + Cargo (EO-ELC) 9

2.2.6 Stowed Condition (SC) 9

2.3 Load spectra for the composite T-boom 10

2.4 Composite gangway : Design concepts 11

2.5 Composite gangway : Design requirements 13

2.5.1 Deflection . . . 13
2.5.2 Design life . . . 14
2.5.3 Strength . . . 14
2.5.4 Durability . . . 14
2.5.5 Safety factor . . . 14
2.5.6 Vibration . . . 14
2.6 Failure modes and stiffness of FRP beams . . . 15
2.6.1 Axial and bending stiffness . . . 15
2.6.2 Column buckling . . . 17
2.6.3 Crippling . . . 18
2.6.4 Material failure . . . 19
2.7 Fatigue : Composites versus metals . . . 20
2.8 Composite : Fatigue models . . . 20
2.8.1 Progressive damage models . . . 20
2.8.2 Phenomenological models . . . 21
2.9 Material system and material characterization tests . . . 23
2.9.1 Moisture absorption properties . . . 24
2.9.2 Data pooling . . . 24
2.10 Research questions and sub-goals . . . 25
2.11 Chapter summary . . . 26

3 Methodology 27
3.1 Preliminary design of the composite T-boom . . . 27
3.1.1 Material system . . . 29
3.1.2 Cost implication . . . 29
3.1.3 Design guidelines/ Rules of thumb . . . 30
3.1.4 Design strategy . . . 31
3.2 Finite Element (FE) analysis of the composite T-boom . . . 33
3.3 Detailed analysis of the composite T-boom . . . 38
3.3.1 Global deflection of the gangway . . . 39
3.3.2 Natural frequency of the gangway in bending . . . 40
3.3.3 Global column buckling load of the composite T-boom . . . 41
3.4 Material characterization tests . . . 42
3.4.1 Moisture ingression test . . . 42
3.4.2 Tensile and compression test . . . 43
3.4.3 Data pooling method . . . 44
3.5 Modified Kassapoglou's model . . . 45
3.6 Chapter Summary . . . 47

4 Results and Discussion 49

4.1 Preliminary design results . . . 49
4.1.1 Axial stiffness estimation . . . 51
4.1.2 Bending stiffness estimation . . . 51
4.1.3 Buckling modulus estimation . . . 52
4.1.4 Mass estimation . . . 52
4.2 FE analysis results . . . 53
4.2.1 SC results . . . 54
4.2.2 EO-3PT results . . . 56
4.2.3 EO-ELC results . . . 58
4.2.4 Local buckling . . . 60
4.3 Detailed analysis . . . 61
4.3.1 Global deflection of the gangway . . . 61
4.3.2 Natural frequency of the gangway . . . 63
4.3.3 Global buckling of the composite T-boom . . . 64
4.4 Material characterization test results . . . 65
4.4.1 Moisture ingression test results . . . 65
4.4.2 Compression test results . . . 66
4.4.3 Tension test results . . . 66
4.5 Data pooling results . . . 67
4.5.1 Pooled compressive strength degradation curve . . . 67
4.5.2 Pooled tensile strength degradation curve . . . 68
4.6 Ideal S-N curves . . . 70
4.6.1 S-N curve for Tension-Tension (T-T) fatigue . . . 70
4.6.2 S-N curve for Compression-Compression (C-C) fatigue . . . 70
4.7 Modified Kassapoglou's model results . . . 71
4.7.1 Modified S-N curves for T-T fatigue . . . 72
4.7.2 Modified S-N curves for C-C fatigue . . . 72
4.8 Constraints in fatigue life estimation . . . 74
4.8.1 Fatigue model proposal to account the multi-axial stress state . . . 75
4.9 Cost estimation . . . 76
4.9.1 Production cost . . . 76
4.9.2 Labour installation cost . . . 76
4.9.3 Inspection cost . . . 77
4.9.4 Repairs . . . 77
4.9.5 Certification cost . . . 77
4.10 Chapter Summary . . . 78

5 Conclusions and recommendations 79
5.1 Conclusions . . . 79
5.2 Recommendations . . . 81

References **83**

A Existing T-boom design **89**
- A.1 Existing gangway GXL arrangement . . . 89
- A.2 Cross-section details of the existing T-boom . . . 89
- A.3 Bending stiffness of the existing T-boom . . . 93

B Technical data sheet : Hexcel **95**

C Preliminary design : Matlab code **103**
- C.1 Matlab algorithm . . . 103

D Composite T-boom design **107**
- D.1 Composite T-boom drawing . . . 107
- D.2 Cross-section details of the composite T-boom . . . 109
- D.3 Bending stiffness of the composite T-boom . . . 110

E Verification of the shell model **113**
- E.1 Beam model . . . 113
- E.2 Displacement results and conclusion . . . 114

F Load cases for the FE model **117**
- F.1 Introduction . . . 117
- F.2 EO-3PT . . . 118
- F.3 EO-ELC . . . 120
- F.4 SC . . . 122

G Experimental setup **125**
- G.1 Manufacturing of coupons . . . 125
- G.2 Preconditioning of the specimens . . . 127
- G.3 Static strength tests . . . 128
  - G.3.1 Tension test . . . 128
  - G.3.2 Compression test . . . 129
- G.4 Experimental results . . . 130
  - G.4.1 Moisture ingression tests data for the Hexply 8552/AS4 laminate . . . 130
  - G.4.2 Tension test results . . . 131
  - G.4.3 Compression test results for the Hexply 8552/AS4 laminate . . . 131
  - G.4.4 Static strength results for the Hexply 8552/IM7 laminate . . . 131

H Statistical tests **133**
H.1 2-parameter Weibull distribution . . . 133
H.2 k-sample Anderson-Darling test . . . 135
H.3 Maximum Normed Residual (MNR) test . . . 136
H.4 Weibull distribution . . . 136
  H.4.1 Shape and scale parameters . . . 136
  H.4.2 Goodness-of-fit test . . . 137
  H.4.3 A and B basis values . . . 137
H.5 Levene's test . . . 138
H.6 Data pooling results . . . 138

List of Figures

1.1 The Ampelmann system 2
1.2 Degrees of freedom of the gangway 2
1.3 Workflow of the Master thesis 4

2.1 Overview of the T-boom for illustrative purpose 8
2.2 General operational procedure for the Ampelmann system 8
2.3 Lifetime distribution of the Ampelmann system (Courtesy: Ampelmann) 10
2.4 Composite T-boom design concepts 11
2.5 Truss based design concepts 12
2.6 Truss based design concepts 13
2.7 Box beam cross-section 15
2.8 Directions of the force and moment resultants 16
2.9 Resin pockets formed at flange/web intersection 17
2.10 Flange crippling of stiffener 18
2.11 No Edge Free (NEF) webs and flanges of box beam 18
2.12 Comparison of fatigue damage mechanism 21

3.1 Notation of the truss members of the T-boom 27
3.2 Variation of $I_{box,beam}/M_{box,beam}$ with a_{box} for t_{box} = 4 mm 32
3.3 Variation of $I_{box,beam}/M_{box,beam}$ with t_{box} for a_{box} = 50 mm 32
3.4 Location of the rollers and section for the FE model 34
3.5 T-boom section used in the FE model 35
3.6 Meshed model of the T-boom section of element edge length = 50 mm 37
3.7 Location of point 1 and 2 in the T-boom section 37
3.8 Vertical displacement at point 2 for various element edge lengths 38
3.9 Schematic beam model of the gangway subjected to a tip load 39

3.10 Variation of tensile and compressive strength with % moisture content (for illustrative purpose only) . . . 45
3.11 T-T and C-C fatigue curves for moisture contents M_1 and M_2 (for illustrative purpose only) . . . 46

4.1 Boundary conditions for the FE model in the y and z axis . . . 53
4.2 Boundary conditions for the FE model in the x axis . . . 54
4.3 Deflection of the T-boom section during SC . . . 54
4.4 Tsai-Wu value of the T-boom section during SC . . . 55
4.5 Deflection of the T-boom section during EO-3PT . . . 56
4.6 Tsai-Wu value of the T-boom section during EO-3PT . . . 57
4.7 Deflection of the T-boom section during EO-ELC . . . 58
4.8 Tsai-Wu value of the T-boom section during EO-ELC . . . 59
4.9 Local buckling analysis for the design option A during SC . . . 61
4.10 Schematic beam model of the gangway including the effect of Main Boom (MB)/T-boom interface . . . 64
4.11 Moisture absorption curve for Hexply 8552/AS4 laminate . . . 65
4.12 Scale parameter degradation curve of the compressive strength for the Hexply 8552/AS4 laminate . . . 68
4.13 Scale parameter degradation curve of the tensile strength for Hexply 8552/AS4 laminate . . . 69
4.14 S-N curves for T-T and C-C fatigues . . . 71
4.15 Modified S-N curve for T-T fatigue . . . 73
4.16 Modified S-N curve for C-C fatigue . . . 73

A.1 Cross-section details of member 1 . . . 89
A.2 Cross-section details of member 2 . . . 90
A.3 Cross-section details of member 3 . . . 91
A.4 Cross-section details of member 4 . . . 91
A.5 Cross-section details of member 5 . . . 92
A.6 Cross-section details of member 6 . . . 92
A.7 Cross-section of the T-boom for bending stiffness calculation . . . 93

D.1 Cross-section details of member 1,3,4,5 and 6 . . . 109
D.2 Cross-section details of member 2 . . . 109
D.3 Cross-section of the composite T-boom for bending stiffness calculation . . . 110

E.1 FE model of the FRP box beam of mesh size = 5 mm . . . 114
E.2 Vertical displacement result of the FRP box beam . . . 115

F.1 Remaining section of the T-boom . . . 117

G.1 C-scan results . . . 126
G.2 Illustrations depicting the methodology to manufacture the coupons . . . 127

G.3 Illustration of a tensile coupon 128
G.4 Tension test setup 129
G.5 Illustration of a compression coupon 129
G.6 CLC fixture for the compression test 130

H.1 Effect of scale parameter for the Weibull distribution 134
H.2 Effect of shape parameter for the Weibull distribution 134

List of Tables

2.1 Current mass and c.o.g of the GXL gangway 7
2.2 Preliminary load cases for the composite T-boom 10

3.1 Axial and bending stiffness of the chords and bracings 28
3.2 Layup choices for the composite T-boom 30
3.3 Shear forces and bending moments due to reaction forces at the tip 35
3.4 Shear forces and bending moments due to live mass 35
3.5 Shear forces and bending moments due to self-weight 36
3.6 Shear forces and bending moments due to slewing and telescopping 36
3.7 Shear forces and bending moments due to weight of the tip 36
3.8 Shear forces and bending moments due to wind 36
3.9 Maximum displacement and strain energy for various element edge lengths 38
3.10 Laminate level test matrix per preconditioning period 42
3.11 Moisture ingression test matrix 43
3.12 Tension and compression test matrix 43
3.13 Test condition notation 44

4.1 Dimensions of the chords and bracings of the composite T-boom 49
4.2 Layup of the chords and bracings for the design option A 50
4.3 Layup of the chords and bracings for the design option B 50
4.4 Membrane and bending modulus of the chords and bracings 50
4.5 Axial stiffness comparison of the members of the composite and steel T-boom . 51
4.6 Bending stiffness comparison of the chords of the composite and steel T-boom in x_1 and y_1 axis 51
4.7 Buckling modulus comparison of the bracings between the composite and steel T-boom in the weakest axis 52
4.8 Mass comparison of the composite and steel T-boom 53

4.9 FE results summary for the worst load cases 60
4.10 Parameters for the horizontal deflection determination 62
4.11 Horizontal deflection comparison of the gangway 62
4.12 Parameters for the vertical deflection determination 62
4.13 Vertical deflection comparison of the gangway 63
4.14 Natural frequency comparison of the gangway 63
4.15 Column buckling load of the T-boom 64
4.16 Moisture ingression test results 65
4.17 Static compressive strength results of Hexply 8552/AS4 laminate 66
4.18 Static tensile strength results of Hexply 8552/AS4 laminate 67
4.19 Data pooling results of the compressive strength of Hexply 8552/AS4 laminate . 67
4.20 Data pooling results of the tension strength of Hexply 8552/AS4 laminate 69
4.21 Static tensile and compressive strength results of Hexply 8552/IM7 laminate . . . 70
4.22 Cost breakdown of the composite and existing T-boom 78

E.1 Box beam dimensions 113
E.2 Graphite/epoxy T300/5208 properties 113
E.3 Displacement results comparison between FE and analytical model 114

F.1 Total accelerations for EO-3PT 118
F.2 Shear forces and bending moments due to live mass for EO-3PT 118
F.3 Shear forces and bending moments due to slewing and telescopping for EO-3PT 119
F.4 Shear forces and bending moments due to self-weight for EO-3PT 119
F.5 Shear forces and bending moments due to tip weight for EO-3PT 119
F.6 Force coefficients of the truss members 120
F.7 Wind loads on the truss members 120
F.8 Shear forces and bending moments due to wind load for EO-3PT 120
F.9 Total accelerations for EO-ELC 121
F.10 Shear forces and bending moments due to live mass for EO-ELC 121
F.11 Shear forces and bending moments due to self-weight for EO-ELC 121
F.12 Shear forces and bending moments due to tip weight for EO-ELC 122
F.13 Total accelerations for SC 122
F.14 Shear forces and bending moments due to reaction forces at tip for SC 122
F.15 Shear forces and bending moments due to self-weight for SC 123
F.16 Shear forces and bending moments due to tip weight for SC 123
F.17 Shear forces and bending moments due to wind load for SC 123

G.1 Mass of the coupons in mg for different preconditioning periods 130
G.2 Tension strength results in MPa for the Hexply 8552/AS4 laminate for different preconditioning periods 131
G.3 Compression strength results in MPa for the Hexply 8552/AS4 laminate for different preconditioning periods 131
G.4 Static strength results in MPa for the Hexply 8552/IM7 laminate 132

H.1 Data pooling tests statistic results 138

List of Acronyms

3-D	Three Dimensional
CFRP	Carbon Fibre Reinforced Polymer
CLAME	Code for Lifting Appliances in a Marine Environment
CLC	Combined Loading Compression
CLT	Classical Lamination Theory
c.o.a.	centre of area
c.o.g.	centre of gravity
C-C	Compression-Compression
CTD	Cold Temperature Dry
EO-3PT	Emergency Operation- 3 People Transfer
EO-ELC	Emergency Operation- Extra Length + Cargo
ETW	Elevated Temperature Wet
FE	Finite Element
FRP	Fibre Reinforced Polymer
GFRP	Glass Fibre Reinforced Polymer
MB	Main Boom
MNR	Maximum Normed Residual
NEF	No Edge Free
NO-SE	Normal Operation- Starting/Ending
NO-PT	Normal Operation- People Transfer

NO-CT	Normal Operation- Cargo Transfer
OSL	Observed Significance Level
R.H.	Relative Humidity
RTD	Room Temperature Dry
S2S	Ship to Ship
SC	Stowed Condition
T-boom	Telescoping boom
T-C	Tension-Compression
T-T	Tension-Tension
UV	Ultraviolet

List of Symbols

List of Symbols

Abbreviations

$[A_{ij}]$	Extensional stiffness matrix	[N/mm]
$[B_{ij}]$	Extension-bending coupling matrix	[N]
$[D_{ij}]$	Bending stiffness matrix	[N·mm]
α	Shape parameter for the two parameter Weibull distribution	[-]
α_C	Shape parameter for the two parameter Weibull distribution describing static compression strength	[-]
α_i	Shape parameter for the two parameter Weibull distribution of the ith test condition	[-]
α_{pool}	Shape parameter for the two parameter Weibull distribution of the pooled data	[-]
α_T	Shape parameter for the two parameter Weibull distribution describing static tension strength	[-]
β	Scale parameter for the two parameter Weibull distribution	[N/mm^2]
β_C	Scale parameter for the two parameter Weibull distribution describing static compression strength	[N/mm^2]
β_i	Scale parameter for the two parameter Weibull distribution of the ith test condition	[N/mm^2]
β_{pool}	Scale parameter for the two parameter Weibull distribution of the pooled data	[N/mm^2]
β_T	Scale parameter for the two parameter Weibull distribution describing static tension strength	[N/mm^2]
ν	Frequency of the loading	[Hz]
ν_{12m}	Poisson's ratio of the laminate	[-]
ν_{12}	Poisson's ratio of the ply	[-]
ρ_{steel}	Density of steel	[kg/mm^3]
σ	Applied load	[N/mm^2]
σ_{cu}^{u}	Ultimate compressive strength of the flange and the web	[N/mm^2]
σ_1	Ply stress in the fibre direction (1 direction)	[N/mm^2]

σ_2	Ply stress perpendicular to the fibre direction (2 direction)	[N/mm^2]
$\sigma_{C,Mi}$	Compressive stress that leads to failure after N cycles for moisture content M_i	[N/mm^2]
$\sigma_{compression}$	Compression strength of the coupon	[N/mm^2]
$\sigma_{crip,flange}$	Crippling stress of the flange	[N/mm^2]
$\sigma_{crip,web}$	Crippling stress of the web	[N/mm^2]
σ_{max}	Maximum stress during cyclic loading	[N/mm^2]
σ_{min}	Minimum stress during cyclic loading	[N/mm^2]
σ_m	Mean stress during cyclic loading	[N/mm^2]
$\sigma_{T,Mi}$	Tensile stress that leads to failure after N cycles for moisture content M_i	[N/mm^2]
$\sigma_{tension}$	Tensile strength of the coupon	[N/mm^2]
τ_{12}	Shear ply stress	[N/mm^2]
$\{\epsilon_o\}$	Mid-surface strains of the laminate	[-]
$\{\kappa\}$	Mid-surface curvatures of the laminate	[1/mm]
$\{M\}$	Moment resultants applied to a laminate	[N]
$\{N\}$	Force resultants applied to a laminate	[N/mm]
A	Area of the truss member exposed to the wind	[mm^2]
A_{box}	Area of the box beam	[mm^2]
a_{box}	Height of the box beam cross-section	[mm]
$A_{compression}$	Area of the compression coupon	[mm^2]
A_{pool}	A basis value of the pooled data	[MPa]
A_{steel}	Area of the steel beam	[mm^2]
$A_{tension}$	Area of the tensile coupon	[mm^2]
b_{box}	Width of the box beam cross-section	[mm]
B_{pool}	B basis value of the pooled data	[MPa]
BM_x	Bending moment in the x axis	[N·mm]
BM_z	Bending moment in the z axis	[N·mm]
D	Fickian material diffusion constant through-the thickness of the material	[mm^2/s]
E_{1b}	Bending modulus of the laminate	[GPa]
E_{1m}	Membrane modulus of the laminate	[GPa]
E_1	Tensile modulus of the ply in the fibre direction	[GPa]
E_2	Tensile modulus of the ply perpendicular to the fibre direction	[GPa]
$E_{compression}$	Compressive modulus of the coupon	[GPa]
E_{steel}	Modulus of elasticity of steel	[N/mm^2]
$E_{tension}$	Tensile modulus of the coupon	[GPa]
EA_{box}	Axial stiffness of the box shaped beam	[N]
$EI_{avg,x}$	Length average bending stiffness of the MB and T-boom in the x axis	[N·mm^2]
$EI_{avg,z}$	Length average bending stiffness of the MB and T-boom in the z axis	[N·mm^2]
$EI_{box,x1}$	Bending stiffness of the box shaped beam in the x1 axis	[N·mm^2]
$EI_{box,y1}$	Bending stiffness of the box shaped beam in the y1 axis	[N·mm^2]
$EI_{MB,x}$	Bending stiffness of the MB in the x axis	[N·mm^2]

$EI_{MB,z}$	Bending stiffness of the MB in the z axis	[N·mm^2]
$EI_{Tboom,x}$	Bending stiffness of the T-boom in the x axis	[N·mm^2]
$EI_{Tboom,z}$	Bending stiffness of the T-boom in the z axis	[N·mm^2]
EI_{Tboom}	Minimum bending stiffness of the T-boom	[N·mm^2]
F_x	Tip load in the horizontal direction	[N]
f_x	Natural frequency of the gangway in bending in the horizontal direction	[Hz]
F_z	Tip load in the vertical direction	[N]
f_z	Natural frequency of the gangway in bending in the vertical direction	[Hz]
$F_{compression}$	Compression failure load of the coupon	[N]
F_d	Duty factor	[$-$]
F_h	Hoisting factor	[$-$]
$F_{tension}$	Tensile failure load of the coupon	[N]
G_{12}	Shear modulus of the ply	[GPa]
h	Thickness of the laminate	[mm]
h_{spec}	Average specimen thickness	[mm]
$I_{box,beam}$	Moment of inertia of the box beam in the x$_1$ axis	[mm^4]
I_{box}	Moment of inertia of the box shaped beam in the weakest axis	[mm^4]
$I_{steel,x1}$	Moment of inertia of the steel beam in the x$_1$ axis	[mm^4]
$I_{steel,y1}$	Moment of inertia of the steel beam in the y$_1$ axis	[mm^4]
L	Span of the structure	[mm]
L_{box}	Length of the box shaped beam	[mm]
$L_{gangway}$	Length of the gangway	[mm]
L_g	Dead loads	[N]
L_{h1}	Horizontal component of live load due to heel and trim	[N]
L_{h2}	Next most unfavourable horizontal load	[N]
L_{h3}	Horizontal component of dead load due to heel and trim	[N]
L_l	Live loads	[N]
L_{MB}	Length of the MB	[mm]
L_{roller}	Distance between the rollers	[mm]
L_{Tboom}	Length of the T-boom	[mm]
L_w	Most unfavourable wind load	[N]
M	Mass of the gangway	[kg]
$M_{box,beam}$	Mass of the box beam	[kg]
M_{gain}	% Moisture gain percentage	[%]
M_i	Moisture content at time t_i	[%]
m_{MB}	Mass of the MB	[kg]
M_m	Effective moisture equilibrium content	[%]
m_{Tboom}	Mass of the T-boom	[kg]
N	Number of cycles	[-]
$N_{c,C}$	Number of cycles at which P is maximized for static compression	[-]

$N_{c,T}$	Number of cycles at which P is maximized for static tension	[-]
N_c	Number of cycles at which P is maximized	[-]
n_{plies}	Number of plies	[-]
P	Probability of failure anywhere between 1 and N cycles	[-]
p	Probability of failure in each cycle	[-]
$P_{box,crip,flange}$	Compression load on the box beam to cause flange crippling failure	[N]
$P_{box,crip,web}$	Compression load on the box beam to cause web crippling failure	[N]
$P_{box,crip}$	Minimum compression load on the box beam to cause crippling failure	[N]
$P_{column,box}$	Column buckling load of the box shaped beam	[N]
$P_{column,Tboom}$	Column buckling load of the T-boom	[N]
p_C	Probability of failure for a single compression cycle	[-]
$p_{Mi,C}$	Probability of failure for a single compression cycle for moisture content M_i	[-]
$p_{Mi,T}$	Probability of failure for a single tension cycle for moisture content M_i	[-]
p_T	Probability of failure for a single tension cycle	[-]
q_{MB}	Mass of the MB times the gravity constant divided by its length	[N/mm]
q_{Tboom}	Mass of the T-boom times the gravity constant divided by its length	[N/mm]
R	Stress ratio, which is given by $\sigma_{min}/\sigma_{max}$	[-]
S	Shear strength strength of the ply	[N/mm^2]
SF_x	Shear force in the x axis	[N]
SF_y	Shear force in the y axis	[N]
SF_z	Shear force in the z axis	[N]
SWL	Safe working load	[kg]
t	Time	[hrs]
t_{box}	Thickness of the box beam cross-section	[mm]
T_g	Glass transition temperature of the resin	[°C]
$w_{gangway,x}$	Horizontal deflection of the gangway due to tip load	[mm]
$w_{gangway,z}$	Vertical deflection of the gangway	[mm]
W_i	Current specimen mass	[mg]
$w_{MB,sw,z}$	Vertical deflection of the MB due to self-weight	[mm]
$w_{MB,tipload,x}$	Horizontal deflection of the MB due to tip load	[mm]
$w_{MB,tipload,z}$	Vertical deflection of the MB due to tip load	[mm]
W_o	Baseline specimen mass	[mg]
$w_{Tboom,sw,z}$	Vertical deflection of the T-boom due to self-weight	[mm]
$w_{Tboom,tipload,x}$	Horizontal deflection of the T-boom due to tip load	[mm]
$w_{Tboom,tipload,z}$	Vertical deflection of the T-boom due to tip load	[mm]
X^c	Compressive strength of the ply in the fibre direction	[N/mm^2]
X^t	Tensile strength of the ply in the fibre direction	[N/mm^2]
x_{ij}	jth data value for the ith test condition	[-]
Y^c	Compressive strength of the ply perpendicular to the fibre direction	[N/mm^2]
Y^t	Tensile strength of the ply perpendicular to the fibre direction	[N/mm^2]

Acknowledgments

A lot of people have positively influenced me during the course of my Masters, and, words are not sufficient to describe the gratitude I feel towards all of you. You have shared my enthusiasms, criticized me when I have been wrong, and, most importantly, motivated me to give my best regardless of the outcome.

I would like to thank...

... *Ampelmann B.V. and Miguel*, for giving me the opportunity to work on this idea.

... *my supervisors, Sonell and Koen*, for challenging me to think outside the box, and, their endless support and valuable guidance.

... *my associate professor, Christos*, for the amazing lectures and assignments on composites, and, technical support during the thesis.

... *my DASML Lab colleagues: Fred, Bart, Berthil, Misja, Gertjan, Johann and Frans*, for helping me with the lab work.

... *my spiritual mentors: Japesh Bandyopadhyay and Sadhguru*, for being the guiding light all these years.

... *my family: Appa, Amma, Anna, Archana, Mahesh, Pushpa, Ramesh, Rohita, all cousins, uncles and aunties back in India* , for their unconditional love and support.

... *my friends: David, Himanshu, Karthikeyan, Miguel, Mukesh, Nikita, Nishant, Rahul, Saranya, Shivanshu, Shreya, Thej, Telmo, Vivek, Xindi*, for all the great weekends, and, useful distractions.

... *my Spartan workout gang: Bart, Else, Paul, Richard, Sachin and others*, for all the crazy workouts, and, helping me push beyond my mental and physical limits.

... *the A.S.M. gang: Juliette, Krishna, Mohit, Nishant, Sachin and others*, for all the coffee chats and brainstorming sessions.

... *my former line managers: Anandappan, Ashok and Mehta*, for motivating me to pursue my Masters, and, realize my ambitions.

I hope you find reading my thesis enjoyable as much as I enjoyed writing it.

Delft, University of Technology
20 May 2016

Koushik Subramanian

“Live as if you were to die tomorrow. Learn as if you were to live forever.”
— *Mahatma Gandhi*

Chapter 1

Introduction

This chapter gives a brief overview of the Ampelmann system and presents the benefits and challenges of a composite gangway in an offshore environment. The core requirements set forth by Ampelmann for the composite gangway are identified and the research objective is formulated.

1.1 Ampelmann system : An overview

Over that last decades, the unstable prices of fossil fuels, growing need for green energy, and, increasing demand for energy have shifted the focus towards renewable sources of energy. Among various renewable energy sources, wind energy offers an attractive solution for a sustainable future as it is clean, free or indigenous, home grown and cost competitive compared to other energy sources. Majority of the wind turbine projects are gradually shifting offshore because of many reasons like higher wind speeds and lower turbulent winds at sea, thereby reducing fatigue loads [1]. One of the major disadvantages of offshore wind turbines is that its accessibility is dependent on sea and weather conditions leading to faulty turbine being sometimes unavailable for electricity production until it's maintained or repaired. This results in downtime of the turbines thereby causing a reduction in electricity production and ultimately leading to loss of revenue for the energy provider.

The Ampelmann system shown in Figure 1.1 was designed to facilitate safe and increased accessibility of offshore wind farms in order to reduce downtime of offshore turbines, and, the subsequent loss of revenue for the energy provider. The system compensates ship motions in all 6 degrees of freedom thereby enabling safe and easy access to the offshore structure despite adverse weather conditions [1].

Transfer of personnel from the Stewart platform to the fixed offshore structure is facilitated by the use of a gangway which is the focus of the thesis. The gangway is a steel structure and consists of 3 sub-assemblies: a Main Boom (MB), a Telescoping boom (T-boom) and a Tip. The coordinate system of the gangway that will be used throughout the thesis is shown in Figure 1.1.

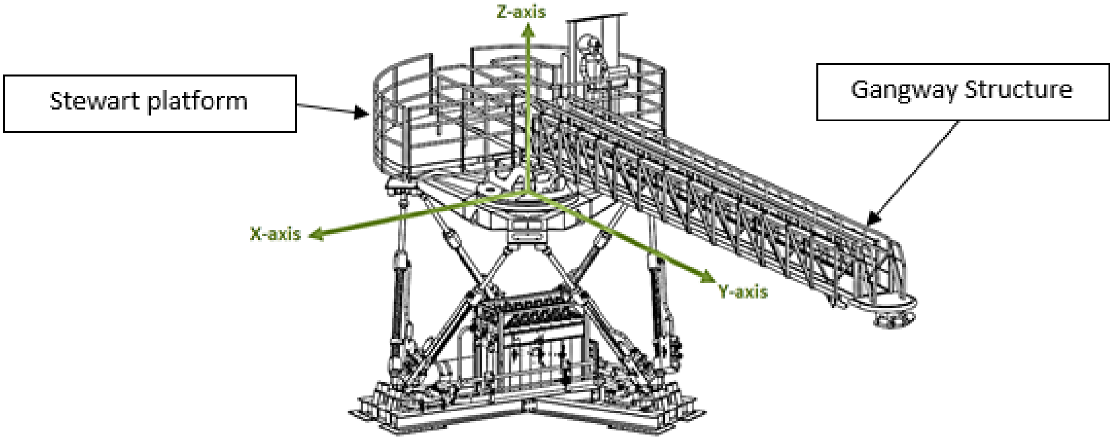

Figure 1.1: The Ampelmann system (Courtesy: Ampelmann)

The residual motions are compensated by the gangway using its 3 degrees of freedom namely: Slewing (rotation about z-axis of the hexapod), Luffing (rotation about x-axis of the hexapod) and Telescoping (shown in Figure 1.2). The motions of the gangway can be made either passively (Freefloating) or actively (Manual). In the manual mode, the gangway is manually steered out to the target while in the Freefloating mode, the gangway moves along with the residual motions of the hexapod. Hexapod or stewart platform is a configuration of six hydraulic cylinders which compensates the vessel motions in all 6 degrees of freedom. The passive mode also allows for Ship to Ship (S2S) operations, as it enables the gangway to move along with the target vessel motions. The current design of the gangway is a truss based steel structure, measuring approximately 3800 kg in mass and reaching a maximum length of 25 m when fully extended.

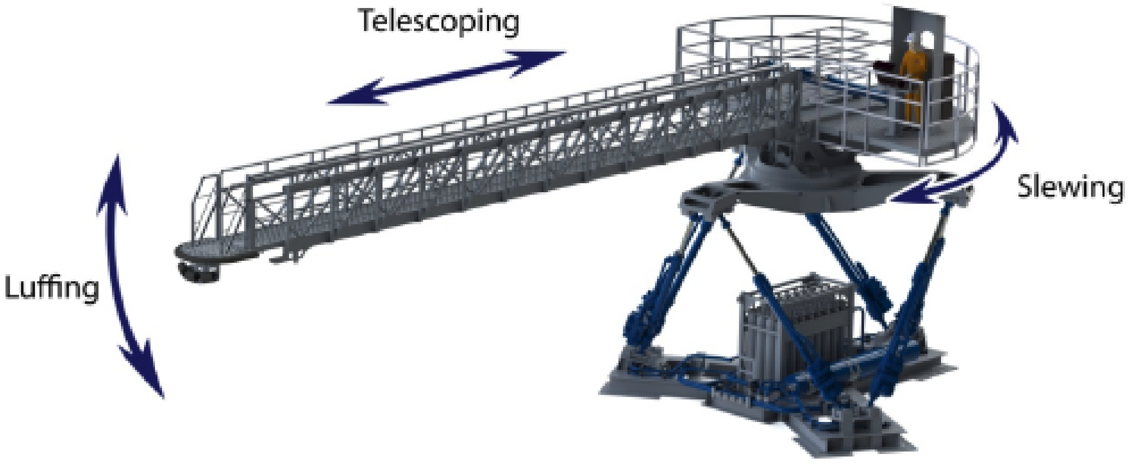

Figure 1.2: Degrees of freedom of the gangway

1.2 Composite gangway: Benefits and challenges

Studies carried out by Daniel and Ishai [2] prove that composite materials have excellent stiffness to weight ratio, high impact strength and corrosion resistance. Hence, the use of composite materials may lead to a lighter, stronger gangway which is more durable than the existing one. This may even lead to a "snowball effect" where the gangway can be made longer, or, the hydraulic power to operate the gangway can be reduced. Composite gangways do exist but their utility in offshore applications, or their functionality with spans of 20 m or more, is hitherto unexplored. Designers are deterred from choosing composites by factors like high raw material cost, difficulties in certification and fire-safety requirements [3–5].

In addition, the fatigue phenomena for such structures (loads due to waves and winds, etc.) are dependent on the weather conditions and thus, unpredictable to a large degree. During its lifetime, the structure will also be exposed to hostile conditions like humidity, rain, solar radiation, extreme temperatures, hail and snow [6]. In order to ensure the safety of the structure, understanding the fatigue behaviour of the composite material and its structure becomes imperative, however, difficult.

1.3 Core requirements of Ampelmann

Improvements in the current design of the gangway are anticipated by the replacement of a steel structure by a composite structure. Ampelmann set forth the minimum core requirements wherein the composite gangway should:

- be lighter than the existing gangway
- be cost competitive with the existing gangway
- be as durable as the existing gangway
- be manufacturable and maintainable
- be safe for transfer of personnel and cargo
- not pose any hazard to the environment

The current Master thesis explores the feasibility of a composite material design of the T-boom of Ampelmann gangway GXL due to time constraint. It is simple and feasible from the economic and manufacturing point of view to replace the existing T-boom with a composite T-boom and subsequently test it rather than doing the same for the entire gangway. This task comes with many challenges which makes it a subject fit for a master thesis project. The primary objective of this study is to estimate the potential weight savings while accounting for some of the harsh environmental conditions such as moisture ingress, temperature variations and Ultraviolet (UV) radiation throughout the structure's operational life.

1.3.1 Research objective

The research objective for the Master thesis is the following:

" Design an offshore composite T-boom made from Carbon Fibre Reinforced Polymer (CFRP) or Glass Fibre Reinforced Polymer (GFRP) that is at least 10% lighter than the existing steel based design and develop a suitable fatigue model to determine it's fatigue life."

1.4 Master thesis: Workflow

Figure 1.3 shows the workflow of the Master thesis. The first phase is the literature study which involves defining the design requirements and load cases, identifying a suitable design concept and fatigue model for the the composite T-boom. After the literature study phase, a preliminary design of the composite T-boom is developed based on the existing steel based design. Subsequently, a Finite Element (FE) analysis is performed to determine whether the structure satisfies the design requirements. Another purpose of doing the FE analysis is to determine the structural " hotspots"(regions with peak stresses) during the extreme loading conditions. In the detailed analysis phase, the global deflection and natural frequency of the gangway retrofitted with the composite T-boom are determined. Material characterization tests are subsequently performed to determine the effect of moisture and temperature on the material properties of the composite coupons. Finally, an appropriate fatigue model is developed to predict the life of the composite T-boom based on its load spectra.

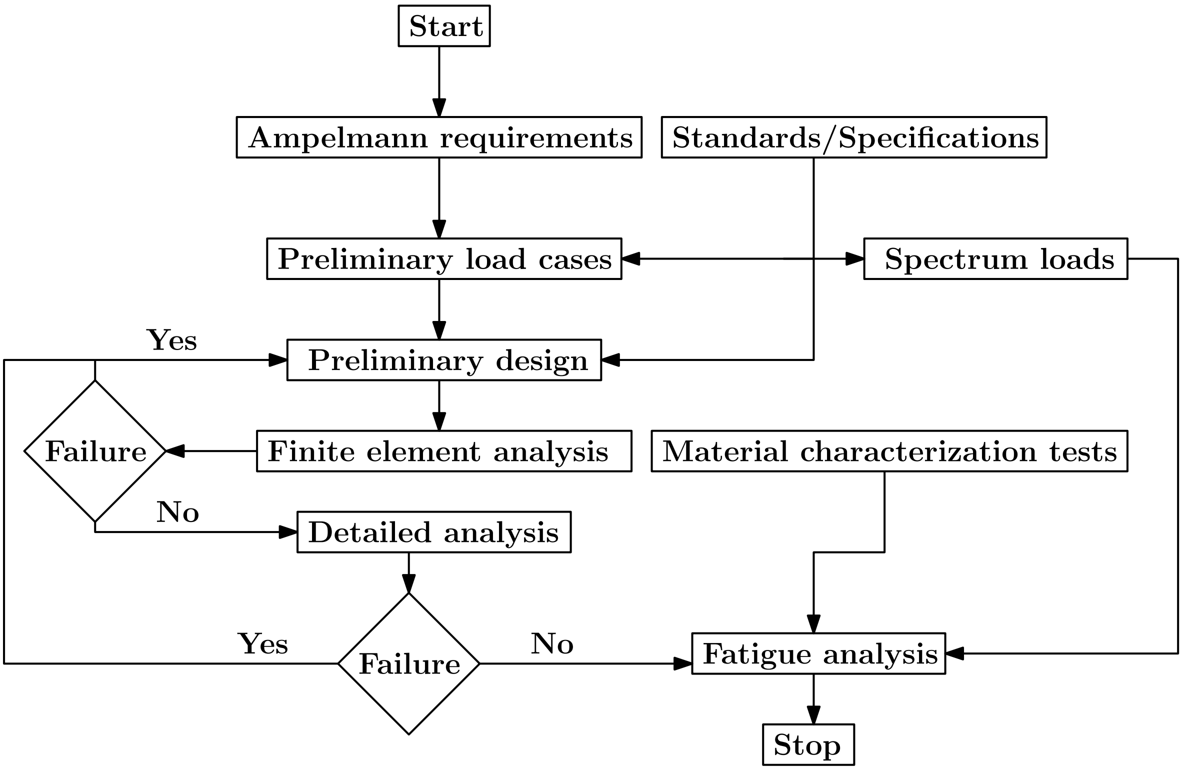
Start
Ampelmann requirements
Standards/Specifications
Preliminary load cases
Spectrum loads
Yes
Preliminary design
Failure
Finite element analysis
Material characterization tests
No
Detailed analysis
Yes
Failure
No
Fatigue analysis
Stop

Figure 1.3: Workflow of the Master thesis

1.5 Readers guide

Chapter 2 gives an overview of the literature on the standards/specifications, design concepts and composite fatigue models relevant for the Master thesis, and, subsequently formulates research questions and sub-goals. Chapter 3 outlines the methodology used to get answers to the research questions framed in Chapter 2. Chapter 4 discusses the results obtained during the design and fatigue analysis phase. Finally in Chapter 5, a reflection on the significance of the research is done and conclusions and recommendations are given.

Chapter 2

Literature study

This chapter summarizes the literature studied for the Master thesis. Various design concepts, material systems and fatigue models are explored for the composite Telescoping boom (T-boom). Subsequently, the design requirements and load cases are derived based on the standards and specifications. Also, a suitable fatigue model is selected for the estimation of fatigue life of the T-boom. Finally, a review is done on the material characterizations tests required to study the effect of environment on the material properties.

2.1 Gangway: Existing design

As mentioned earlier, the current design of the gangway is a truss based steel structure, measuring approximately 3800 kg in mass and 25 m in length. The mass and centre of gravity (c.o.g.) of the existing gangway are shown in Table 2.1. The coordinate system in which the c.o.g. is defined, is shown in Figure 1.1. The c.o.g. of the gangway is defined with respect to the the center of the slewing ring. Based on the Ampelmann specifications, the structure is designed for a deflection limit of L/100 where L is the span of the structure (mm). The dimensions of the existing T-boom are approximately 13 m x 0.90 m x 0.87 m. The details of the existing T-boom design are shown in Appendix A.

Table 2.1: Current mass and c.o.g of the GXL gangway

Part	Current mass (kg)	c.o.g. x (m)	c.o.g. y (m)	c.o.g z (m)
Tip (retracted)	182	0	15.32	1.08
T-boom (retracted)	1365	0.02	7.61	1.42
Main Boom (MB) plus Add-ons	2181			
MB	1851	0.01	6.51	1.34
Add-ons	330	0.03	7.81	1.81

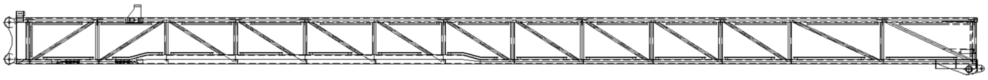

Figure 2.1: Overview of the T-boom for illustrative purpose (Courtesy: Ampelmann)

2.2 Preliminary load cases for the composite T-boom

The design of the existing gangway is based on a set of load cases defined by Lloyd's register in Code for Lifting Appliances in a Marine Environment (CLAME) [7] and are given by Eq. (2.1).

$$F_d \cdot (L_g + F_h(L_l + L_{h1}) + L_{h2} + L_{h3}) + L_w \tag{2.1}$$

where F_d is the duty factor, F_h is the hoisting factor, L_g are the dead loads (N), L_l are the live loads (N), L_{h1} is the horizontal component of the live load due to heel and trim (N), L_{h2} is the next most unfavourable horizontal load (N), L_{h3} is the horizontal component of the dead load due to heel and trim (N) and L_w is the most unfavourable wind load (N).

Heel is defined as the rotation of the ship about the telescoping direction (y-axis) while trim is defined as the rotation of the ship about the luffing direction (x-axis). The hoisting factor is applied only on the live loads which are cargo loads and people while self-weight of the gangway is treated as a dead load subjected to accelerations. Based on the operational procedure shown in Figure 2.2, the preliminary load cases for the composite T-boom design are defined from Section 2.2.1 to 2.2.6.

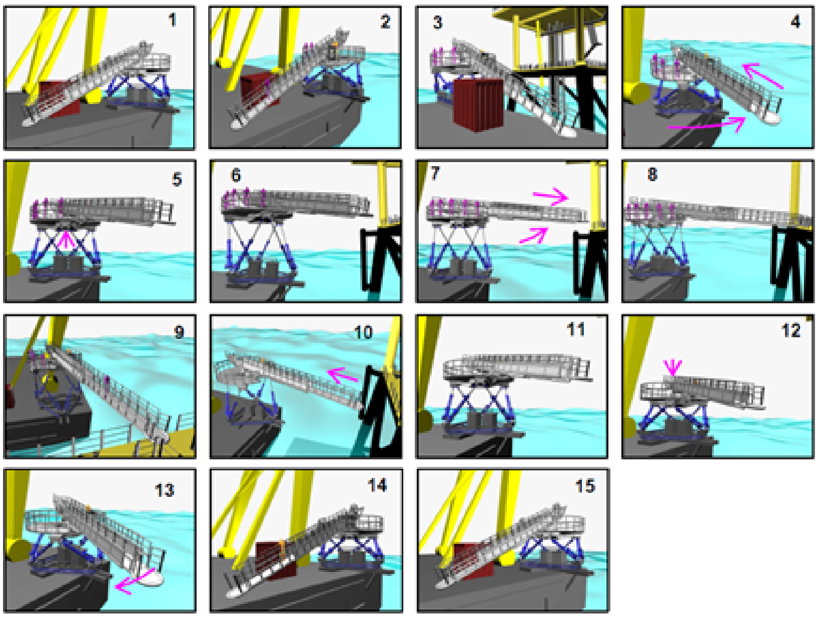

1. Stowed Condition: No Hydraulic Pressure, Gangway sea fastened
2. People Boarding: Gangway sea fastening released, People walk over gangway.
3. Settled: Hydraulic pressure on Platform retracted. No people on gangway. 16 people on transfer deck.
4. Moving gangway outwards: Luffing and Slewing of gangway in retracted position
5. To neutral position: Transfer deck rises to neutral position.
6. Compensation On: Full compensationin 10s, No accelerations.
7. Positioning gangway: Luffing, Slewing and Telescoping of gangway towards landing point
8. Contact with Structure: Contact with structure, Free-floating mode
9. People Transfer: One person at a time walks to structure over gangway
10. Retraction gangway: Retraction of gangway by Luffing, Slewing and Telescoping in active mode
11. Compensation off: Fade out of compensation platform in neutral position
12. To settled position: Transfer deck lowers to settled position
13. Moving gangway to vessel: Luffing, Slewing and Telescoping of gangway
14. People Unboarding: Hydraulic pressure off, People walk over gangway
15. Stowed Condition

Figure 2.2: General operational procedure for the Ampelmann system (Courtesy: Ampelmann)

2.2.1 Normal Operation- Starting/Ending (NO-SE)

In this case, the gangway is retracted and landed on the deck. The luffing angle is -17° and a maximum heel of 5° and trim of 2° of the ship are considered. Since the ship motions are not compensated, accelerations of 2 m/s^2 are considered in the x, y and z directions.

2.2.2 Normal Operation- People Transfer (NO-PT)

The hexapod is compensating thus reducing the accelerations in x, y and z directions to 0.5 m/s^2 . The T-boom is extended to a length of 7 m (measured from the tip of the MB) during a Ship to Ship (S2S) in free-float mode and subjected to extra tip forces.

2.2.3 Normal Operation- Cargo Transfer (NO-CT)

The hexapod is compensating and a KIB (weighing approximately 200 kg) is installed on the tip of the gangway. A KIB is a tool which is installed on the tip of the gangway to transfer cargo. The T-boom is extended to a length of 7 m and the luffing angle is assumed to be 0° for the most severe load case.

2.2.4 Emergency Operation- 3 People Transfer (EO-3PT)

This emergency case is best described when two people are transferring an injured person to a ship from a platform through the Ampelmann gangway. The T-boom is extended to a length of 7 m and the boom is landed. Here also, the luffing angle is assumed to be 0° for the most severe load case.

2.2.5 Emergency Operation- Extra Length + Cargo (EO-ELC)

In this emergency case, the gangway extends to a maximum length of 9 m and a KIB is installed on the tip of the gangway. It is assumed that the hexapod is compensating and the luffing angle is 0° for the most severe load case.

2.2.6 Stowed Condition (SC)

The Ampelmann system is in stowed condition when it is not used for people and cargo transfer. As defined in CLAME [7], during stowed condition, the structure has to withstand survival conditions of the vessel on which it is mounted. As the tip of the gangway has to be supported on the deck, it is assumed that the gangway is simply supported at all times.

Table 2.2 summarizes the preliminary load cases considered for the composite T-boom design.

Table 2.2: Preliminary load cases for the composite T-boom

	Unit	NO-SE	NO-PT	NO-CT	EO-3PT	EO-ELC	SC
T-boom extension	[m]	4.6	7.1	7.1	7.1	9.1	4.6
Person on gangway		0	1	0	3	0	0
Duty factor		1.2	1.2	1.2	1	1.2	1
Hoisting factor		1.15	1.15	1.15	1.15	1.15	1
Wind speed	[m/s]	0	0	0	20	20	63
Accelerations							
X direction	[m/s^2]	2	0.5	0.5	0.5	0.5	0
Y direction	[m/s^2]	2	0.5	0.5	0.5	0.5	4.91
Z direction	[m/s^2]	2	0.5	0.5	0.5	0.5	9.81
S2S accelerations							
X direction	[m/s^2]	0	0	0	0	0	0
Y direction	[m/s^2]	0	1.21	0	1.21	0	0
Z direction	[m/s^2]	0	1.14	0	1.14	0	0
Contact loading							
Free-float slew	[kN]	0	1	0	1	0	0
Free-float luffing	[kN]	0	1	0	1	0	0
Free-float telescope	[kN]	0	10	0	10	0	0
Boom angle	[^{0}]	-17	0	0	0	0	-17
Maximum heel	[^{0}]	5	0	0	0	0	30
Maximum trim	[^{0}]	2	0	0	0	0	0
Add-on		-	-	KIB	-	KIB	-
Hexapod compensating		No	Yes	Yes	Yes	Yes	No

2.3 Load spectra for the composite T-boom

Figure 2.3 shows the lifetime distribution of the Ampelmann system.

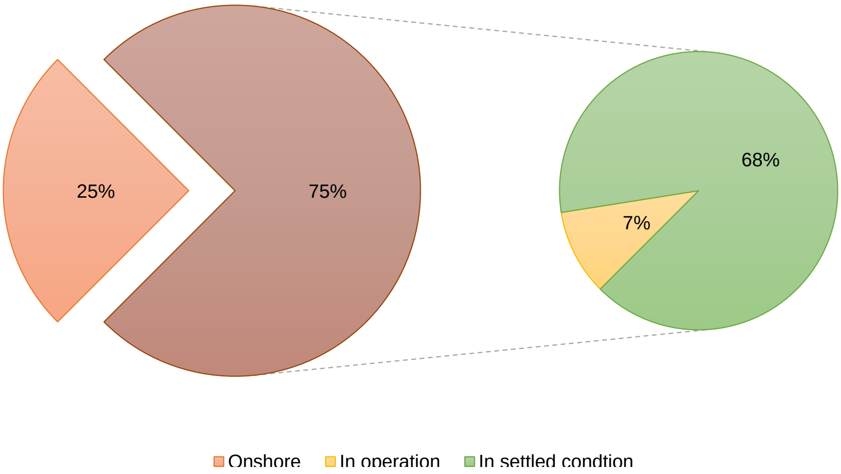

Figure 2.3: Lifetime distribution of the Ampelmann system (Courtesy: Ampelmann)

The various states of the Ampelmann system throughout its lifetime are:

- The Ampelmann system is onshore and under maintenance or sometimes in storage.
- The Ampelmann system is in settled condition and experiences vessel induced motions.
- The Ampelmann system is in an operation mode excluding the stowed condition shown in Figure 2.2.

It is assumed that the fatigue critical loads are mostly due to the settled condition because of the following reasons:

- In the settled condition, the gangway is subjected to high cycle wave induced loads.
- Cargo transfer and people transfer are low frequency impulse loads which occur at less than 10% of the lifetime time of the gangway.
- The dynamic response of telescopping, slewing, luffing, cargo transfer and people transfer are quite complex to model, and, beyond the scope of the Master thesis.

In the Master thesis, a fatigue model is adapted to predict the life of Fibre Reinforced Polymer (FRP) structures used in offshore applications, with emphasis on the effect of environmental factors. Due to certain limitations of the model, described in Section 4.8, the fatigue life of the composite T-boom is not estimated.

2.4 Composite gangway : Design concepts

Figure 2.4 shows the two possible design concepts that can be adopted for the composite T-boom. Truss based structures are of two basic types: a deck-truss shown in Figure 2.5a and a side-truss or pony-truss design shown in Figure 2.5b.

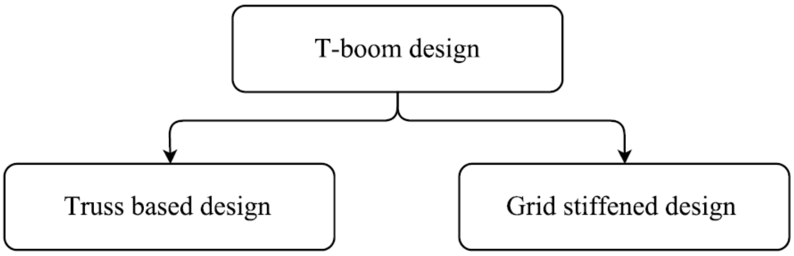

Figure 2.4: Composite T-boom design concepts

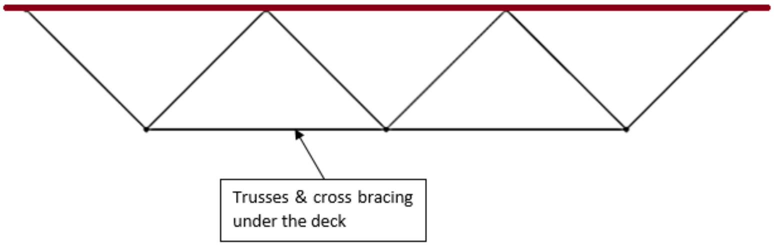

(a) Example of deck truss

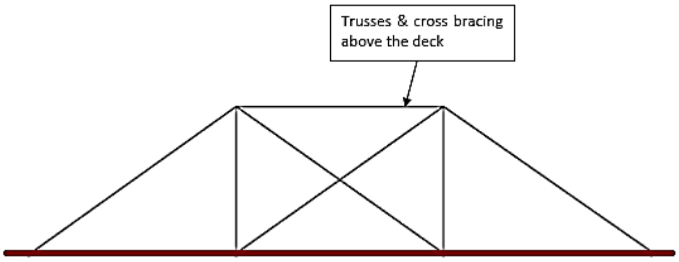

(b) Example of side truss

Figure 2.5: Truss based design concepts

The high specific properties and tailorability of composite materials have favoured the use of the grid stiffened design in aircraft structures. They have high buckling resistance due to the presence of skin stiffened by ribs in the form of grids (thereby increasing the high bending stiffness). Shroff [8] observes that fibre reinforced composites are highly suitable for grid stiffened structures as the ribs are primarily loaded along its length. Huybrechts, et al. [9] compare the benefits and drawbacks of grid structures against other state of the art structures. The authors observe that grid structures have a better damage tolerance than laminates and sandwich structures as they contain delamination to within one cell, thereby preventing catastrophic failure due to the spread of the damage. Other benefits stated are the low cost manufacturing and structural efficiency. Although, the design is quite novel and may yield considerable weight savings than the truss based design, the lack of knowledge/experience on their failure and fatigue behaviour in an offshore environment makes its feasibility study beyond the scope of this Master thesis.

In deck-truss bridges, trusses and cross bracing are under the deck, while in side-truss bridges, the superstructure trusses are on the sides of the bridge. The latter is adopted for the design of the T-boom due to its similarity with the existing design. A deck truss based design is not adopted for the composite T-boom because:

- deck beck-beam FRP bridges are typically used for boardwalks [10] and,
- the MB will require extensive modification before assembling the deck-truss T-boom.

Figure 2.6 shows the possible truss based design concepts applicable for the composite T-boom.

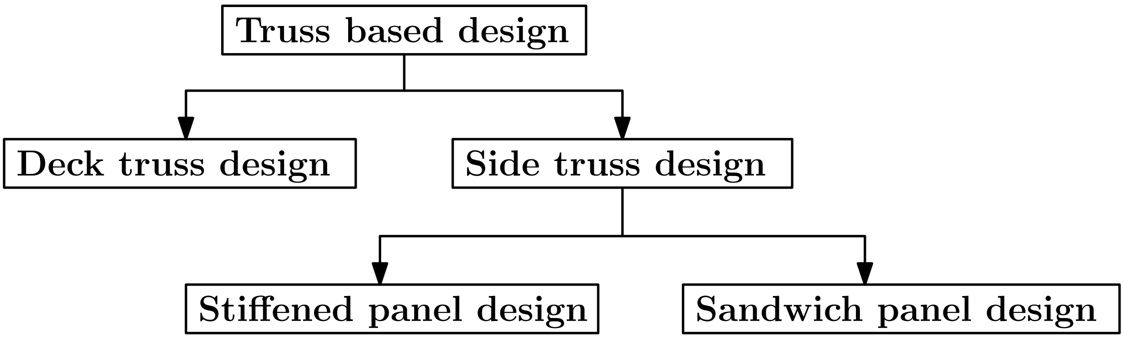

Figure 2.6: Truss based design concepts

The advantage of using sandwich structure is that it provides high bending stiffness and strength for a given weight by using a lightweight core and two face sheets. Although sandwich structures are increasingly used in marine applications like boats, hulls and submarines, they are not considered in the current analysis due to the following reasons:

- Sandwich cores have a tendency to retain water over their lifetime. As a result, core material may gradually corrode due to moisture ingress and subsequently decreases the structural integrity of the T-boom.
- Insufficient codes/guidelines for the design of sandwich structures for offshore applications necessitates the experimental validation of the design which is time consuming.
- Environmental factors like moisture ingress, temperature variations and UV radiation might interact with failure modes (like delamination between core and face sheets), thereby complicating the fatigue analysis of sandwich structures.

2.5 Composite gangway : Design requirements

As there are no specific codes for the design of an offshore composite gangway, it is considered relevant to compare the structure to a pedestrian bridge in the sense that both structures essentially facilitate safe and easy transfer of people. Groenier, et al. [10] state that FRP bridge design is governed by the magnitude of deflection rather than the strength required to keep them from failing due to low stiffness of FRP composites. The design requirements for the composite T-boom which are discussed from subsection 2.5.1 to 2.5.6, are based on AASHTO's Guide Specifications for Design of FRP Pedestrian Bridges [11] and Ampelmann requirements.

2.5.1 Deflection

The maximum deflection (both globally and locally) allowed for the structure is taken as $\frac{L}{100}$.

2.5.2 Design life

Based on the Ampelmann requirements, the design life of the composite T-boom should be at least 20 years.

2.5.3 Strength

The composite T-boom is assumed to be a stiffness based design, and, the critical failure modes are related to buckling like global buckling of T-boom, local buckling of truss members and crippling of stiffeners. It should be ensured that material failure does not occur before the lowest buckling load. Joints may result in stress raisers and their interaction with environment might create hotspots for failure. Analysing the failure modes at the joints and out of plane effects in an offshore environment is complex and will deviate from the scope of this master thesis. Hence, the out of plane effects of the structure are neglected and the joints are assumed to be perfect.

2.5.4 Durability

The structural members should have resistance to extreme in-service environments (like moisture diffusion, Ultraviolet (UV) radiation and high temperature) and impact. The effect of UV radiation on the degradation in material properties is not predominant as the design life is not large. The effect of UV radiation can be minimized by the use of UV coatings and is not considered further in the analysis. Hence, during the fatigue analysis, the effect of moisture and temperature are incorporated.

2.5.5 Safety factor

The safety factor for the material during the preliminary design of the composite T-boom is chosen to be 2.5 which includes a knock-down factor of 0.65 for impact, 0.8 for environment, and, 0.8 for material scatter. The knockdown factors are based on the values suggested by Kassapoglou [12]. Once the design of the composite T-boom is almost finalized, it is essential to check the validity of the knockdown values by testing, and, update them if necessary by rigorous statistical analysis [12]. Also, the safety factor for the loads are explicitly accounted in Eq. (2.1) in the form of F_d and F_h.

2.5.6 Vibration

High specific properties of FRP might lead to a lightweight “lively” T-boom. Excessive vibrations can cause user discomfort and affect the durability of the joints. Based on the Ampelmann requirements, the minimum fundamental frequency of the gangway retrofitted with the composite T-boom in bending should be atleast 1.33 Hz in the horizontal direction (x-axis) and 1.33 Hz in the vertical direction (z-axis) to match the current system.

2.6 Failure modes and stiffness of FRP beams

Only box shaped cross-sections are considered for the design of the composite T-boom due to the following reasons:

- Box shaped cross-sections have better buckling and torsional characteristics than open section shapes.
- FRP box beams are easily manufacturable and can be manufactured by pultrusion, filament winding and hand layup which are all relatively economic options.
- Similarity with the existing T-boom design (refer Appendix A)

The cross-section definition of the box section is shown in Figure 2.7. Here a_{box}, b_{box} and t_{box} correspond to height, width and thickness of the box beam cross-section in mm.

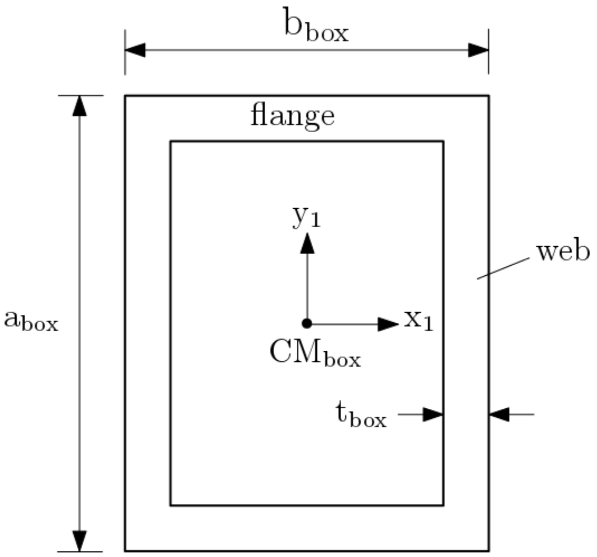

Figure 2.7: Box beam cross-section

Kassapoglou [12] suggests that it is a good engineering practice to allow some plies in the web to continue into the flanges to ensure better load continuity. Hence due to ease of manufacturability and better load continuity, it is assumed that the flanges and webs have the same layup.

2.6.1 Axial and bending stiffness

The first step to determine the stiffness and failure modes of a FRP box beam is to estimate the ABD matrix of its flanges and webs. It is assumed the ply is an orthotropic material with thickness much smaller than the other dimensions of the ply. Hence, the ply is assumed to be in a state of plane stress. The ABD matrix of a laminate having thickness h (mm) is evaluated based on Classical Lamination Theory (CLT) and the generalized constitutive relations are given by Eq. (2.2).

$$\begin{Bmatrix} N_x \\ N_y \\ N_{xy} \\ M_x \\ M_y \\ M_{xy} \end{Bmatrix} = \begin{bmatrix} A_{11} & A_{12} & A_{16} & B_{11} & B_{12} & B_{16} \\ A_{12} & A_{22} & A_{26} & B_{12} & B_{22} & B_{26} \\ A_{16} & A_{26} & A_{66} & B_{16} & B_{26} & B_{66} \\ B_{11} & B_{12} & B_{16} & D_{11} & D_{12} & D_{16} \\ B_{12} & B_{22} & B_{26} & D_{12} & D_{22} & D_{26} \\ B_{16} & B_{26} & B_{66} & D_{16} & D_{26} & D_{66} \end{bmatrix} \begin{Bmatrix} \epsilon_{xo} \\ \epsilon_{yo} \\ \gamma_{xyo} \\ \kappa_x \\ \kappa_y \\ \kappa_{xy} \end{Bmatrix} \tag{2.2}$$

where $\{N\}$ and $\{M\}$ are the force (N/mm) and moment resultants (N) applied to a laminate, $[A_{ij}]$ is the extensional stiffness matrix (N/mm), $[B_{ij}]$ is the extension-bending coupling matrix (N), $[D_{ij}]$ is the bending stiffness matrix (N·mm), $\{\epsilon_o\}$ and $\{\kappa\}$ are the mid-surface strains and curvatures (1/mm) of the laminate.

The directions of the force and moment resultants applied on the laminate are shown in Figure Figure 2.8.

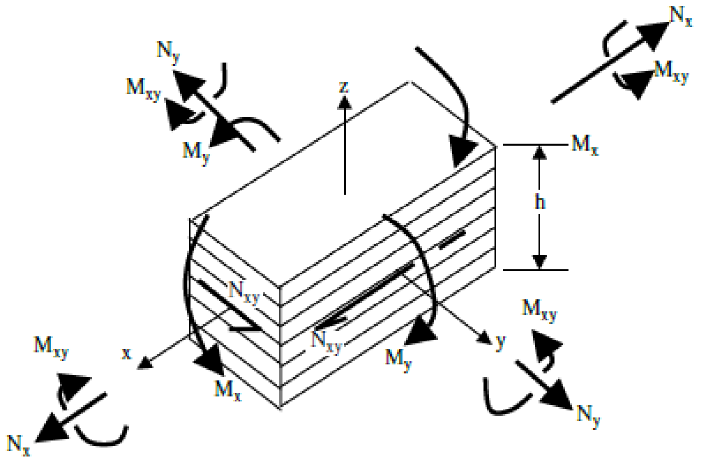

Figure 2.8: Directions of the force and moment resultants [12]

The methodology to formulate the ABD matrix can be found in Kassapoglou [12]. For a balanced and symmetric layup, the membrane modulus and Poisson's ratio are given by Eq. (2.3) and Eq. (2.4) respectively.

$$E_{1m} = \frac{1}{h} \frac{(A_{11}A_{22} - A_{12}^2)}{A_{22}} \tag{2.3}$$

$$\nu_{12m} = \frac{A_{12}}{A_{22}} \tag{2.4}$$

where E_{1m} is the membrane modulus (GPa) and ν_{12m} is the Poisson's ratio of the laminate. For a symmetric laminate and D$_{11}$=D$_{26}$=0, the bending modulus is given by Eq. (2.5).

$$E_{1b} = \frac{12}{h^3} \frac{(D_{11}D_{22} - D_{12}^2)}{D_{22}} \tag{2.5}$$

where E_{1b} is the bending modulus (GPa) of the laminate.

As the layup of the flange and web of the box beam are the same, their axial and bending modulus are the same. Hence, the equivalent axial and bending stiffness of the box cross-section are given by Eq. (2.6) and Eq. (2.7)- Eq. (2.8) respectively.

$$EA_{box} = E_{1m}(a_{box} \cdot b_{box} - (a_{box} - 2 \cdot t_{box}) \cdot (b_{box} - 2 \cdot t_{box})) \tag{2.6}$$

$$EI_{box,x1} = E_{1b}(\frac{1}{12}a_{box}^3 \cdot b_{box} - \frac{1}{12}(a_{box} - 2 \cdot t_{box})^3 \cdot (b_{box} - 2 \cdot t_{box})) \tag{2.7}$$

$$EI_{box,y1} = E_{1b}(\frac{1}{12}a_{box} \cdot b_{box}^3 - \frac{1}{12}(a_{box} - 2 \cdot t_{box}) \cdot (b_{box} - 2 \cdot t_{box})^3) \tag{2.8}$$

where EA_{box} is axial stiffness of the box shaped beam (N), $EI_{box,x1}$ is the bending stiffness of the box shaped beam in the x_1 axis (N·mm^2) and $EI_{box,y1}$ is the bending stiffness of the box shaped beam in the y_1 axis (N·mm^2).

Pockets are created when the plies are turned 90° at the flange/web intersection shown in Figure 2.9). The resin rich areas and wavy fibres in radius section imply that the strength and stiffness of the laminate are compromised. Although pockets are unavoidable, they can be reinforced by incorporating a piece of roving material or unidirectional material. In the Master thesis, the effect of pockets are not considered. By neglecting the force acting on the filler, the loads on the webs and flanges increase, making the design more conservative.

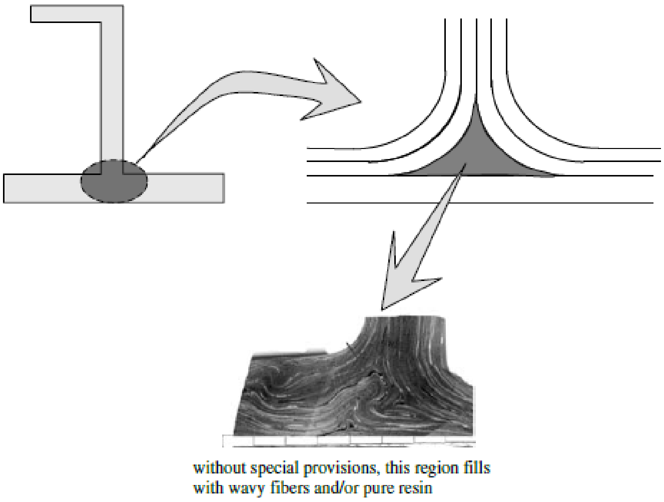
without special provisions, this region fills
with wavy fibers and/or pure resin

Figure 2.9: Resin pockets formed at flange/web intersection [12]

The major failure modes for a FRP box beam are column buckling, crippling and material failure [12].

2.6.2 Column buckling

The truss beams of the composite T-boom are assumed to be simply supported and the column buckling load is given by Eq. (2.9).

$$P_{column,box} = \pi^2 \frac{E_{1m} \cdot I_{box}}{L_{box}^2} \tag{2.9}$$

where $P_{column,box}$ is the column buckling load (N) of the box beam, L_{box} is the length of the beam (mm) and I_{box} is the moment of inertia of the box beam in the weakest axis (mm^4).

2.6.3 Crippling

Crippling is a local stability failure where a flange of the beam buckles and subsequently collapses shown in Figure 2.10.

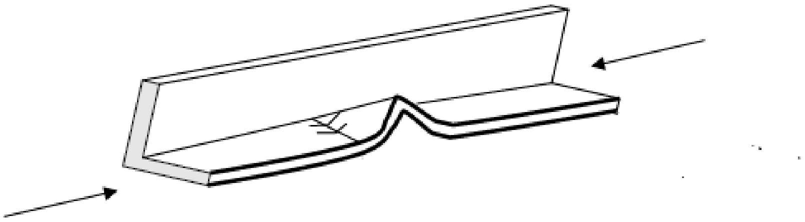

Figure 2.10: Flange crippling of stiffener [12]

The webs and flanges of the box beam are treated as No Edge Free (NEF) (see Figure 2.11) because they are supported at the ends by the flanges and webs respectively.

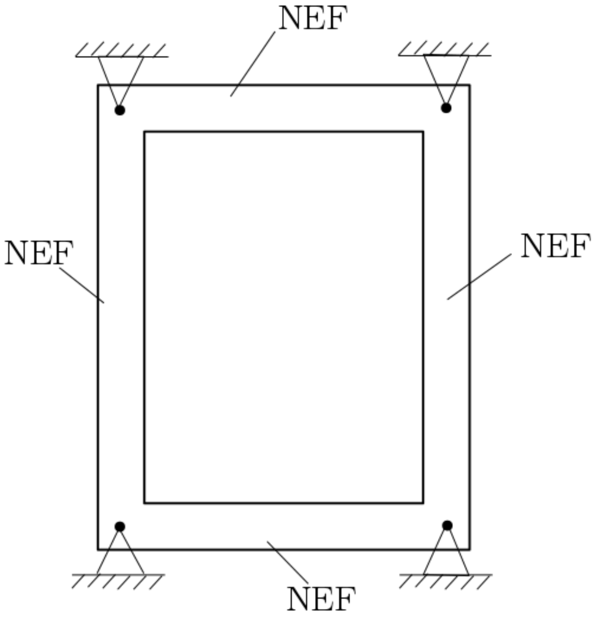

Figure 2.11: NEF webs and flanges of box beam

The B-basis value of the crippling stress of the web under compression load is given by [13]:

$$\sigma_{crip,web} = \frac{11 \cdot \sigma_{cu}^{u} \cdot t_{box}^{1.124}}{a_{box}^{1.124}} \tag{2.10}$$

for $a_{\text{box}} \geq 8.443 \cdot t_{\text{box}}$ and $\sigma_{\text{crip,web}}=\sigma_{cu}^{u}$ for $a_{\text{box}} < 8.443 \cdot t_{\text{box}}$

where $\sigma_{crip,web}$ is the crippling stress of the web (MPa) and σ_{cu}^{u} is the ultimate compressive strength of the flange and the web (MPa).

The B-basis value of the crippling stress of the flange under compression loads is given by [13]:

$$\sigma_{crip,flange} = \frac{11 \cdot \sigma_{cu}^{u} \cdot t_{box}^{1.124}}{b_{box}^{1.124}} \tag{2.11}$$

for $b_{\text{box}} \geq 8.443 \cdot t_{\text{box}}$ and $\sigma_{\text{crip,flange}}=\sigma_{cu}^{u}$ for $b_{\text{box}} < 8.443 \cdot t_{\text{box}}$

where $\sigma_{crip,flange}$ is the crippling stress of the flange (MPa).

The compression load required to cause crippling failure of the webs and flanges of the FRP box beam are given by Eq. (2.12) and Eq. (2.13) respectively.

$$P_{box,crip,web} = \sigma_{crip,web} \cdot A_{box} \tag{2.12}$$

$$P_{box,crip,flange} = \sigma_{crip,flange} \cdot A_{box} \tag{2.13}$$

where $P_{box,crip,web}$ and $P_{box,crip,flange}$ are the compression loads on the box beam to cause web crippling and flange crippling failure respectively (N). Also, A_{box} is the area of the box beam cross-section in mm^2.

The minimum compression load required to cause crippling failure of the box beam is given by Eq. (2.14).

$$P_{box,crip} = min(P_{box,crip,web}, P_{box,crip,flange}) \tag{2.14}$$

where $P_{box,crip}$ is the minimum compression load on the box beam to cause crippling failure (N).

2.6.4 Material failure

For the preliminary and detailed design, the first ply failure load is regarded as the ultimate failure load of the laminate and might lead to a conservative design. The Tsai-Wu failure criterion [14] is used to determine the first ply failure of the webs and flanges of the beam. The failure criterion is given by:

$$\frac{\sigma_1^2}{X^tX^c} + \frac{\sigma_2^2}{Y^tY^c} - \sqrt{\frac{1}{X^tX^c}\frac{1}{Y^tY^c}} \cdot \sigma_1\sigma_2 + \left(\frac{1}{X^t} - \frac{1}{X^c}\right) \cdot \sigma_1 + \left(\frac{1}{Y^t} - \frac{1}{Y^c}\right) \cdot \sigma_2 + \frac{\tau_{12}^2}{S^2} = 1 \tag{2.15}$$

where σ_1 is the ply stress in the fibre direction (1 direction), σ_2 is the ply stress perpendicular to the fibre direction (2 direction), τ_{12} is the shear ply stress , X^t is the tensile strength of the ply in the fibre direction, X^c is the compressive strength of the ply in the fibre direction, Y^t is the tensile strength of the ply perpendicular to the fibre direction, Y^c is the compressive strength of the ply perpendicular to the fibre direction and S is the shear strength strength of the ply in MPa.

The advantage of using the Tsai-Wu failure criterion is that it automatically includes the difference in compressive and tensile strength, and, gives good or conservative predictions for various test cases except for biaxial compression [12].

2.7 Fatigue : Composites versus metals

In general, fibre reinforced composites have good fatigue and corrosion resistance. Bathias [15] compares the fatigue damage of metals and composite materials at the microscopic level, after impact, based on endurance curve, effect of loading, and, stress concentration. Though the paper does not study the effect of environment on metallic and composite fatigue, it concludes that the specific endurance strength of metals is generally less than that of composite materials when subjected to cyclic loading. Another important observation is that cyclic compressive loads cause more fatigue damage to composites than cyclic tensile loads.

Alderliesten [16] states that the fatigue phenomena of composites is more complex than metals due to the anisotropic and inhomogeneous behaviour of composites. Several parameters influence the fatigue performance of composites like fibre reinforcement, matrix materials, environmental and loading conditions, and laminate stacking sequence.

2.8 Composite : Fatigue models

Degrieck and Van Paepegem [17] classify the fatigue models for composites into three major categories: fatigue life models, phenomenological models and progressive damage models. Fatigue life models are based on S-N curves and do not take into account the damage mechanism involved in the degradation of material properties. Since they require elaborate experimental work for each loading condition, layup and material, they are not considered in the thesis.

Phenomenological models characterize residual strength or stiffness of a composite specimen in terms of macroscopically observable properties like stiffness or strength. Progressive damage models relate the evolution law that describes stiffness/strength degradation to one or more damage variables which quantifies damage like delamination size.

2.8.1 Progressive damage models

Shokrieh and Lessard [18] proposed the “progressive damage modelling approach” to simulate the fatigue behaviour of composite laminates. The model simulates the residual strength, residual stiffness and fatigue life of laminated composite materials with arbitrary stacking sequence and geometry subjected to arbitrary fatigue loading. The model is based on CLT and consists of three major parts: stress analysis, estimation of damage and degradation of material properties. It is necessary to fully characterize the residual material properties in matrix and fibre directions under uni-axial fatigue loading conditions (tension, compression, in-plane shear and out of plane shear) to use the fatigue failure criteria. Shokrieh and Rafiee [19] performed fatigue analysis of a composite wind turbine blade based on the progressive damage modelling approach in a Finite Element (FE) environment.

Lian and Yao [20] simulated the evolution of fatigue damage of composites with different layup sequences in a FE environment. It is similar to progressive damage modelling as it couples a stiffness degradation model with a strength degradation model for simulation. The fatigue life and fatigue behaviour of six different layup sequences of E-glass/epoxy laminates were experimentally studied and compared with FE results. The simulation yielded good prediction with experimental results except for quasi-isotropic laminate since out of plane effect was neglected. Based on the studies by Shokrieh and Rafiee [19] and Lian and Yao [20], it can be concluded that it is possible to simulate the fatigue failure of the composite T-boom by employing the progressive fatigue damage modelling technique in a FE environment.

Degrieck and Van Paepegem [17] state that " progressive damage models are the most promising tool because they quantitatively account for the progression of damage in the composite structure ". But, the downside of progressive damage modelling is that significant computational and experimental effort is required for the fatigue life prediction of the T-boom which is beyond the scope of this Master thesis.

2.8.2 Phenomenological models

Mao and Mahadevan [21] proposed a phenomenological model based on residual stiffness to predict the fatigue damage of composites. Figure 2.12 shows the comparison of fatigue damage mechanisms for homogeneous and composite materials. The experimental studies of damage growth for composites revealed that composites have 3 stages of damage evolution under fatigue loading. During the first stage, multiple damage modes occur in the material resulting in rapid fatigue damage growth. The damage increases slowly and steadily during the second stage while in the final stages, the damage growth is rapid due to fracture of fibres. Although the model accurately predicts the damage growth of composites in the early and final phases of its life, considerable experimental effort is required to determine model parameters. Also, for the fatigue analysis of an offshore composite structure, the model has to be modified to account for variable amplitude load spectra.

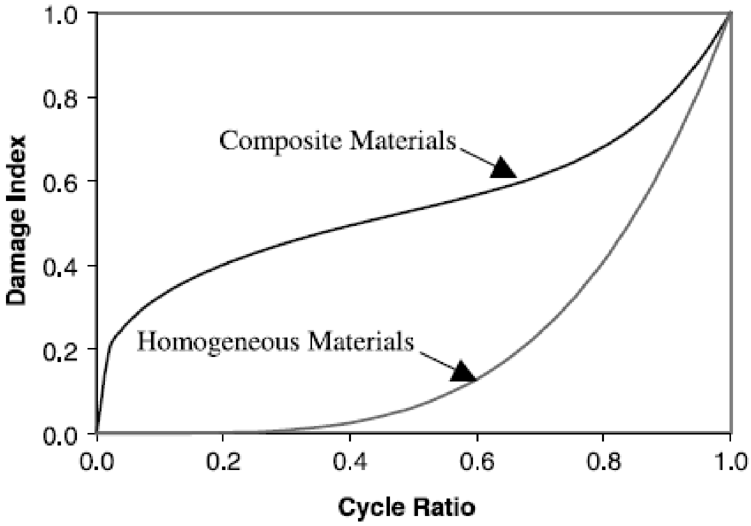

Figure 2.12: Comparison of fatigue damage mechanism [21]

Phenomenological models based on residual strength like Yao and Himmel [22], D'Amore, et al. [23] and residual stiffness like Whitworth [24], Wu and Yao [25] require considerable experiment effort to determine the model parameters which limits their applicability to a specific loading condition, layup and material. Philippidis and Passipoularidis [26] compare and access the validity of various state of the art phenomenological residual strength models by using common experimental data. The authors conclude that “the use of complicated phenomenological models requiring large experimental data sets for implementation does not necessarily pay back in terms of accurate predictions and consequently simple models requiring limited experimental effort should be preferred”. Various damage accumulation rules and residual strength models were fit to numerous constant amplitude and variable amplitude loadings by Post, et al. [27] in order to determine their predictive accuracy. The authors concluded that the use of complex fatigue models did not significantly improve the predictive accuracy relative to simple fatigue models.

Kassapoglou's model [28–30] is based on the residual strength approach and is fundamental as it does not require any curve fitting or experimentally determined parameters for predicting fatigue damage. Another advantage of this model is that no fatigue tests are required for calibrating the fatigue predictions. The author states that “the probability of failure during any cycle is assumed to be constant and equal to the probability of failure obtained from static test results and the associated statistically quantified scatter”.

Hence , the probability of failure between 1 and N cycles is given by [28]:

$$P = N \cdot p \cdot (1-p)^{N-1} \tag{2.16}$$

where N is the number of cycles and p is the probability of failure in each cycle.

The critical number of cycles corresponding to maximum likelihood of failure for the structure is derived by differentiating Eq. (2.16) with respect to N and is given by [28]:

$$N_c = \ln\left(\frac{1}{1-p}\right) \tag{2.17}$$

If the structure experiences tension-compression loads with $\sigma_m > 0$. The probability of failure between 1 and N cycles is analogous to Eq. (2.16) and is given by [28]:

$$P = N\left(p_T + p_C - 2p_T p_C\right)\left(1-p_T\right)^{N-1}\left(1-p_C\right)^{N-1} \tag{2.18}$$

where σ_m is the mean stress during cyclic loading (MPa), p_C is the probability of failure for a single compression cycle and p_T is the probability of failure for a single tension cycle.

Hence for the tension-compression load scenario (R<0), the critical number of cycles corresponding to maximum likelihood for failure is given by [28]:

$$N_c = -\frac{1}{\ln\left(1-p_T\right) + \ln\left(1-p_C\right)} \tag{2.19}$$

where R is the stress ratio.

For example, if the static strengths are described by a two parameter Weibull distribution, the probability of failure for an applied load σ and the critical number of cycles to failure are given by [28]:

$$p = 1 - \mathrm{e}^{-(\sigma/\beta)^{\alpha}} \tag{2.20}$$

$$N_c = \frac{1}{(\sigma_{max}/\beta_T)^{\alpha_T} + (\sigma_{min}/\beta_C)^{\alpha_C}} \tag{2.21}$$

where α and β are the shape and scale (MPa) parameters of the Weibull distribution, σ_{min} and σ_{max} are the minimum and maximum stress during the cyclic loading (MPa), α_T and β_T are the shape and scale (MPa) parameters of the Weibull distribution describing static tensile strength and α_C and β_C are the shape and scale (MPa) parameters of the Weibull distribution describing static compression strength.

The only downside of this approach is that it implicitly assumes that the fatigue and the static failure modes are the same. It does not take into account the failure mode interaction and failure mode change that may occur during fatigue loading. Nevertheless, the model yields a good/conservative predictions for constant amplitude loading stress ratios, R=0 and R<0 and many variable amplitude loading scenarios presented in the papers. The author also states that the model is “useful for preliminary design where fatigue lives can be estimated and alternate designs can be compared to each other on the basis of their expected fatigue performance”. Hence, for the fatigue analysis of the composite T-boom, Kassapoglou's model is used.

Like most fatigue models, Kassapoglou's model also does not take into account the effect of environment to predict the fatigue life of the structure. Hence, the model has to be modified to include the effect of environment on material properties which will be part of the thesis. The methodology to incorporate the effect of environment in the Kassapoglou's model is described in Section 3.5.

2.9 Material system and material characterization tests

The resin systems that are commonly used for marine applications are polyester, vinylester and epoxy [3–5]. Kootsookos and Mouritz [31] studied the durability of glass/polyester, carbon/polyester, glass/vinyl ester and carbon/vinyl ester composites when immersed in seawater. The authors observed a significant reduction in flexural modulus and strength of these composites due to moisture absorption and degradation of resin matrix. Hence, epoxy resins are considered for the T-boom design as they have better resistance to water absorption and chemicals while carbon and glass fibres are considered as candidate materials for reinforcements.

Akbar and Zhang [32] state that the environment resistance of polymer composites are mainly dependant on the matrix. Matrix plasticization and degradation of the fibre/matrix interface are the two possible effects of moisture absorption on composites systems [33–35]. In epoxy matrix composites, moisture absorption generally leads to a plasticizer effect due to the reduction of glass transition temperature, T_g (°C) of the matrix [36], and subsequently, a degradation in material properties. To incorporate the effect of environment in Kassapoglou's model, it is important to :

1. quantify the moisture ingression behaviour of epoxy laminates as a function of time, and,
2. characterize tension and compression properties of the epoxy laminates at different moisture levels and temperature.

2.9.1 Moisture absorption properties

The research performed by Wright [37], Vodicka [38] and Ray [39] suggest that the moisture diffusion characteristics of epoxy laminates can be approximated by Fickian behaviour. A Fickian material is defined as a material whose moisture absorption and desorption behaviour follows Fick's law. Moisture equilibrium content and moisture diffusivity are the 2 moisture absorption properties of a Fickian material. ASTM D 5229/D 5229M —92 describes the method to determine the moisture properties and equilibrium moisture conditioning of polymer matrix composite materials. The average moisture content expressed in percentage (%) is given by Eq. (2.22).

$$M_{gain}\% = \frac{W_i - W_o}{W_o} \cdot 100 \tag{2.22}$$

where W_i and W_o are the current and baseline specimen mass in mg.

The through thickness diffusivity (mm/s^2) of the specimen is given by Eq. (2.23).

$$D = \pi \left(\frac{h_{spec}}{4M_m}\right)^2 \left(\frac{M_2 - M_1}{\sqrt{t_2} - \sqrt{t_1}}\right)^2 \tag{2.23}$$

where h_{spec} is the average specimen thickness (mm), M_m is the effective moisture content (%) and M_i is the moisture content at time t_i (%).

2.9.2 Data pooling

In order to determine the effect of moisture and temperature on tensile and compressive properties mentioned in point 2, tests have to be performed at various environment conditions (moisture contents and temperature levels). ASTM D 6641/D 6641M and ASTM D 3039/D 3039M describe the test method to determine the compressive and tensile properties of polymer matrix composites respectively.

Evaluating the tensile and compressive properties at various moisture contents and temperature levels require a lot of testing, money, time and effort. Data pooling using regression analysis is used to limit the number of tests at various test conditions. Regression analysis enables the pooling of data at different environment conditions such as different moisture contents and temperatures, to improve the understanding of the effect of certain parameters like moisture or temperature on material properties. Also, by pooling similar data, sufficient data is obtained to calculate basis values.

Data pooling implicitly assumes that batch to batch variability is negligible. Hence, it is important to check for batch to batch variability before data pooling because if this is not the case, the results from pooling might be too optimistic [40]. It is also important to ensure that there is statistical equivalency of variability across environments and no significant change of failure modes for each environment.

Shyprykevich [41] and Tomblin, et al. [42] describe the general methodology for data pooling and fitting the data to Weibull and normal distribution respectively. In general, using Weibull distribution to fit data, results in conservative material basis values [40].

2.10 Research questions and sub-goals

Based on the literature study, the research questions and sub-questions for the Master thesis are formulated and are as follows:

- Which truss based design concept yields the highest possible weight savings within the time frame of a Master thesis?
    1. What is the margin of safety for the design?
    2. What is the most suitable finite element model for the composite T-boom with respect to the following aspects?
        - Modelling and computational time
        - Accuracy of results
        - Budget for testing and validation of results
    3. What is the most suitable material system for the composite T-boom with respect to the following aspects?
        - Cost
        - Specific strength and specific stiffness
        - Fatigue and environment resistance
- What is the fatigue life of the composite T-boom using the modified Kassapoglou's model?
    1. What are the effects of moisture and temperature on material properties?
        - How many coupons should be tested?
        - What are the dimensions of the coupon?
        - What are the humidity and temperatures levels at which testing has to be done?
            - ∗ Is data pooling possible? If yes, what are the basis values of material properties?
        - What is the duration of testing?
    2. What is the fatigue test plan to validate the Kassapoglou's model?
        - How many coupons should be tested?
        - What are the dimensions of the coupon?
        - Which standards should be followed for testing?
        - What are the load levels at which the coupons have to be tested?
        - What is the duration of testing?

In the first research question, the design of the composite T-boom is addressed. The main goal here is to design a truss based composite T-boom which yields a maximum weight saving while satisfying the core requirements of Ampelmann and the design requirements. The research performed by Li, et al. [43] and Shen, et al. [44] suggest that FE analysis provides accurate results for the static and dynamic analysis of FRP bridge structures. Hence, FE analysis will be performed to determine whether the composite gangway satisfies the design requirements like strength and deflection. During the FE analysis, it is necessary to make a sound judgement on the method in which the T-boom will be modelled. It is highly desirable for Ampelmann to model the T-boom which is not computationally expensive, yields accurate results and requires minimal budget for validation of results.

In the second research question, the fatigue behaviour of the composite T-boom is addressed. The main goal here is to develop a modified Kassapoglou's model which takes into account the effect of moisture and temperature with minimal experimental effort. The modified fatigue model should be simple and yield accurate or conservative results of fatigue life. The first task is to characterize the material properties with respect to moisture and temperature and subsequently incorporate the results in the existing model. The next task is to determine the fatigue life of the T-boom and validation of the analytical predictions by fatigue testing of the coupons.

2.11 Chapter summary

Various design concepts for the composite T-boom are reviewed and a side truss stiffened panel design is selected. As there are no offshore composite standards for the gangway, it is assumed that the structure is similar to a pedestrian bridge as their primary functionalities are the same. Subsequently, the load cases and design requirements for the composite T-boom are formulated based on standards and specifications. Various composite fatigue models are reviewed and Kassapoglou's model is selected for the estimation of fatigue life of T-boom. Epoxy laminate reinforced with glass or carbon fibre is selected as the material system for the T-boom design and test methods to characterize its material properties with respect to environment are reviewed. Finally, the research questions and sub-questions are formulated based on the conclusions of literature study.

Chapter 3

Methodology

This chapter discusses the methodology to design and perform fatigue analysis of the composite Telescoping boom (T-boom).

3.1 Preliminary design of the composite T-boom

The preliminary design of the composite T-boom is based on the equivalent stiffness approach. In this method, each and every truss member of the existing design is replaced by a Fibre Reinforced Polymer (FRP) box beam of equivalent stiffness. The notation of the truss members of the existing T-boom are shown in Figure 3.1.

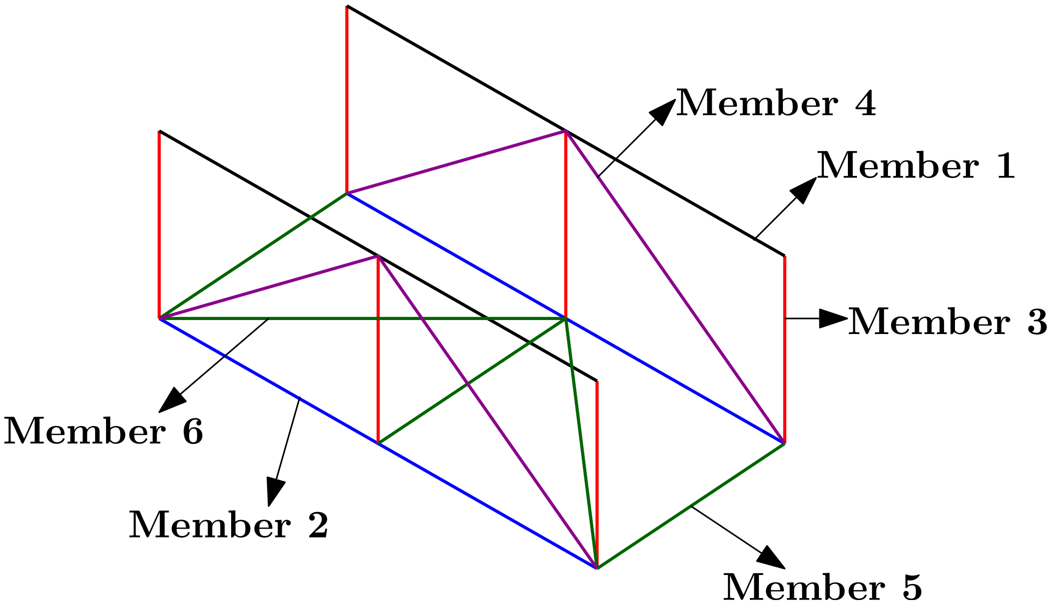

Figure 3.1: Notation of the truss members of the T-boom

In Figure 3.1, member 1 denotes the top chord, member 2 is the bottom chord, member 3 is the vertical bracing, member 4 is the vertical diagonal bracing, member 5 is the bottom horizontal bracing and member 6 is the bottom diagonal bracing.

In the preliminary design phase, it is assumed that:

- Members 1 and 2 are purely in bending and,
- Members 3-6 are axially loaded and act as buckling arresters.

Based on the above assumptions and applying equivalent stiffness approach for the composite T-boom,
for the top and bottom chord members,

$$E_{1m}A_{box} \geq (EA)_{steel} \tag{3.1}$$

$$E_{1b}I_{box,x1} \geq (EI)_{steel,x1} \tag{3.2}$$

$$E_{1b}I_{box,y1} \geq (EI)_{steel,y1} \tag{3.3}$$

for the bracings,

$$E_{1m}A_{box} \geq (EA)_{steel} \tag{3.4}$$

$$E_{1m}I_{box,x1} \geq (EI)_{steel,x1} \tag{3.5}$$

$$E_{1m}I_{box,y1} \geq (EI)_{steel,y1} \tag{3.6}$$

where A_{steel} is the area of the steel beam (mm^2), E_{steel} is the modulus of elasticity of steel (GPa), $I_{steel,x1}$ is the moment of inertia of the steel beam in the x_1 axis (mm^4) and $I_{steel,y1}$ is the moment of inertia of the steel beam in the y_1 axis (mm^4). The modulus of elasticity of steel is assumed to be 210 GPa.

Eq. (3.5) and Eq. (3.6) imply that the buckling modulus of the composite beam in the x_1 and y_1 should be equal to or greater than the corresponding buckling modulus of the steel beam. The cross-section details of the chords and bracings are given in Appendix A. The axial and bending stiffness of the chords and bracings of the existing design are shown in Table 3.1.

Table 3.1: Axial and bending stiffness of the chords and bracings

Member	A_{steel} (mm^2)	EA_{steel} ($\times$ 10^7 N)	I_{steel} ($\times$ 10^5 mm^4)		EI_{steel} ($\times$ 10^{10} N·mm^2)	
			x_1	y_1	x_1	y_1
1	736	15.5	2.62	2.62	5.5	5.5
2	2144	45	24.9	7.67	52.3	16.1
3	736	15.5	2.62	2.62	5.5	5.5
4	576	12.1	1.26	1.26	2.64	2.64
5	475	9.98	1.13	1.13	2.37	2.37
6	475	9.98	1.13	1.13	2.37	2.37

In fact, the assumption that only members 1 and 2 of the T-boom experience bending stress is not entirely true. In reality, the bending stiffness of the T-boom also depends on members 3-6. As a result, the bending stiffness estimation of the T-boom is quite conservative, since it assumes that only 2 members are in bending.

3.1.1 Material system

The material system selected for the design of the composite T-boom is Hexply 8552/IM7. It is an unidirectional prepreg with a tough epoxy matrix and continuous, intermediate modulus carbon fibres as reinforcements. It has high specific strength and specific stiffness with good damage tolerance and impact resistance for a variety of applications. The product data sheet is shown in Appendix B.

For a quasi-isotropic layup, [45/-45/0/90]s, the ABD matrix is given by Eq. (3.7).

$$ABD = \begin{bmatrix} 8.5281 & 2.7295 & 0 & 0 & 0 & 0 \\ 2.7295 & 8.5281 & 0 & 0 & 0 & 0 \\ 0 & 0 & 2.8893 & 0 & 0 & 0 \\ 0 & 0 & 0 & 0.9543 & 0.5489 & 0.1630 \\ 0 & 0 & 0 & 0.5489 & 0.7369 & 0.1630 \\ 0 & 0 & 0 & 0.1630 & 0.1630 & 0.5699 \end{bmatrix} \cdot 10^4 \tag{3.7}$$

The E_{1m} and E_{1b} are calculated using Eq. (2.3) and Eq. (2.5) respectively and are given by:

$$E_{1m} = 62.78 \text{ GPa} \tag{3.8}$$

$$E_{1b} = 36.12 \text{ GPa} \tag{3.9}$$

Substituting equations Eq. (3.8) and Eq. (3.9) in Eq. (3.1), Eq. (3.2), Eq. (3.3) and Eq. (3.4), *for the top and bottom chord members,*

$$A_{box} \geq 3.345\,(A)_{steel} \tag{3.10}$$

$$I_{box,x1} \geq 5.81\,(I)_{steel,x1} \tag{3.11}$$

$$I_{box,y1} \geq 5.81\,(I)_{steel,y1} \tag{3.12}$$

for the bracings,

$$A_{box} \geq 3.345\,(A)_{steel} \tag{3.13}$$

$$I_{box,x1} \geq 3.345\,(I)_{steel,x1} \tag{3.14}$$

$$I_{box,y1} \geq 3.345\,(I)_{steel,y1} \tag{3.15}$$

It is impossible to satisfy the above requirements for the chords and bracings without violating the design space constraints of the T-boom. Hence, a quasi-isotropic layup is not used for the design of the flanges and webs of the FRP beam.

3.1.2 Cost implication

If we consider only the material costs, the choice of a carbon fibre-epoxy system for the design of the composite T-boom may seem to violate the precept of cost competitiveness laid down by Amplemann in Section 1.3. Nevertheless, this option may lead to an overall reduction in the life cycle costs if we consider the lower fuel consumption resulting from the light-weight design or the reduction in maintenance cost resulting from the ruggedness of this design as observed in FRP bridges [45–47]. Estimating the life cycle costs of the T-boom is beyond the scope of this mater thesis, however, a detailed investigation in the future may prove to be interesting. A preliminary investigation of the cost incurred by Ampelmann to manufacture and maintain the composite T-boom is described in Section 4.9.

3.1.3 Design guidelines/ Rules of thumb

The layup of the flanges and webs of the FRP box beam of the composite T-boom are determined based on a set of design guidelines recommended by Kassapoglou [12]. The rules of thumb used for designing the layup of the webs and flanges are the following:

(a) The layup should be symmetric in order to avoid membrane/bending coupling, B matrix is zero.

(b) The layup should be balanced in order to avoid stretching/shear coupling, A_{16}=A_{26}=0.

(c) Minimize bending/twisting coupling, D_{16} and D_{26} terms, by grouping $+\theta$ and $-\theta$ together.

(d) At least 10% fibres in the four principal directions: 0,+45,-45 and 90 to protect against secondary load cases.

(e) Limit the number of unidirectional fibres having the same orientation next to each other to 4-5 plies in order to arrest microcracks and minimizing the probability of creating delaminations.

(f) Placing the 0° plies far away from the neutral axis to improve the bending stiffness by maximizing D_{11}.

(g) Placing the 45/-45 plies far away from the neutral axis to improve panel buckling and crippling by maximizing D_{66}.

(h) The minimum web height should be 18 mm to make fabrication easier and avoid damage during handling.

Kassapoglou [12] suggests that it is a good practice to have atleast 25% 0° and 25% 45° plies for the flange designs as a comprise between high D_{11} and high D_{66}. Based on the design guidelines, the layup options considered for the composite T-boom design are shown in Table 3.2.

Table 3.2: Layup choices for the composite T-boom

	% 0/45/-45/90
Option A	30/30/30/10
Option B	40/25/25/10

Since T-boom is a stiffness based design , it is highly desirable to use more number of 0° plies as it increases the overall bending stiffness. Option B is the maximum number of 0° plies possible for a laminate based on the design guidelines. Option A is considered to study the effect of decreasing the 0° plies on the deflection and stresses of the composite T-boom.

3.1.4 Design strategy

The composite T-boom design is subject to a number of design space constraints to ensure that it perfectly fits inside the Main Boom (MB). The design space constraints are listed below:

(a) The length of the composite T-boom should be 13.12 m.

(b) The height of the composite T-boom should be 0.9 m.

(c) The width of the composite T-boom should be 0.87 m.

(d) The horizontal distance between the top chord members and vertical members should be 0.77 m to ensure easy and safe transfer of people.

(e) The maximum allowable a_{box} is 150 mm in order to reduce the wind loads and enable easy assembly of members 3-6.

Based on the design space constraints, the cross-section properties of the box beam ($A_{box,beam}$ and $I_{box,beam}$) can be increased by increasing the:

(a) a_{box} of the box beam, see Figure 2.7, or,

(b) t_{box} of the box beam, see Figure 2.7.

The effect of increasing the a_{box} and t_{box} on the moment of inertia and weight were studied for a steel box beam of L_{box}=1000 mm. The mass and moment of inertia of a box beam are given by Eq. (3.16) and Eq. (3.17).

$$M_{box,beam} = \rho_{steel} \cdot (a_{box} \cdot b_{box} - (a_{box} - 2 \cdot t_{box}) \cdot (b_{box} - 2 \cdot t_{box})) \cdot L_{box} \tag{3.16}$$

$$I_{box,beam} = (\frac{1}{12} a_{box}^3 \cdot b_{box} - \frac{1}{12}(a_{box} - 2 \cdot t_{box})^3 \cdot (b_{box} - 2 \cdot t_{box})) \tag{3.17}$$

where $M_{box,beam}$ is the mass of the box beam (kg), $I_{box,beam}$ is the moment of inertia of the box beam in the x_1 axis (mm^4) and ρ_{steel} is the density of steel (kg/mm^3). The density of steel is assumed to be 8050 kg/m^3.

Figure 3.2 and Figure 3.3 shows the plot of $I_{box,beam}/M_{box,beam}$ while varying the a_{box} and t_{box} of the box section respectively. The plots are used only for trend study, and, the values do not have any significance on the actual design of the composite T-boom.

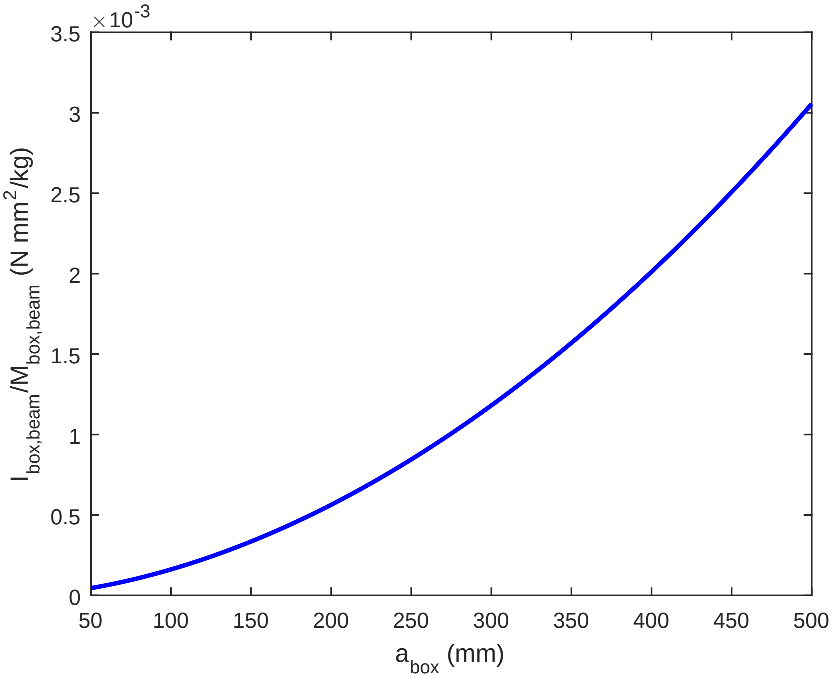

Figure 3.2: Variation of $I_{box,beam}/M_{box,beam}$ with a_{box} for $t_{box} = 4$ mm

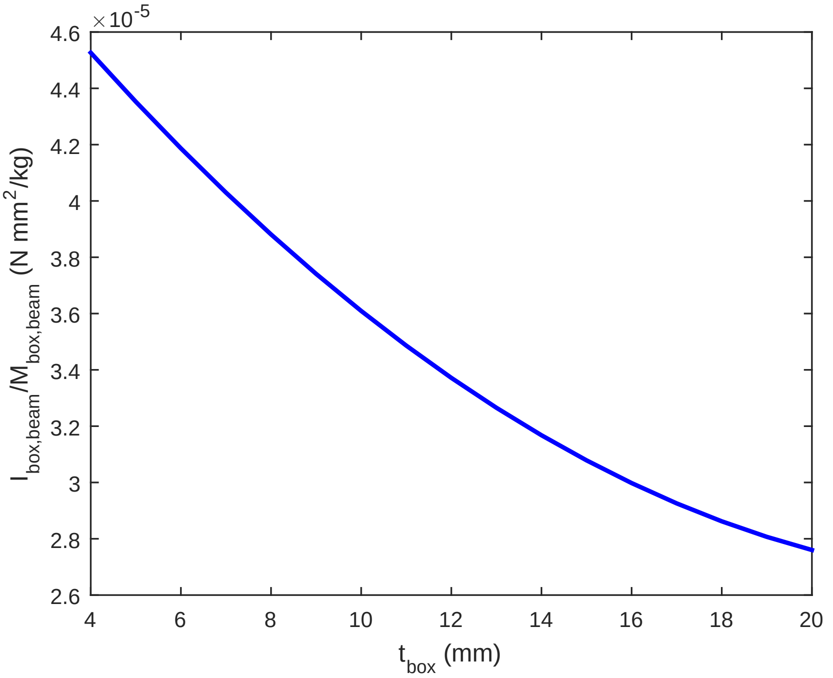

Figure 3.3: Variation of $I_{box,beam}/M_{box,beam}$ with t_{box} for $a_{box} = 50$ mm

It can be inferred from Eq. (3.16) and Eq. (3.17) that $M_{box,beam}$ and $I_{box,beam}$ increases when either a_{box} or t_{box} is increased. But the ratio, $I_{box,beam}/M_{box,beam}$ decreases when t_{box} is increased while the same increases when a_{box} is increased. Also, the ratio has a higher order of magnitude for the latter by a factor of approximately 100. This implies that it is more advantageous to increase the a_{box} than t_{box} to get higher cross-sectional properties without adding considerable weight. Hence, for a specific layup choice (refer Table 3.2), the required cross-sectional properties for the chords and bracings are obtained by first increasing the a_{box} till 150 mm, and, subsequently increasing the t_{box} till Eq. (3.1) and Eq. (3.2) are satisfied for the chords, and, Eq. (3.3) and Eq. (3.4) are satisfied for the bracings.

Kassapoglou [12] suggests that material failure should not be preceded by some stability failure (like crippling and column buckling) as it leads to a heavy design. The author also states that crippling is the preferred primary failure mode over column buckling. Therefore, this design guideline is also followed during the preliminary design phase of this thesis. The design variables of the preliminary design phase of the composite T-boom are the following:

(a) n_{plies}, number of plies

(b) a_{box}

(c) b_{box}

(d) layup of the web and flange

(e) L_{box}

A Matalab code shown in Appendix C is written, where the design variables are given as input and the outputs are the following:

(a) Checks if the mass of the FRP box beam is less than the mass of the corresponding steel member.

(b) Calculates the axial and bending stiffness of the FRP box beam.

The results of the preliminary design of the composite T-boom are discussed in Section 4.1. The CATIA drawing of the the preliminary design along with the cross-section properties of its truss members are given in Appendix D. The mass of the composite T-boom after the preliminary design, m_{Tboom} is 520 kg.

3.2 Finite Element (FE) analysis of the composite T-boom

Research carried out by Davalos and Qiao [48], Lee and Lee [49] and Kim and Choi [50] suggest that shell elements are a good approximation to model FRP beams as their thickness is considerably less than the other two dimensions. Shen, et al. [44] and Singh and Chawla [51] analysed the structural response of FRP beams in ABAQUS using S4R elements and concluded that the FE results are in good agreement with analytical and experimental results. S4R element is a 4-node shell element with reduced integration to avoid membrane and shear locking [52].

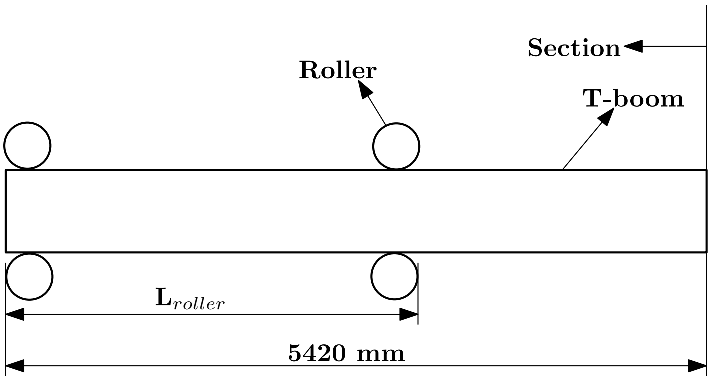

Figure 3.4: Location of the rollers and section for the FE model

S4R elements are used to model the composite T-boom to predict its deflection and stress distribution. For the verification purpose, a box FRP beam is modelled in ABAQUS using S4R elements and compared with results published by Bank and Bednarczyk [53]. The results of the analysis are shown in Appendix E. As mentioned in Section 2.6, Tsai-Wu failure criterion is used to predict the first ply failure load of the composite T-boom, and, the first ply failure load is regarded as the ultimate failure load of the laminate. The Tsai-Wu failure criterion is expected to give conservative predictions of the ultimate failure load of the composite T-boom because of the following reasons:

(a) The ultimate failure load of the laminate is generally greater than the first ply failure load of the laminate.

(b) The composite T-boom is primarily loaded in bending, and, hence Tsai-Wu failure criterion gives good/conservative predictions for bending load scenarios.

The T-boom is connected to the MB by means of 4 rollers (2 each on the MB and T-boom). The distance between the rollers, L_{roller} is 5040 mm for all load cases except Emergency Operation- Extra Length + Cargo (EO-ELC). The distance between the rollers for EO-ELC is 3040 mm. It is computationally expensive to mesh the entire T-boom as its length is too large. Hence, analysis is done at regions close to the rollers since they are the critical regions. A section is taken at 5420 mm from the end roller as shown in the Figure 3.4. Shear force and bending moments are evaluated at this location and subsequently used in the FE model.

The T-boom section used in the FE model is shown in Figure 3.5. The mass and length of the remaining section of the composite T-boom are 306 kg and 7885 mm respectively. Based on Table 2.2, it can be concluded that the worst load cases are Emergency Operation- 3 People Transfer (EO-3PT), EO-ELC and Stowed Condition (SC). The detailed calculation of the shear forces and bending moments due to these load cases are shown in Appendix F. The shear forces and bending moments acting at the section due to different loads in the EO-3PT, EO-ELC and SC are shown from Table 3.3 to Table 3.8. The shear forces and bending moments due to the self weight, live mass, weight of the tip and wind are applied at the centre of area (c.o.a.) of the cross-section (see right view of Figure 3.5) while the shear forces and bending moments due to slewing and telescopping are applied at the bottom chords. For example, SF_x corresponds to the shear force acting the x axis, and, BM_z corresponds to bending moment acting in the z axis due to the forces acting in the x direction.

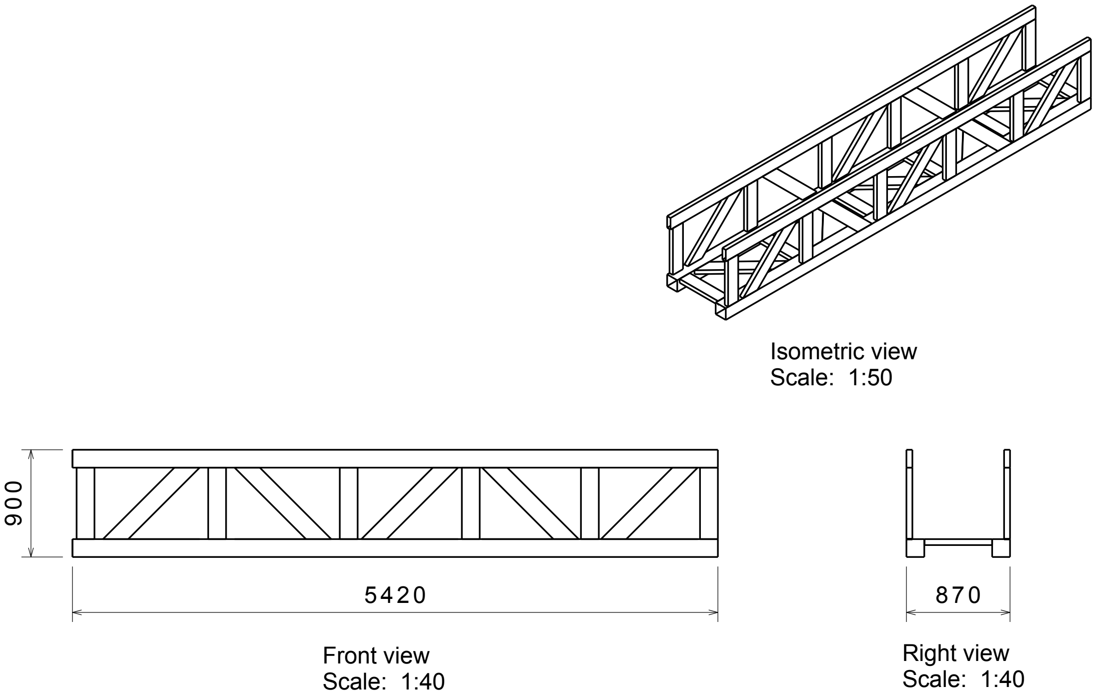
Isometric view
Scale: 1:50
900
5420
870
Front view
Scale: 1:40
Right view
Scale: 1:40

Figure 3.5: T-boom section used in the FE model

Table 3.3: Shear forces and bending moments due to reaction forces at the tip

Loads	Unit	EO-3PT	EO-ELC	SC
SF_x	N	0	0	4.96×10^4
SF_y	N	0	0	5.05×10^3
SF_z	N	0	0	2.02×10^4
BM_x	N·mm	0	0	1.81×10^8
BM_z	N·mm	0	0	-4.45×10^8

Table 3.4: Shear forces and bending moments due to live mass

Loads	Unit	EO-3PT	EO-ELC	SC
SF_x	N	-1.73×10^2	-3.04×10^2	0
SF_y	N	-5.90×10^2	-1.38×10^2	0
SF_z	N	-3.95×10^3	-2.85×10^3	0
BM_x	N·mm	-3.55×10^7	-2.56×10^7	0
BM_z	N·mm	1.55×10^6	2.73×10^6	0

Table 3.5: Shear forces and bending moments due to self-weight

Loads	Unit	EO-3PT	EO-ELC	SC
SF_x	N	-1.53×10^2	-4.04×10^2	0
SF_y	N	-5.24×10^2	-1.84×10^2	-1.51×10^3
SF_z	N	-3.51×10^3	-3.79×10^3	-6.02×10^3
BM_x	N·mm	-1.38×10^7	-1.49×10^7	-2.37×10^7
BM_z	N·mm	6.04×10^5	1.59×10^6	0

Table 3.6: Shear forces and bending moments due to slewing and telescopping

Loads	Unit	EO-3PT	EO-ELC	SC
SF_x	N	-10^3	0	0
SF_y	N	-10^4	0	0
SF_z	N	-10^3	0	0
BM_x	N·mm	-8.99×10^6	0	0
BM_z	N·mm	8.99×10^6	0	0

Table 3.7: Shear forces and bending moments due to weight of the tip

Loads	Unit	EO-3PT	EO-ELC	SC
SF_x	N	-0.91×10^2	-2.40×10^2	0
SF_y	N	-3.11×10^2	-1.09×10^2	-8.94×10^2
SF_z	N	-2.08×10^3	-2.25×10^3	-3.57×10^3
BM_x	N·mm	-1.76×10^7	-1.90×10^7	-3.01×10^7
BM_z	N·mm	7.68×10^5	2.03×10^6	0

Table 3.8: Shear forces and bending moments due to wind

Loads	Unit	EO-3PT	EO-ELC	SC
SF_x	N	-2.01×10^3	-2.01×10^3	-1.96×10^4
SF_y	N	0	0	0
SF_z	N	0	0	0
BM_x	N·mm	0	0	0
BM_z	N·mm	7.93×10^6	7.93×10^6	7.71×10^7

A convergence study of the FE model of the T-boom section is performed to determine the ideal element edge length for the static analysis. The vertical z-axis deflection at a point and strain energy of the whole model are determined for element edge lengths = 20 mm, 30 mm, 40 mm, 50 mm and 60 mm with self-weight as the load and roller supports as the constraint. The meshed model of the composite T-boom of element edge length = 50 mm is shown in Figure 3.6.

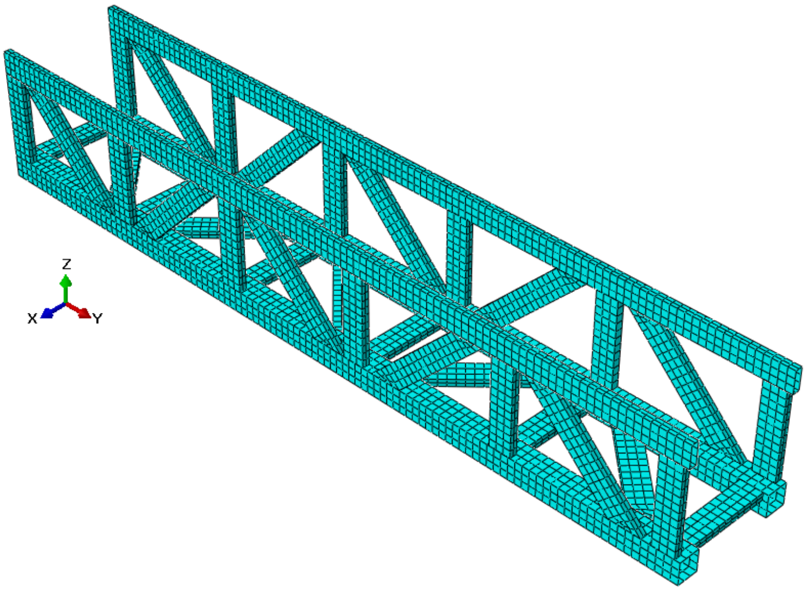

Figure 3.6: Meshed model of the T-boom section of element edge length = 50 mm

The vertical displacement is measured at point 2 whose coordinates are (-435, 2587, 100) with respect to point 1 shown in Figure 3.7. Figure 3.8 shows the plot of vertical displacement at point 2 for various element edge lengths. The vertical displacement at point 2 and the strain energy for the whole model for different element edge lengths are shown in Table 3.9.

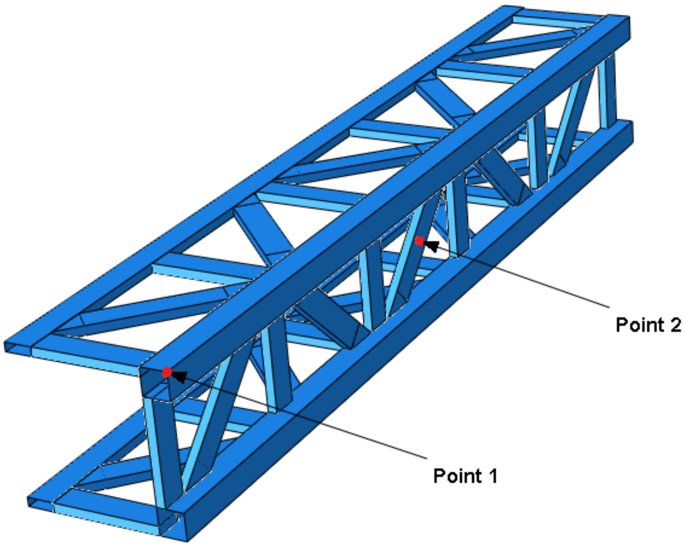

Figure 3.7: Location of point 1 and 2 in the T-boom section

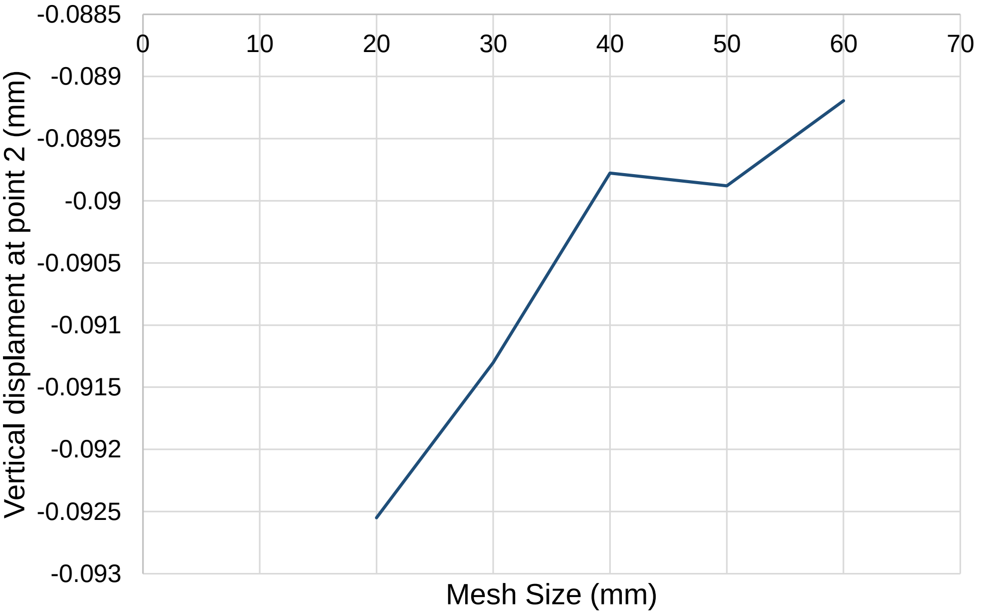

Figure 3.8: Vertical displacement at point 2 for various element edge lengths

Table 3.9: Maximum displacement and strain energy for various element edge lengths

Element edge length (mm)	Vertical displacement at point 2 (mm)	Strain energy (J)
20	-0.09255	103.075
30	-0.0913	101.725
40	-0.0898	100.22
50	-0.0899	100.393
60	-0.0892	100.065

The deviation from the decreasing trend for the vertical displacement at element edge length = 40 mm might be due to the stability issues of the FE model where the displacement tend to oscillate around a mean value for coarse element edge lengths and subsequently stabilize and converge at finer element edge lengths. The % difference between the strain energy of the whole model and vertical displacement at point 2 for element edge lengths = 20 and 50 mm are only 2.67% and 2.97% respectively. Hence, for the static analysis of the composite T-boom, an element edge length of 50 mm is used.

3.3 Detailed analysis of the composite T-boom

In the detailed analysis of the composite T-boom, the parameters that are estimated are the following:

(a) Global deflection of the gangway retrofitted with the composite T-boom

(b) Natural frequency of the gangway in bending retrofitted with the composite T-boom

(c) Global column buckling load of the composite T-boom

As it is computationally expensive to model the entire T-boom in a FE environment, these parameters are determined analytically.

3.3.1 Global deflection of the gangway

Ampelmann estimates the global deflection of the gangway in the horizontal x and vertical z direction by modelling it as a beam clamped at one end and subjected to a tip load at the other end. The beam model of the gangway subjected to a tip force is shown in Figure 3.9.

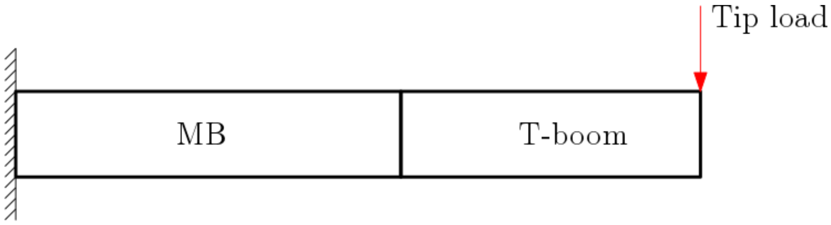

Figure 3.9: Schematic beam model of the gangway subjected to a tip load

As the bending stiffness of the MB and T-boom are different, the displacement of the applied load is split into two parts. The bending stiffness of the T-boom is estimated by calculating the bending stiffness of members 1 and 2 about the centre mass of the T-boom cross-section. The cross-section details of the composite T-boom design are shown in Appendix D. Also, the effect of rotation of the MB on the displacement of the T-boom is considered as an additional displacement. For the vertical displacement, the effect of self-weight is taken into account by assuming a uniformly distributed load over its length.

The vertical deflection of the MB due to tip load is given by,

$$w_{MB,tipload,z} = \frac{1}{3}\frac{F_z \cdot L_{MB}^3}{EI_{MB,x}} + \frac{1}{2}\frac{F_z \cdot L_{MB}^2}{EI_{MB,x}} \cdot L_{Tboom} \tag{3.18}$$

where $w_{MB,tipload,z}$ is the vertical deflection of the MB due to tip load (mm), F_z is the vertical tip load (N), L_{MB} is the length of the MB (mm), $EI_{MB,x}$ is the bending stiffness of the MB along the x axis ($\mathrm{N} \cdot \mathrm{mm}^2$) and L_{Tboom} is the length of the T-boom (mm).

The vertical deflection of the T-boom due to tip load is given by,

$$w_{Tboom,tipload,z} = \frac{1}{3}\frac{F_z \cdot L_{Tboom}^3}{EI_{Tboom,x}} + \left(\frac{1}{2}\frac{F_z \cdot L_{MB}^2}{EI_{MB,x}} + \frac{F_z \cdot L_{MB} \cdot L_{Tboom}}{EI_{MB,x}}\right) \cdot L_{Tboom} \tag{3.19}$$

where $w_{Tboom,tipload,z}$ is the vertical deflection of the T-boom due to tip load (mm) and $EI_{Tboom,x}$ is the bending stiffness of the T-boom along the x axis ($\mathrm{N} \cdot \mathrm{mm}^2$).

The vertical deflection of the MB due to self-weight is given by,

$$w_{MB,sw,z} = \frac{1}{8}\frac{q_{MB} \cdot L_{MB}^4}{EI_{MB,x}} + \left(\frac{1}{3}\frac{L_{MB}^3}{EI_{MB,x}} + \frac{1}{2}\frac{L_{MB}^2}{EI_{MB,x}} \cdot \frac{L_{Tboom}}{2}\right) \cdot q_{Tboom} \cdot L_{Tboom} \tag{3.20}$$

where $w_{MB,sw,z}$ is the vertical deflection of the MB due to self-weight (mm) and q_{MB} and q_{Tboom} are the mass of the MB and T-boom times the gravity constant divided by their length respectively (N/mm).

The vertical deflection of the T-boom due to self-weight is given by,

$$\begin{aligned} w_{Tboom,sw,z} = \frac{1}{8}\frac{q_{Tboom} \cdot L_{Tboom}^4}{EI_{Tboom,x}} + \frac{1}{6}\frac{q_{MB} \cdot L_{MB}^3}{EI_{MB,x}} \cdot L_{Tboom} + \\ \left(\frac{1}{2}\frac{L_{MB}^2}{EI_{MB,x}} + \frac{L_{MB}}{EI_{MB,x}} \cdot \frac{L_{Tboom}}{2}\right) \cdot q_{Tboom} \cdot L_{Tboom}^2 \end{aligned} \tag{3.21}$$

where $w_{Tboom,sw,z}$ is the vertical deflection of the T-boom due to self-weight (mm).

The vertical deflection of the gangway is given by,

$$w_{gangway,z} = w_{MB,tipload,z} + w_{Tboom,tipload,z} + w_{MB,sw,z} + w_{Tboom,sw,z} \tag{3.22}$$

The horizontal deflection of the MB due to tip load is given by,

$$w_{MB,tipload,x} = \frac{1}{3}\frac{F_x \cdot L_{MB}^3}{EI_{MB,z}} + \frac{1}{2}\frac{F_x \cdot L_{MB}^2}{EI_{MB,z}} \cdot L_{Tboom} \tag{3.23}$$

where $w_{MB,tipload,x}$ is the horizontal deflection of the MB due to tip load (mm), F_x is the horizontal tip load (N) and $EI_{MB,z}$ is the bending stiffness of the MB along the z axis ($\text{N} \cdot \text{mm}^2$).

The horizontal deflection of the T-boom due to tip load is given by,

$$w_{Tboom,tipload,x} = \frac{1}{3}\frac{F_x \cdot L_{Tboom}^3}{EI_{Tboom,z}} + \left(\frac{1}{2}\frac{F_x \cdot L_{MB}^2}{EI_{MB,z}} + \frac{F_x \cdot L_{MB} \cdot L_{Tboom}}{EI_{MB,z}}\right) \cdot L_{Tboom} \tag{3.24}$$

where $w_{Tboom,tipload,x}$ is the horizontal deflection of the T-boom due to tip load (mm) and $EI_{Tboom,z}$ is the bending stiffness of the T-boom along the z axis ($\text{N} \cdot \text{mm}^2$).

The horizontal deflection of the gangway is given by,

$$w_{gangway,x} = w_{MB,tipload,x} + w_{Tboom,tipload,x} \tag{3.25}$$

3.3.2 Natural frequency of the gangway in bending

Ampelmann analytically estimates the natural frequencies of the gangway in bending by modelling it as a cantilever beam and neglecting the MB/T-boom interface.

The natural frequency of the gangway in bending in the horizontal direction is given by [54]:

$$f_x = \frac{1}{2\pi}\sqrt{\frac{3EI_{avg,z}}{(0.2235M + SWL) \cdot L_{gangway}^3}} \tag{3.26}$$

where f_x is the natural frequency of the gangway in bending in the horizontal direction (Hz), $EI_{avg,z}$ is the length average bending stiffness of the MB and T-boom in the z axis (N · mm^2), M is the mass of the gangway (kg), $L_{gangway}$ is the length of the gangway (mm) and SWL is the safe working load (kg) .

The natural frequency of the gangway in bending in the vertical direction is given by [54]:

$$f_z = \frac{1}{2\pi}\sqrt{\frac{3EI_{avg,x}}{(0.2235M + SWL) \cdot L_{gangway}^3}} \tag{3.27}$$

where f_z is the natural frequency of the gangway in bending in the vertical direction (Hz) and $EI_{avg,x}$ is the length average bending stiffness of the MB and T-boom in the z axis (N · mm^2)

3.3.3 Global column buckling load of the composite T-boom

The global column buckling load of the T-boom is estimated by modelling the gangway as a simply supported beam and is given by

$$P_{column,Tboom} = \pi^2 \frac{EI_{Tboom}}{L_{Tboom}^2} \tag{3.28}$$

where,

$$EI_{Tboom} = \begin{cases} EI_{Tboom,x} & \text{if } EI_{Tboom,x} < EI_{Tboom,z} \\ EI_{Tboom,z} & \text{if } EI_{Tboom,x} \geq EI_{Tboom,z} \end{cases}$$

where $P_{column,Tboom}$ is the column buckling load of the T-boom (N) and EI_{Tboom} is the minimum bending stiffness of the T-boom (N · mm^2).

Since the estimate of the bending stiffness of the T-boom is quite conservative, the parameters calculated during the detailed analysis phase are also conservative. The results of the detailed analysis are described in Section 4.3. It is observed that there is a reduction in the global deflection of the gangway in the horizontal and vertical direction by 6.25% and 18% respectively. Also, there is an increase in the natural frequency of the gangway in the horizontal and vertical direction by 33.1% and 42.86% respectively. The reduction in the global deflection, and, increase in the natural frequency of the gangway are attributed to the increase in the bending stiffness, and, reduction in the mass of the composite T-boom. After the detailed analysis, the next phase is to characterize the degradation of material properties for different environment conditions, and, subsequently incorporate them in the fatigue model.

3.4 Material characterization tests

The tensile and compression properties of Hexply 8552/IM7 prepreg are lower for Elevated Temperature Wet (ETW) condition than for Room Temperature Dry (RTD) and Cold Temperature Dry (CTD) conditions [55]. Due to time constraint, it is impossible to test the coupons at various moisture levels and temperature conditions. Hence, for a conservative design, the coupons are only tested at the maximum ETW offshore environment possible for the Ampelmann system. The coupons are thereby conditioned at 90% Relative Humidity (R.H.) and 55°C for a period of 8 weeks. Tensile and compression tests of the coupons are performed at various moisture contents in order to determine the degradation of mechanical properties due to moisture and elevated temperature. As mentioned earlier in Section 2.9, the degradation of tensile and compression properties due to moisture are mainly dependant on the matrix. Due to time constraint in procuring the Hexply 8552/IM7 prepreg, the coupons are manufactured using Hexply 8552/AS4 prepreg. It is assumed that the degradation of material properties for Hexply 8552/IM7 and Hexply 8552/AS4 prepregs due to moisture ingress and elevated temperature are the same.

The details of the experimental procedure are shown in Appendix G. The test matrix used for the laminate level testing per preconditioning period is shown in Table 3.10.

Table 3.10: Laminate level test matrix per preconditioning period

Parameter	Unit	Test method	Number of specimens
% Moisture gain	-	ASTM D 5229/D 5229M	6
Compression modulus	GPa	ASTM D 6641/D 6641M	7
Compression strength	MPa	ASTM D 6641/D 6641M	7
Tensile modulus	GPa	ASTM D 3039/D 3039M	7
Tensile strength	MPa	ASTM D 3039/D 3039M	7

Standards for moisture ingression, tensile and compression testing suggest that a minimum of 5 coupons are required to estimate the moisture absorption, tensile and compression properties respectively. It is ideal to have more number of coupons for these tests so that the test data can be fit accurately to a probability distribution. Due to budget and time constraints, only 6 coupons are used for moisture ingression testing while 7 coupons are used for tension and compression per conditioning period at the cost of accuracy.

In order to obtain sufficient data for determining the effects of environment on the degradation of material properties, data pooling is subsequently used to calculate the material basis values. Due to material variability, it is important to choose design values which minimizes the probability of failure. A (99% probability with 95% confidence interval) and B basis (90% probability with 95% confidence interval) values are used to lower the probability of failure for critical structural components, and hence provide a framework for certification.

3.4.1 Moisture ingression test

As mentioned in Section 2.9, moisture ingression test is performed based on ASTM D 5229/D 5229M to determine the moisture absorption properties of the laminate. Six coupons are conditioned in an environment chamber for a period of 8 weeks. The weight gain of the coupons are measured every 7 days using a balance with an accuracy of 0.1 mg. The details of the experimental setup are shown in Appendix G. Table 3.11 shows the moisture ingression test matrix of the coupons.

Table 3.11: Moisture ingression test matrix

Parameter	Unit	Value
Length	mm	40
Width	mm	40
Thickness	mm	2.97
Reference time period	days	7
Number of tests	-	6x8=48

3.4.2 Tensile and compression test

The tensile and compressive properties of the coupons are determined by testing on the Zwick 250 kN machine. The coupons are preconditioned for 10 days, 25 days and 55 days and subsequently tested to determine the degradation of tensile and compressive properties with moisture content and elevated temperature. The detailed experimental setup for performing tension and compression test is given in Appendix G. Table 3.12 shows the tensile and compression test matrix of the coupons.

Table 3.12: Tension and compression test matrix

Parameter	Unit	Value	
		Tension	Compression
Length	mm	250	140
Width	mm	25	12
Thickness	mm	2.5	2.5
Preconditioning periods	days	0,10,25,55	0,10,25,55
Number of tests	-	7x4=28	7x4=28

The tensile strength and modulus of the coupons are given by,

$$\sigma_{tension} = \frac{F_{tension}}{A_{tension}} \tag{3.29}$$

$$E_{tension} = \frac{\Delta\sigma_{tension}}{\Delta\epsilon_{tension}} \tag{3.30}$$

The compressive strength and modulus of the coupons are given by,

$$\sigma_{compression} = \frac{F_{compression}}{A_{compression}} \tag{3.31}$$

$$E_{compression} = \frac{\Delta\sigma_{compression}}{\Delta\epsilon_{compression}} \tag{3.32}$$

3.4.3 Data pooling method

Due to time constraints, tensile and compression tests are performed only for specimens preconditioned at 90% R.H. and 55°C for 0, 10, 25 and 55 days. Subsequently, data pooling is used to obtain sufficient data to calculate the basis values to improve the understanding of the effect of moisture and elevated temperature on the material properties. The notation for the test conditions are shown in Table 3.13.

Table 3.13: Test condition notation

Notation	Preconditioning period in days
W1	0
W2	10
W3	25
W4	55

Test data are fit to Weibull distribution to obtain conservative basis values. The details of the two-parameter Weibull distribution are given in Appendix H. It is assumed that there are no variations in the fibre volume fractions of the specimens of the same batch. The methodology to perform data pooling is shown below :

- The data are collected for each test condition. Let x_{ij} corresponds to the jth data value for the ith test condition.
- The data for each test condition are fit to Weibull distribution and checked for outliers using the Maximum Normed Residual (MNR) test method shown in Appendix H. The shape and scale parameters of the Weibull distribution corresponding to the ith test condition are denoted by α_i and β_i respectively.
- A two-parameter Weibull goodness-of-fit test is performed for each test condition to check if the distribution adequately fits the data. The details of the goodness-of-fit test for Weibull distribution are shown in Appendix H.
- The A and B basis values of the Weibull distribution are calculated for each test condition using the method shown in Appendix H.
- Levene's test [40] is performed to check if the variability across test conditions are negligible before data pooling. Though the test assumes that the data are normally distributed, it is relatively insensitive to deviations from this assumption [40].
- The data are pooled by dividing the data set for each test condition by their corresponding β_i.
- A k-sample Anderson-Darling test is performed to check if the pooled data are from an identical population.
- The pooled data are fit to Weibull distribution with α_{pool} as the shape parameter and β_{pool} as the scale parameter.

- A two-parameter Weibull goodness-of-fit test is performed and the basis values are calculated for the pooled data. The A and B basis values of the pooled data are denoted by A_{pool} and B_{pool} respectively.
- The A and B basis values for each test condition is obtained by multiplying A_{pool} and B_{pool} with the corresponding β_i respectively.

3.5 Modified Kassapoglou's model

As Kassapoglou's model is based on residual strength, only static tensile and compressive strength data are pooled in order to incorporate them in the model. To explain a bit more about the modified Kassapoglou's model , it is assumed that the scale parameters of the static tension and compression properties of the laminate vary linearly with moisture content as shown in Figure 3.10.

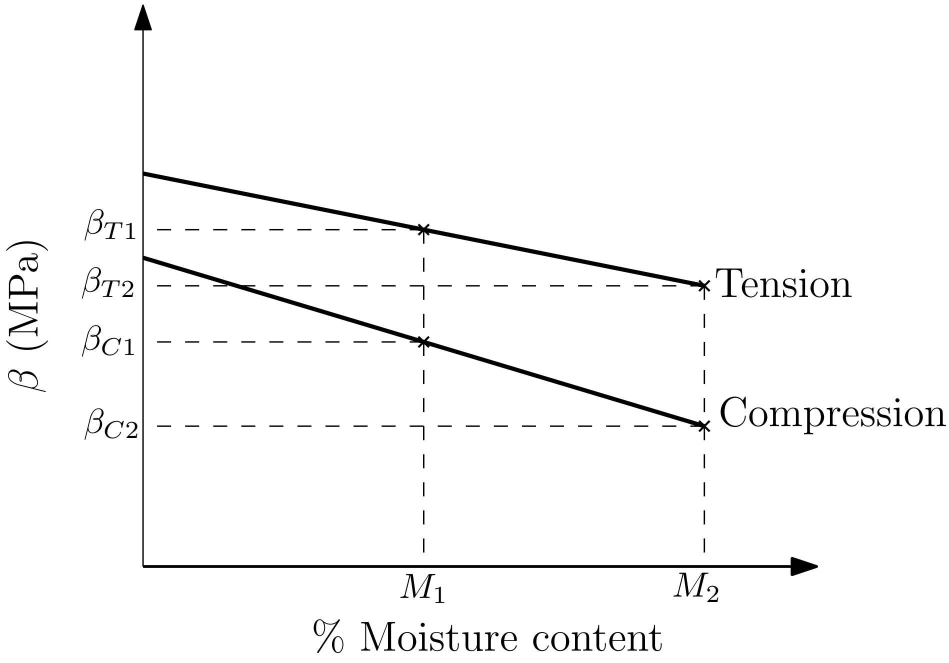

Figure 3.10: Variation of tensile and compressive strength with % moisture content (for illustrative purpose only)

After data pooling, it is assumed that the shape parameters for tension and compression tests are $\alpha_{pool,T}$ and $\alpha_{pool,C}$ respectively.

For Tension-Tension (T-T) fatigue,
The probability of failure at moisture contents M_1 and M_2 are given by,

$$p_{M1,T} = 1 - \mathrm{e}^{-(\sigma/\beta_{T1})^{\alpha_{pool,T}}} \tag{3.33}$$

$$p_{M2,T} = 1 - \mathrm{e}^{-(\sigma/\beta_{T2})^{\alpha_{pool,T}}} \tag{3.34}$$

Substituting Eq. (3.33) and Eq. (3.34) in Eq. (2.17), the stress that leads to failure after N cycles for moisture contents M_1 and M_2 are given by,

$$\sigma_{T,M1} = \frac{\beta_{T1}}{(N_{c,T})^{\frac{1}{\alpha_{pool,T}}}} \tag{3.35}$$

$$\sigma_{T,M2} = \frac{\beta_{T2}}{(N_{c,T})^{\frac{1}{\alpha_{pool,T}}}} \tag{3.36}$$

Similarly for Compression-Compression (C-C) fatigue,

$$\sigma_{C,M1} = \frac{\beta_{C1}}{(N_{c,C})^{\frac{1}{\alpha_{pool,C}}}} \tag{3.37}$$

$$\sigma_{C,M2} = \frac{\beta_{C2}}{(N_{c,C})^{\frac{1}{\alpha_{pool,C}}}} \tag{3.38}$$

The S-N curves of T-T and C-C fatigue in log-log scale for moisture contents M_1 and M_2 are shown in Figure 3.11.

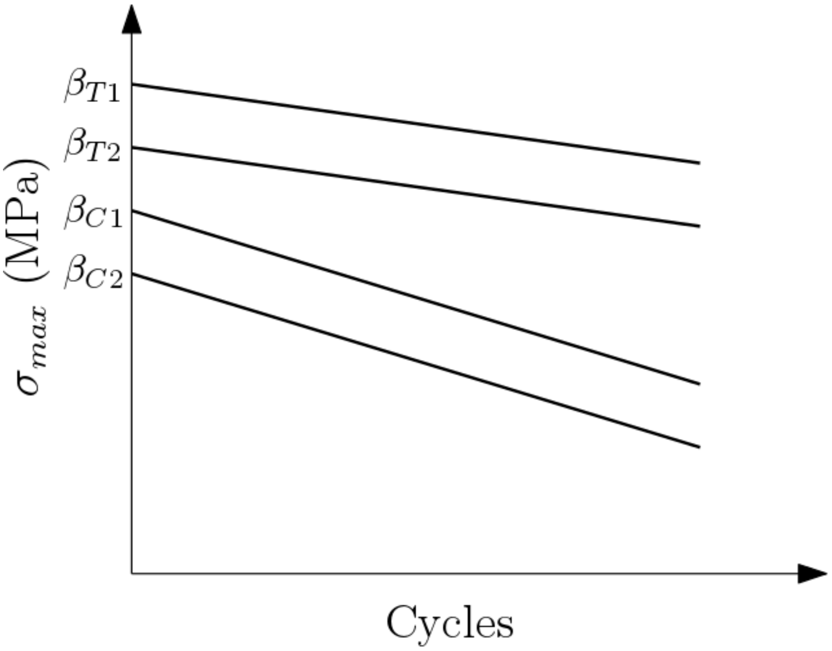

Figure 3.11: T-T and C-C fatigue curves for moisture contents M_1 and M_2 (for illustrative purpose only)

The same methodology can be used to plot the S-N curve for Tension-Compression (T-C) fatigue where the critical number of cycles to failure is calculated by Eq. (2.19). In this way, the effect of moisture and temperature are incorporated in the model to make it more robust in predicting the life of the structure.

This methodology plots a series of parallel S-N curves for different levels of moisture contents, shown in Figure 3.11. The advantage of using this approach is that, limited number of experiments are required to determine the S-N curves of a laminate for different environment conditions. Due to time constraints, the modified Kassapoglou's model is not validated with experimental results in the Master thesis.

3.6 Chapter Summary

This chapter summarizes the methodology adopted during the design and fatigue analysis phase of the Master thesis. In the preliminary design phase, an equivalent stiffness approach is adopted to replace the existing steel truss members by a FRP box beam of equivalent stiffness. The preliminary design of the composite T-boom is subsequently modelled in a FE environment using shell elements to compute the deflection and stresses. The detailed analysis phase explains the procedure to calculate the global deflection and natural frequency of the gangway. Finally in the fatigue analysis phase, the methodology to data pool and incorporate the effect of moisture and temperature in the Kassapoglou's model are explained.

Chapter 4

Results and Discussion

This chapter presents and discusses the results obtained from the design and fatigue analysis of the Telescoping boom (T-boom).

4.1 Preliminary design results

Based on the methodology discussed in Section 3.1, the layup and cross-section dimensions of members 1-6 of the composite T-boom are generated using the Matlab code shown in Appendix C. The dimensions of the chords and bracings for the preliminary design of the composite T-boom are shown in Table 4.1. The cross-section details of the chords and bracings are shown in Appendix D.

Table 4.1: Dimensions of the chords and bracings of the composite T-boom

Parameter	Unit	1	2	3	4	5	6
a_{box}	mm	150	150	150	150	150	150
b_{box}	mm	50	150	50	50	50	50
n_{plies}	-	40	67	40	40	40	40
t_{box}	mm	6.1	10.21	6.1	6.1	6.1	6.1
L_{box}	mm	13,305	13,305	600	849	570	825
A_{box}	$\times 10^3$ mm^2	2.29	5.71	2.29	2.29	2.29	2.29
$I_{box,x1}$	$\times 10^6$ mm^4	5.82	18.70	5.82	5.82	5.82	5.82
$I_{box,y1}$	$\times 10^6$ mm^4	5.82	18.70	5.82	5.82	5.82	5.82

The layup of the chords and bracings for the design options A and B are shown in Table 4.2 and Table 4.3 respectively.

Table 4.2: Layup of the chords and bracings for the design option A

Part	Option A layup
Member 1	$[0_3/(45/-45)_3/0_3/(45/-45)_2/90/45/-45/90]s$
Member 2	$[0_3/(45/-45)_3/0_3/(45/-45)_3/0_3/(45/-45)_3/0/90_2/45/-45/90/\bar{90}]s$
Member 3	$[0_3/(45/-45)_3/0_3/(45/-45)_2/90/45/-45/90]s$
Member 4	$[0_3/(45/-45)_3/0_3/(45/-45)_2/90/45/-45/90]s$
Member 5	$[0_3/(45/-45)_3/0_3/(45/-45)_2/90/45/-45/90]s$
Member 6	$[0_3/(45/-45)_3/0_3/(45/-45)_2/90/45/-45/90]s$

Table 4.3: Layup of the chords and bracings for the design option B

Part	Option B layup
Member 1	$[0_3/(45/-45)_2/0_3/(45/-45)/0_2/45/-45/90/45/-45/90]s$
Member 2	$[0_3/(45/-45)_3/0_3/(45/-45)_3/0_3/(45/-45)_2/0_3/90_2/45/-45/90/\bar{90}]s$
Member 3	$[0_3/(45/-45)_2/0_3/(45/-45)/0_2/45/-45/90/45/-45/90]s$
Member 4	$[0_3/(45/-45)_2/0_3/(45/-45)/0_2/45/-45/90/45/-45/90]s$
Member 5	$[0_3/(45/-45)_2/0_3/(45/-45)/0_2/45/-45/90/45/-45/90]s$
Member 6	$[0_3/(45/-45)_2/0_3/(45/-45)/0_2/45/-45/90/45/-45/90]s$

The % number of 0° plies in member 2 for the design options A and B are rounded off to the nearest even integers to preserve the symmetry and 10 % design rule. The ABD matrix of the flanges and webs are calculated by the Matlab code shown in Appendix C to estimate the E_{1m} and E_{1b} using Eq. (2.3) and Eq. (2.5) respectively. The E_{1m} and E_{1b} of the chords and bracings for the design options are shown in Table 4.4.

Table 4.4: Membrane and bending modulus of the chords and bracings

Part	E_{1m} (GPa)		E_{1b} (GPa)	
	A	B	A	B
Member 1	68.2	82.3	91.1	103.4
Member 2	68.1	76.52	81.25	82.57
Member 3	68.2	82.3	91.1	103.4
Member 4	68.2	82.3	91.1	103.4
Member 5	68.2	82.3	91.1	103.4
Member 6	68.2	82.3	91.1	103.4

Due to low modulus of the composite laminate, shown in Table 4.4, the cross-section dimensions of the members are increased in order to satisfy Eq. (3.1), Eq. (3.2) and Eq. (3.3) for the chords, and Eq. (3.4), Eq. (3.5) and Eq. (3.6) for the bracings (see Table 4.1). It can be inferred from Eq. (F.2) that the wind load is proportional to the area exposed to the wind. As a result, the wind load increases in proportion to the increase in the cross-section dimensions of the members and is given by Eq. (4.1).

$$F_{wind} \propto A \propto a_{box} \times L_{box} \tag{4.1}$$

where A is the area of the truss member exposed to the wind (mm^2).

Due to an increase in the wind load, the shear forces and bending moments at the T-boom section increases, thereby increasing the stress and deflection of the truss members.

4.1.1 Axial stiffness estimation

After evaluating the modulus, the stiffness of the bracings and chords of the composite T-boom are estimated using Eq. (2.6) and Eq. (2.7)-Eq. (2.8) as shown in Appendix D. Table 4.5 depicts the comparison of axial stiffness of the chords and bracings between the composite and existing T-boom design.

Table 4.5: Axial stiffness comparison of the members of the composite and steel T-boom

Part	$E_{1m}A_{box}/EA_{steel}$	
	A	B
Member 1	1.01	1.22
Member 2	0.86	0.98
Member 3	1.01	1.22
Member 4	1.29	1.56
Member 5	1.57	1.89
Member 6	1.57	1.89

As seen in Table 4.5, the axial stiffness of member 2 of the composite T-boom is smaller than the existing steel design. Since the axial stiffness of the members of the composite T-boom are greater than that of the existing steel design except for member 2, it is concluded that the axial stiffness requirements, Eq. (3.1) and Eq. (3.4), are satisfied. As member 2 is primarily in bending, it is assumed that violating the axial stiffness requirement is not as critical as violating the bending stiffness requirement. Hence, the design options considered for member 2 are not omitted.

4.1.2 Bending stiffness estimation

The bending stiffness of the chords of the composite T-boom in the x_1 and y_1 axes are compared with the corresponding bending stiffness values of the steel design. Table 4.6 depicts the comparison of bending stiffness of the chords and bracings in the x_1 and y_1 axis between the composite and existing T-boom design.

Table 4.6: Bending stiffness comparison of the chords of the composite and steel T-boom in x_1 and y_1 axis

Part	$E_{1b}I_{box,x1}/EI_{steel,x1}$		$E_{1b}I_{box,y1}/EI_{steel,y1}$	
	A	B	A	B
Member 1	9.64	10.95	1.56	1.77
Member 2	2.91	2.94	9.44	9.57

Since the bending stiffness of the chords of the composite T-boom are greater than the existing steel design, it is concluded that the bending stiffness requirements, Eq. (3.2) and Eq. (3.3), are satisfied. Since member 2 satisfies the more critical bending stiffness requirements, the design options considered for member 2 are not omitted in the preliminary design phase.

It can be inferred from Table 4.6 that, in terms of bending stiffness, the weakest axes for members 1 and 2 are respectively y_1 and x_1. It is more critical to satisfy the bending stiffness requirement in the weakest axis. This, when coupled with the axial stiffness requirement, increases the cross-section dimensions of the members to such an extent that, in their strongest axis, their bending stiffness is much higher than the corresponding bending stiffness of the steel members, shown in Table 4.6.

4.1.3 Buckling modulus estimation

For the bracings, the buckling modulus are compared for the composite and steel design in the weakest axis or y_1 axis. Table 4.7 shows the comparison of buckling modulus of the chords and bracings in the weakest axis between the composite and existing T-boom design.

Table 4.7: Buckling modulus comparison of the bracings between the composite and steel T-boom in the weakest axis

Part	$E_{1m}I_{box}/EI_{steel,beam}$	
	A	B
Member 3	1.17	1.41
Member 4	2.43	2.94
Member 5	2.71	3.27
Member 6	2.71	3.27

Since the buckling modulus of the bracings of the composite T-boom are greater than the existing steel design, it is concluded that the buckling modulus requirement, Eq. (3.4), is satisfied.

Based on the results discussed in Table 4.5, Table 4.6 and Table 4.7, it can be concluded that all the stiffness requirements are satisfied by the members of composite T-boom.

4.1.4 Mass estimation

The preliminary design of the composite T-boom is subsequently modelled in Catia and the drawing of the composite T-boom is shown in Appendix D. The Catia model is subsequently used for Finite Element (FE) analysis to determine the structural response of the composite T-boom subjected to design loads.

The mass of the preliminary design of the composite T-boom is estimated using Catia, and, is compared with the existing steel design. Table 4.8 compares the mass of the composite and existing steel T-boom without considering joints like welds and bolts, and other secondary attachments.

Table 4.8: Mass comparison of the composite and steel T-boom

Composite T-boom mass (kg)	Steel T-boom mass (kg)	% weight reduction
520	950	45.3

The current weight reduction of the composite T-boom does not take into account the effect of joints and fatigue life on the structure. It is expected that the weight reduction will be lower if the effect of joints are considered in the design because joints may result in stress raisers, and, can act as a hotspot for failure. Hence, additional patchwork may be required to reduce the stresses at the joints thereby increasing the weight of the structure. Also, cutouts have to be provided on the structural members in order to assemble the secondary attachments onto it thereby requiring additional reinforcements to strengthen the structure. This will in turn lead to an overall increase in the weight of the structure. Despite all this, the preliminary estimate of weight reduction is quite promising for the composite T-boom, and, has to be researched further before making concrete conclusions.

4.2 FE analysis results

As discussed in Section 3.2, since it is computationally expensive to mesh the entire T-boom, only a section of 5420 mm long, shown in Figure 3.5, is used for the FE analysis. Also, the structural response of the composite T-boom section are determined only for the worst load cases: Emergency Operation- 3 People Transfer (EO-3PT), Emergency Operation- Extra Length + Cargo (EO-ELC) and Stowed Condition (SC). The shear forces and bending moments, shown from Table 3.3 to Table 3.8, are input to the FE model while roller support constraints are imposed at the location of the rollers. The ends of the bottom chords closer to the Main Boom (MB)/T-boom interface are constrained in the telscopping direction, y axis, to restrict the motion due to the telescopping force. Finally, the bottom chords near the roller supports are constrained in the luffing direction, x axis, in order to restrict the motion due to the wind loads. Figure 4.1 and Figure 4.2 depict the constraints applied to the FE model.

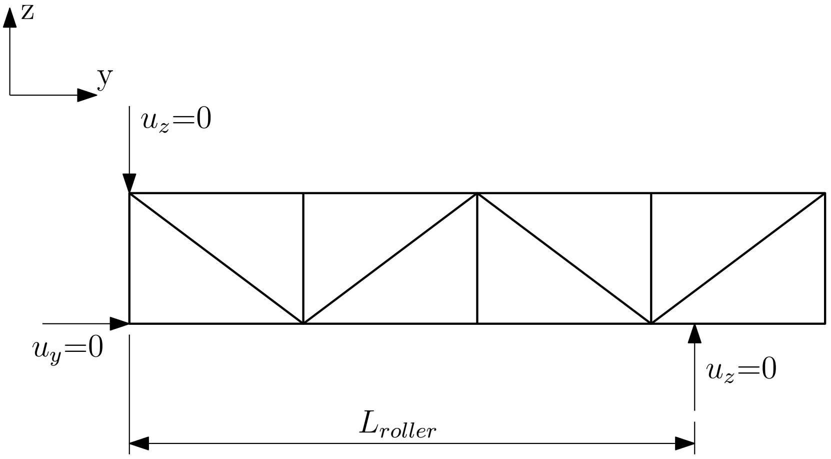

Figure 4.1: Boundary conditions for the FE model in the y and z axis

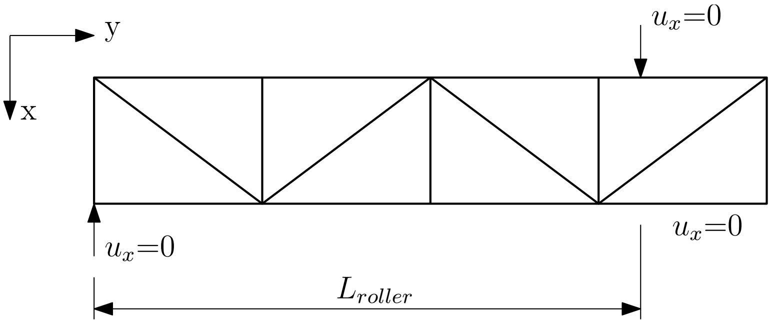
y
x
u_x=0
u_x=0
u_x=0
L_{roller}

Figure 4.2: Boundary conditions for the FE model in the x axis

4.2.1 SC results

The deflection of the FE model for the design options A and B during SC are shown in Figure 4.3a and Figure 4.3b respectively.

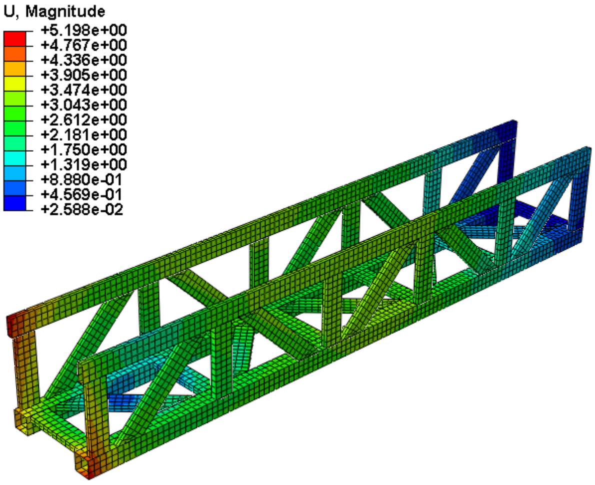
U, Magnitude
+5.198e+00
+4.767e+00
+4.336e+00
+3.905e+00
+3.474e+00
+3.043e+00
+2.612e+00
+2.181e+00
+1.750e+00
+1.319e+00
+8.880e-01
+4.569e-01
+2.588e-02

(a) Design option A

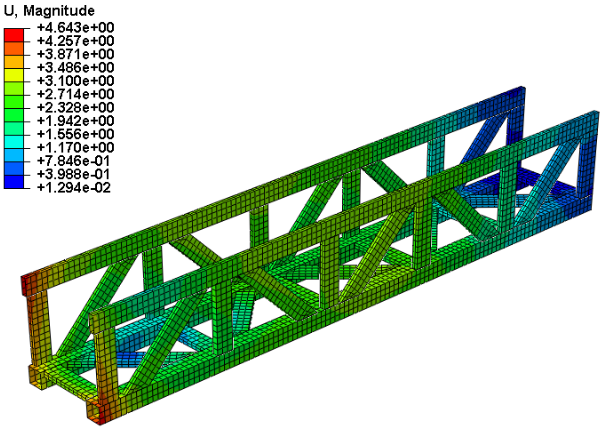
U, Magnitude
+4.643e+00
+4.257e+00
+3.871e+00
+3.486e+00
+3.100e+00
+2.714e+00
+2.328e+00
+1.942e+00
+1.556e+00
+1.170e+00
+7.846e-01
+3.988e-01
+1.294e-02

(b) Design option B

Figure 4.3: Deflection of the T-boom section during SC

The maximum local deflection of the truss members for the design options A and B are 5.198 and 4.643 mm respectively. Since the maximum local deflection of the truss members is less than $L/100$ for both the design options, the deflection requirement mentioned in Section 2.5 is satisfied for the SC.

Figure 4.4a and Figure 4.4b depict the Tsai-Wu failure criterion value for the design options A and B during SC.

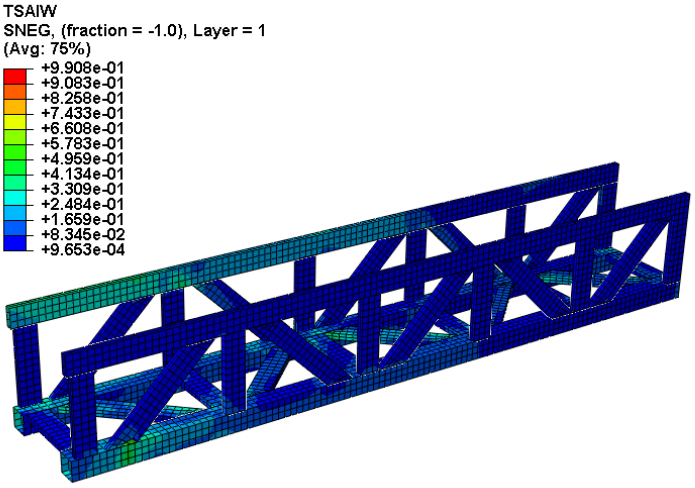

(a) Design option A

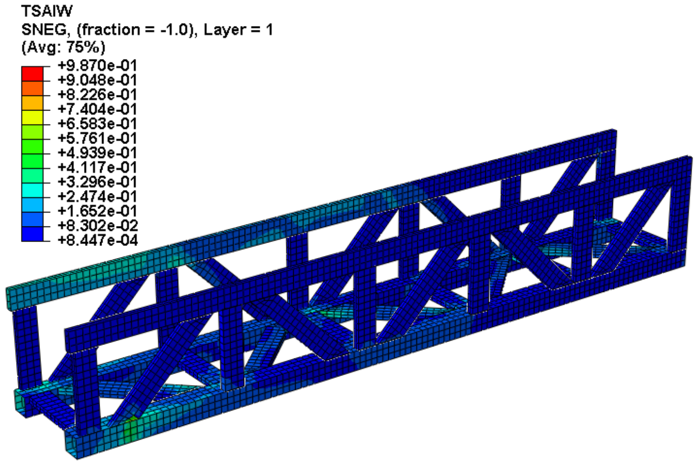

(b) Design option B

Figure 4.4: Tsai-Wu value of the T-boom section during SC

The margin of safety for the design options A and B during SC are given by Eq. (4.2) and Eq. (4.3) respectively.

for the design option A,

$$Margin\ of\ safety = \left(\frac{1}{0.9908} - 1\right) \cdot 100 = 0.93\ \% \tag{4.2}$$

for the design option B,

$$Margin\ of\ safety = \left(\frac{1}{0.987} - 1\right) \cdot 100 = 1.32\ \% \tag{4.3}$$

Since the margin of safety is greater than 0 for both the design options, it can be concluded that for the load case, SC , the structure is safe from material failure.

4.2.2 EO-3PT results

The deflection of the FE model for the design options A and B during EO-3PT are shown in Figure 4.5a and Figure 4.5b respectively.

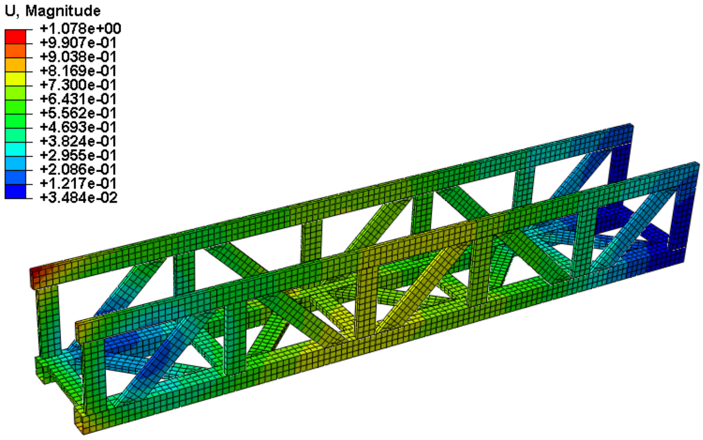
U, Magnitude
+1.078e+00
+9.907e-01
+9.038e-01
+8.169e-01
+7.300e-01
+6.431e-01
+5.562e-01
+4.693e-01
+3.824e-01
+2.955e-01
+2.086e-01
+1.217e-01
+3.484e-02

(a) Design option A

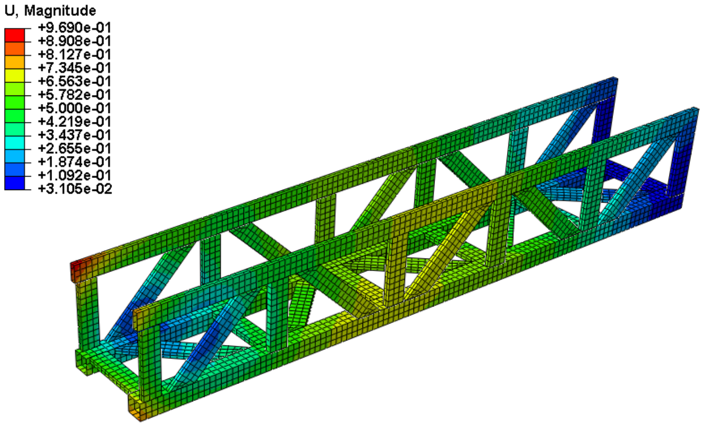
U, Magnitude
+9.690e-01
+8.908e-01
+8.127e-01
+7.345e-01
+6.563e-01
+5.782e-01
+5.000e-01
+4.219e-01
+3.437e-01
+2.655e-01
+1.874e-01
+1.092e-01
+3.105e-02

(b) Design option B

Figure 4.5: Deflection of the T-boom section during EO-3PT

The maximum local deflection of the truss members for the design options A and B are 1.08 and 0.97 mm respectively. Since the maximum local deflection of the truss members of both the design options are less than the maximum allowable deflection, it can be concluded that the deflection requirement mentioned in Section 2.5 is satisfied for both the design options during EO-3PT.

Figure 4.6a and Figure 4.6b depict the Tsai-Wu failure criterion value for the design options A and B during EO-3PT.

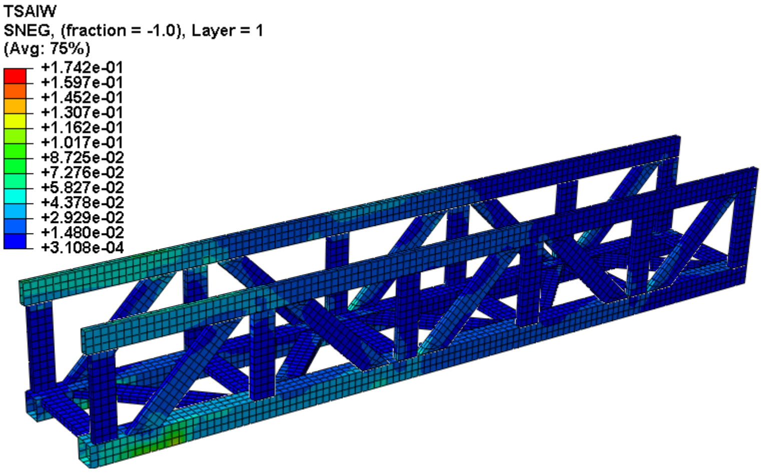
TSAIW
SNEG, (fraction = -1.0), Layer = 1
(Avg: 75%)
+1.742e-01
+1.597e-01
+1.452e-01
+1.307e-01
+1.162e-01
+1.017e-01
+8.725e-02
+7.276e-02
+5.827e-02
+4.378e-02
+2.929e-02
+1.480e-02
+3.108e-04

(a) Design option A

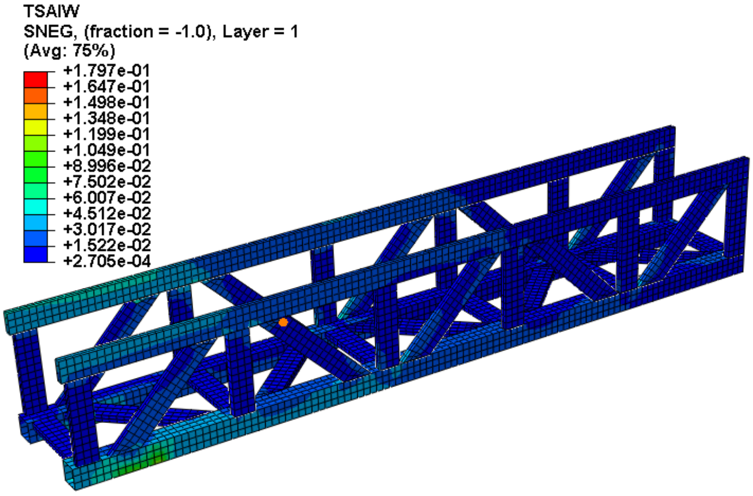
TSAIW
SNEG, (fraction = -1.0), Layer = 1
(Avg: 75%)
+1.797e-01
+1.647e-01
+1.498e-01
+1.348e-01
+1.199e-01
+1.049e-01
+8.996e-02
+7.502e-02
+6.007e-02
+4.512e-02
+3.017e-02
+1.522e-02
+2.705e-04

(b) Design option B

Figure 4.6: Tsai-Wu value of the T-boom section during EO-3PT

The margin of safety for the design options A and B during EO-3PT are given by Eq. (4.4) and Eq. (4.5) respectively.

for the design option A,

$$Margin\ of\ safety = \left(\frac{1}{0.1742} - 1\right) \cdot 100 = 474.1\ \% \tag{4.4}$$

for the design option B,

$$Margin\ of\ safety = \left(\frac{1}{0.1797} - 1\right) \cdot 100 = 456.48\ \% \tag{4.5}$$

Since the margin of safety is greater than 0 for both the design options, it can be concluded that for the load case, EO-3PT , the structure is safe from material failure.

4.2.3 EO-ELC results

The deflection of the FE model for the design options A and B during EO-ELC are shown in Figure 4.7a and Figure 4.7b respectively.

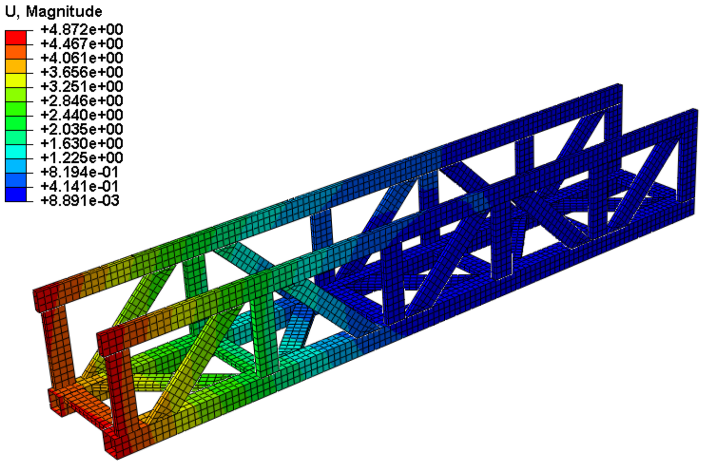
U, Magnitude
+4.872e+00
+4.467e+00
+4.061e+00
+3.656e+00
+3.251e+00
+2.846e+00
+2.440e+00
+2.035e+00
+1.630e+00
+1.225e+00
+8.194e-01
+4.141e-01
+8.891e-03

(a) Design option A

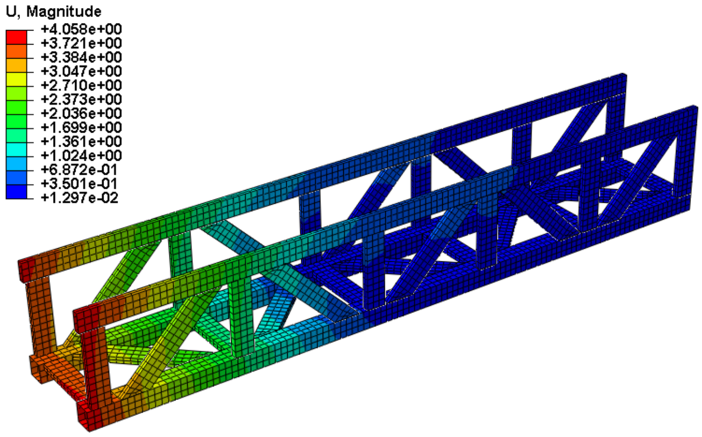
U, Magnitude
+4.058e+00
+3.721e+00
+3.384e+00
+3.047e+00
+2.710e+00
+2.373e+00
+2.036e+00
+1.699e+00
+1.361e+00
+1.024e+00
+6.872e-01
+3.501e-01
+1.297e-02

(b) Design option B

Figure 4.7: Deflection of the T-boom section during EO-ELC

The maximum local deflection of the truss members for the design options A and B are 4.872 and 4.06 mm respectively. Since the maximum local deflection of the truss members of both the design options are less than the maximum allowable deflection, it can be concluded that the deflection requirement mentioned in Section 2.5 is satisfied for both the design options during EO-ELC.

Figure 4.8a and Figure 4.8b depict the Tsai-Wu failure criterion value for the design options A and B during EO-3PT.

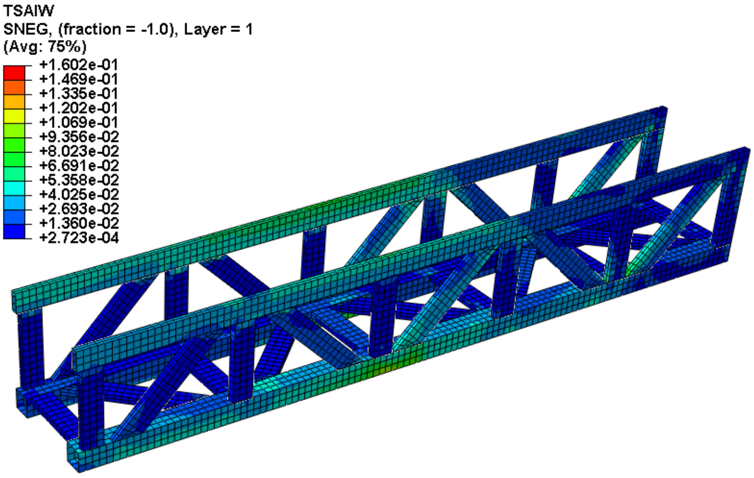

(a) Design option A

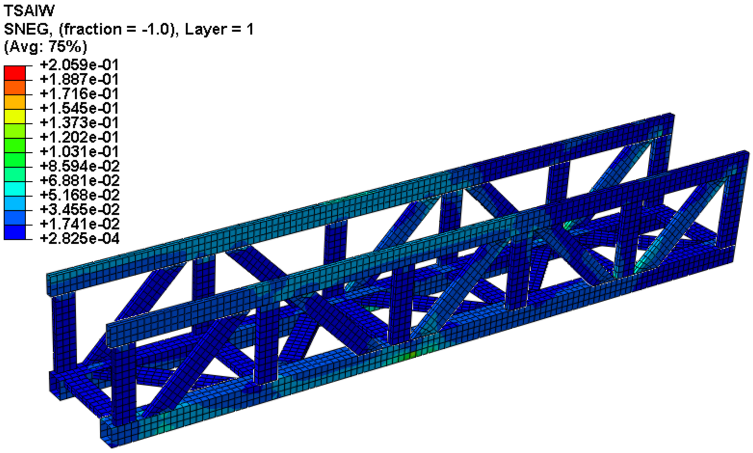

(b) Design option B

Figure 4.8: Tsai-Wu value of the T-boom section during EO-ELC

The margin of safety for the design options A and B during EO-ELC are given by Eq. (4.6) and Eq. (4.7) respectively.

for the design option A,

$$Margin\ of\ safety = \left(\frac{1}{0.1602} - 1\right) \cdot 100 = 524.22\ \% \tag{4.6}$$

for the design option B,

$$Margin\ of\ safety = \left(\frac{1}{0.206} - 1\right) \cdot 100 = 385.44\ \% \tag{4.7}$$

Since the margin of safety is greater than 0 for both the design options, it can be concluded that for the load case, EO-ELC , the structure is safe from material failure.

The summary of the FE results for the worst load cases are shown in Table 4.9.

Table 4.9: FE results summary for the worst load cases

Load case	Margin of safety (%)		Maximum displacement (mm)	
	A	B	A	B
SC	0.9	1.3	5.2	4.6
EO-3PT	474.1	456.5	1.1	1.0
EO-ELC	524.2	385.4	4.9	4.1

The composite T-boom has a lower margin of safety and maximum deflection for the SC load case. Hence, it can be concluded that SC is the worst load case scenario encountered by the composite T-boom. Since, design option B has a higher margin of safety and a lower maximum deflection than design option A for the SC load case, it is selected as the final design option for the composite T-boom. The advantages of going for design option B are the following:

(a) It has a higher margin of safety for the worst load case. This implies that the structure can be optimized further, yielding higher weight reduction.

(b) It is stiffer thereby improving the natural frequency of the composite T-boom.

Another interesting observation is that, the margin of safety is higher for the design option A for EO-3PT and EO-ELC load cases. This might be due to the fact that shear loads are more dominant than bending loads on the structure for these load scenarios. Since design option A has more number of +45/-45 plies than design option B, it thereby has a higher margin of safety. The higher margin of safety for the design option B during SC load case might be due to the fact that the bending loads are more dominant than the shear loads. Since, design option B has more number of 0 plies, it has a higher margin of safety for the SC load case.

The downside of the current FE model is that analysis is performed only at the T-boom section close to the rollers. Since the analysis is localized, it is impossible to study the global buckling of the T-boom, and, global deflection and natural frequency of the gangway. This problem was solved by estimating these parameters analytically at the expense of accuracy. Also, the effect of stress concentrations at the box beam corners were not considered in the analysis. These regions are a hotspot for failure as resin pockets might be created at the flange/web intersection. The effect of joints will also have a significance influence in the FE results, as they might act as stress raisers. The accuracy of the FE predictions can be improved by accounting the effect of joints and resin pockets, and, subsequently validating the results by testing.

4.2.4 Local buckling

The local buckling of the design option B of the composite T-boom is checked for the worst load case, SC. Figure 4.9 shows the local buckling analysis for the design option B during SC.

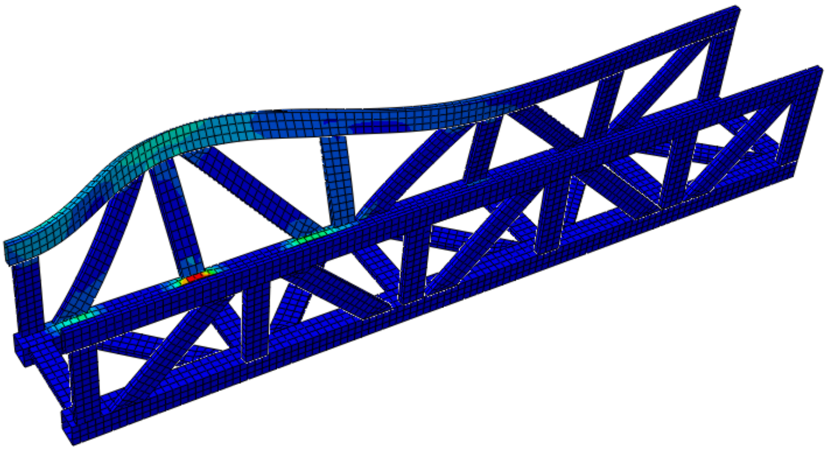

Figure 4.9: Local buckling analysis for the design option A during SC

Eigenvalue is used to predict the theoretical buckling load of an elastic structure. The eigenvalue of the composite T-boom for the SC load case is 3.70. As the eigenvalue of the structure is greater than 1 , it can be concluded that there is no local buckling during the SC load case. Also, since the vertical truss members, shown in Figure 4.9, are in tension, they are not expected to buckle in the first mode.

The downside of this analysis is that the local buckling is evaluated only at the critical regions of the T-boom. As a result, it is impossible to evaluate the local mode shapes of the entire T-boom. This problem can be solved by analysing the entire T-boom in ABAQUS at the expense of computational and modelling effort.

4.3 Detailed analysis

In this section, the parameters that are estimated are the following:

(a) Global deflection of the gangway retrofitted with the composite T-boom.

(b) Natural frequency of the gangway in bending retrofitted with the composite T-boom.

(c) Global buckling of the T-boom

4.3.1 Global deflection of the gangway

The global deflection of the gangway are estimated in the horizontal and vertical direction for a unit tip load and compared against the existing gangway design.

The parameters used to determine the horizontal deflection of the gangway are shown in Table 4.10.

Table 4.10: Parameters for the horizontal deflection determination

Parameter	Unit	MB	Steel T-boom	Composite T-boom
Load, F	N	1	1	1
Length, L	m	12.3	9	9
EI_z	N × mm^2	2.5 × 10^{14}	2.04 × 10^{14}	2.33 × 10^{14}

The detailed calculation of the bending stiffness of the steel and composite T-boom are shown in Appendix A and D respectively. Substituting these values in Eq. (3.23), Eq. (3.24) and Eq. (3.25), the horizontal deflection under unit load of the gangway retrofitted with the composite T-boom is calculated and is given by Eq. (4.8).

$$w_{gangway,x} = 0.015\ mm \tag{4.8}$$

The corresponding value for the existing gangway is 0.018 mm. Table 4.11 compares the horizontal deflection of the gangway retrofitted with the composite T-boom and steel T-boom.

Table 4.11: Horizontal deflection comparison of the gangway

with Composite T-boom	with Steel T-boom	% reduction
0.015	0.016	6.25

The gangway retrofitted with the composite T-boom is stiffer in the horizontal direction than the existing gangway and the horizontal deflection is reduced by 6.25 %. Since, the existing gangway satisfies the horizontal deflection requirement, it can be concluded the gangway retrofitted with the composite T-boom also satisfies the same.

The parameters used to determine the vertical deflection of the gangway are shown in Table 4.12.

Table 4.12: Parameters for the vertical deflection determination

Parameter	Unit	MB	Steel T-boom	Composite T-boom
Load, F	N	1	1	1
Length, L	m	12.3	9	9
EI_x	N × mm^2	3.38 × 10^{14}	1.57 × 10^{14}	2.13 × 10^{14}
Mass	kg	2181	950	520
Weight per unit length, q	N/mm	1.74	1.04	0.57

Substituting these values in Eq. (3.18) to Eq. (3.22), the vertical deflection under unit load of the gangway retrofitted with the composite T-boom is calculated and is given by Eq. (4.9).

$$w_{gangway,z} = 63.60\ mm \tag{4.9}$$

The corresponding value for the existing gangway is 130.42 mm. Table 4.13 compares the horizontal deflection of the gangway retrofitted with the composite T-boom and steel T-boom.

Table 4.13: Vertical deflection comparison of the gangway

with Composite T-boom	with Steel T-boom	% reduction
63.60	77.59	18

The gangway retrofitted with the composite T-boom is stiffer in the vertical direction than the existing gangway and the vertical deflection is reduced by 18%. Since, the existing gangway satisfies the vertical deflection requirement, it can be concluded the gangway retrofitted with the composite T-boom also satisfies the same.

Since the gangway retrofitted with composite T-boom is stiffer than the existing gangway, the horizontal and vertical deflection of the former is smaller than the latter. Hence, the design requirement for deflection is satisfied for the composite T-boom in both directions. The advantage of using a composite T-boom is more visible in the vertical deflection of the gangway because of higher margin of reduction due to lower self-weight and higher stiffness.

4.3.2 Natural frequency of the gangway

The natural frequency of the gangway retrofitted with the composite T-boom in bending are estimated in the horizontal and vertical direction for a $SWL = 0$ kg.

The parameters used to determine the natural frequency of the gangway in the horizontal direction and vertical direction are given in Table 4.11 and Table 4.13 respectively. Table 4.14 compares the natural frequencies of the gangway retrofitted with the composite T-boom with the corresponding vibration requirements set forth by Ampelmann.

Table 4.14: Natural frequency comparison of the gangway

Parameter	with Composite T-boom	with Steel T-boom	% increase
f_x	1.77	1.33	33.1
f_z	1.90	1.33	42.86

As the natural frequencies of the gangway retrofitted with the composite T-boom in bending are greater than the minimum fundamental frequencies required by Ampelmann, described in Section 2.5, it can be concluded that the structure satisfies the vibration requirements. It should be noted that, the natural frequencies for the gangway are estimated only for the bending modes. Other modes like torsion mode and mixed torsion-bending mode are possible for the gangway, which can be estimated by FE analysis of the full scale model or by experimental investigation. Due to time constraints, the effect of other modes on the structure are not investigated in this thesis.

As mentioned earlier, the bending stiffness estimate of the T-boom is conservative as it does not account the contribution of members 3-6. Also, the effect of MB/T-boom interface is neglected in the deflection and natural frequency estimation of the gangway. If the interface is taken into account in the analysis, the schematic beam model of gangway will look like Figure 4.10.

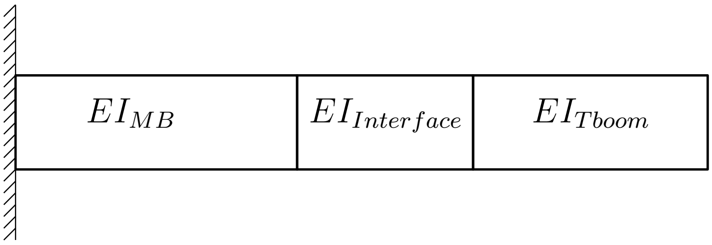

Figure 4.10: Schematic beam model of the gangway including the effect of MB/T-boom interface

Although, it is quite complex to analytically estimate the bending stiffness of the MB/T-boom interface, it can be inferred that the overall length average bending stiffness of the gangway increases. As a result, the global deflection of the gangway decreases, and, the natural frequency of the gangway increases. Hence, it can be concluded that the preliminary estimate of the natural frequency and global deflection of the gangway are conservative. The accuracy of these predictions can be improved by analysing the whole gangway in a FE environment or testing the gangway.

4.3.3 Global buckling of the composite T-boom

As discussed in Section 3.3, the global buckling of the composite T-boom is estimated by modelling it as a beam of the same length and bending stiffness. The parameters to estimate the column buckling load are shown in Table 4.15.

Table 4.15: Column buckling load of the T-boom

Parameter	Unit	Value
$EI_{Tboom,x}$	N × mm^2	2.13 × 10^{14}
$EI_{Tboom,z}$	N × mm^2	2.33 × 10^{14}
EI_{Tboom}	N × mm^2	2.13 × 10^{14}
L_{Tboom}	mm	13100

Substituting these values in Eq. (3.28), the column buckling load of the composite T-boom is calculated and given by 1.23×10^7 N.

The maximum compressive load on the T-boom is due to the free-float telescoping force, which is 10 kN. As the column buckling load is larger than the maximum compressive load possible for the composite T-boom, it can be concluded that the T-boom will not fail by column bucking during its operation.

Since it is quite complex to model the roller support constraints of the T-boom, it is assumed that the T-boom is simply supported as it yields conservative results. It is difficult to comment about the predictive accuracy of the analysis due to the conservative boundary conditions and estimate of the bending stiffness. However, it can be concluded that the actual global buckling load will be higher than the estimated load, and, the T-boom will not undergo global buckling during its operation.

4.4 Material characterization test results

The results of the material characterization tests are discussed for the laminate whose layup is based on design option B, and, given by $[0_3, (45/-45)_2, 90_2]s$.

4.4.1 Moisture ingression test results

The mass of the coupons for the moisture ingression tests were measured every 7 days for a period of 8 weeks, and, the M_{gain} was calculated using Eq. (2.22). Table 4.16 shows the average mass and M_{gain} of the coupons for the 8 week period.

Table 4.16: Moisture ingression test results

Week	W_i (mg)	M_{gain} (%)
0	7351.6	0
1	7373.8	0.30
2	7383.5	0.43
3	7391.5	0.54
4	7398.0	0.63
5	7403.9	0.71
6	7408.5	0.77
7	7412.6	0.83
8	7414.8	0.86

Figure 4.11 shows the moisture absorption curve for Hexply 8552/AS4 laminate conditioned at 90% Relative Humidity (R.H.) and 55°C.

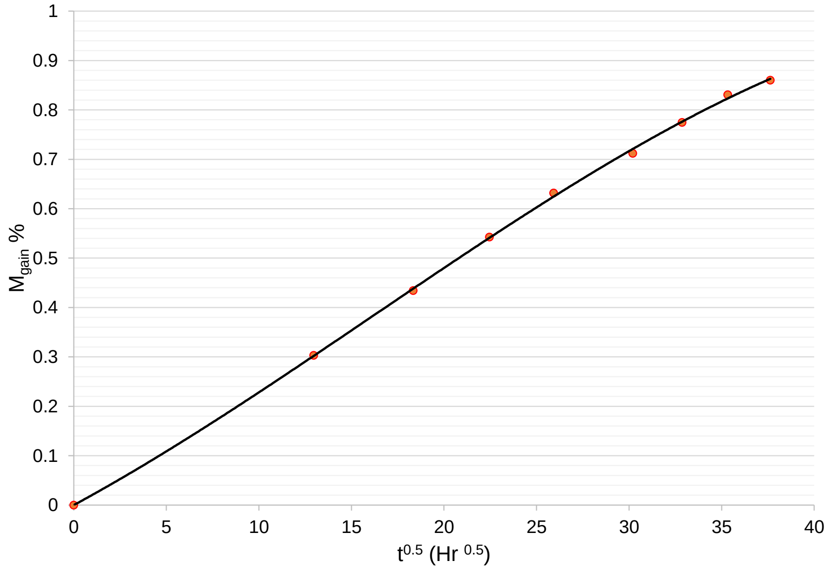

Figure 4.11: Moisture absorption curve for Hexply 8552/AS4 laminate

The initial linear portion of the moisture absorption curve indicates a Fickian diffusion pattern which validates the assumption made in Section 2.9. Studies carried out by Akbar and Zhang [32], and, Dao, et al. [36] indicate that the moisture absorption curve subsequently concaves to the time axis until M_m is reached. Since M_{gain} of the laminate changes by more than 0.01 % within the reference time period, it can be concluded that the coupons are not saturated after conditioning them for 8 weeks. Since M_m is unknown, it is impossible to calculate D for the laminate using Eq. (2.23). The coupons are allowed to condition further in the climate chamber till they are saturated, and, the results are not discussed in the report due to time constraints.

It is impossible to determine the equivalent number of years an Ampelmann system is expected to work offshore for the given moisture ingression period and environment condition due to the following reasons:

(a) An Ampelmann system works all around the globe in a diverse environment, and, as a result it is difficult to track the operating conditions experienced by it.

(b) As mentioned in Section 2.3, the Ampelmann system is in the settled position during majority of its lifetime. During the settled position, salt water might get sprayed on the composite T-boom due to harsh sea states, and, result in the degradation of the structure. Due to variability in the sea conditions, it is quite difficult to predict the moisture absorption pattern of the entire structure or local parts.

Hence, the strength and fatigue analysis can done for the worst case scenario where the entire T-boom is completely saturated. Since the laminate is not completely saturated for the given moisture ingression period, analysis is done at the maximum moisture content of 0.86% for the 8^{th} week.

4.4.2 Compression test results

Table 4.17 shows the shape and scale parameters of the compressive strength of the Hexply 8552/AS4 laminate preconditioned for 0, 10, 25 and 55 days (refer Table 3.13 for the notations).

Table 4.17: Static compressive strength results of Hexply 8552/AS4 laminate

Parameter	Unit	W1	W2	W3	W4
Shape parameter	-	47.5	31.3	33.2	49.8
Scale parameter	MPa	532	512	489	481
A basis	MPa	423	362	353	386
B basis	MPa	472	428	413	429

4.4.3 Tension test results

Table 4.18 shows the shape and scale parameters of the tensile strength of the Hexply 8552/AS4 laminate preconditioned for 0, 10, 25 and 55 days.

Table 4.18: Static tensile strength results of Hexply 8552/AS4 laminate

Parameter	Unit	W1	W2	W3	W4
Shape parameter	-	51.5	30.1	22.7	50
Scale parameter	MPa	1002	975	952	942
A basis	MPa	741	644	589	758
B basis	MPa	856	786	743	842

Kassapoglou [56] observes that the shape parameter of a two-parameter Weibull distribution is inversely proportional to the scatter. The increase in the scatter at W2 as compared to W1 for tensile and compressive strength might be because of the presence of a number of flaws [56] caused by moisture and elevated temperature. The subsequent decrease in the scatter at W4 might be because a flaw created during moisture ingress is exacerbated during static loading. This flaw might have overwhelmed the presence of other smaller inherent flaws in the structure, and, consequently driven the failure of the structure. Since the number of coupons tested per preconditioning period is small, it is difficult to comment about the accuracy of the predictions. But, it is possible to improve the accuracy by testing more coupons per preconditioning period at the expense of time and money.

4.5 Data pooling results

Based on the tension and compression results discussed in Section 4.4, the data sets are pooled by the methodology discussed in Section 3.4 using CMH-17 STATS software.

4.5.1 Pooled compressive strength degradation curve

Table 4.19 shows the data pooling results of the compressive strength of Hexply 8552/AS4 laminate.

Table 4.19: Data pooling results of the compressive strength of Hexply 8552/AS4 laminate

Parameter	Value
Shape parameter	37.7
Scale parameter	1
A_{pool}	0.845
B_{pool}	0.919

The detailed analysis of data pooling for the compressive strength is shown in Appendix H. Figure 4.12 depicts the scale parameter degradation curve of the compressive strength with moisture content for the Hexply 8552/AS4 laminate.

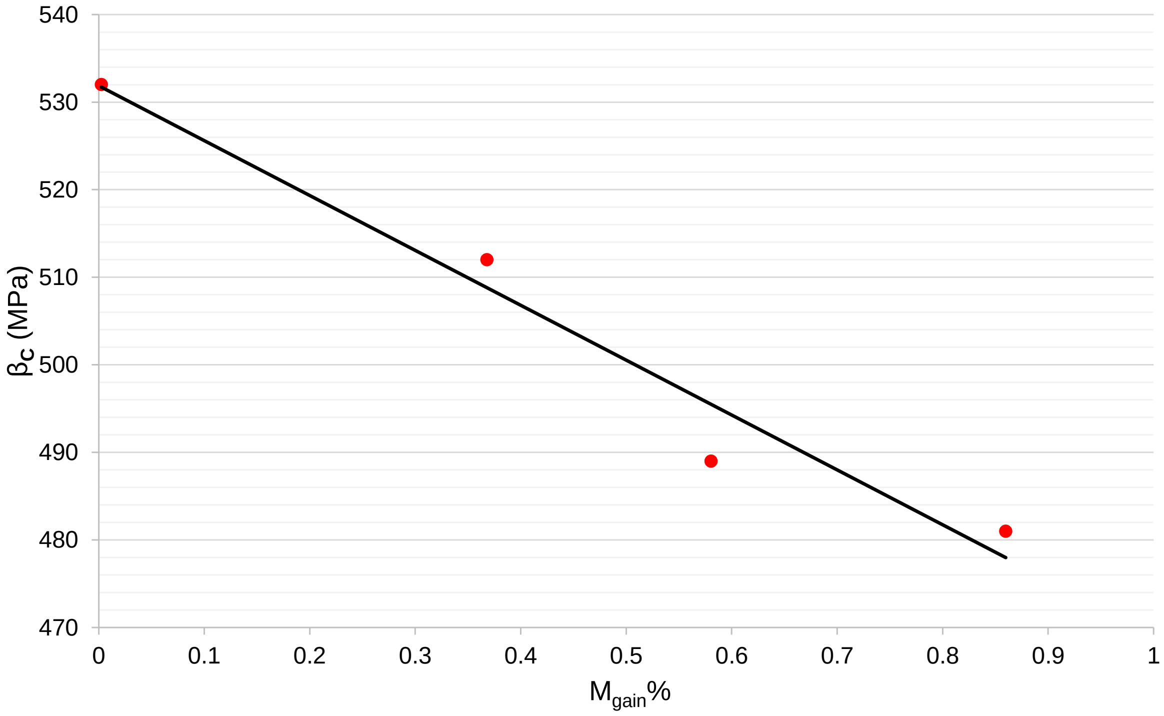

Figure 4.12: Scale parameter degradation curve of the compressive strength for the Hexply 8552/AS4 laminate

It is difficult to comment about the nature of the degradation curve except that the compressive strength decreases with an increase in the moisture content because of the following reasons:

(a) The number of preconditioning periods for which the coupons are tested is small.

(b) No literature exists for the degradation curve of the compressive strength for the Hexply 8552/AS4 laminate with moisture content .

Hence for the sake of simplicity, the data points are fit to a simple linear regression curve, shown in Figure 4.12. The linear regression curve is given by Eq. (4.10).

$$\beta_C = -62.666 \cdot M_{gain} + 531.87 \tag{4.10}$$

Since the analysis is performed only at the maximum moisture content, the degradation curve prediction for the compressive strength at the maximum moisture content is conservative shown in Figure 4.12. The accuracy of the compressive strength degradation curve can be improved by increasing the number of preconditioning periods for which the coupons are tested at the expense of experimental effort and money.

4.5.2 Pooled tensile strength degradation curve

Table 4.20 shows the data pooling results of the tension strength of Hexply 8552/AS4 laminate.

Table 4.20: Data pooling results of the tension strength of Hexply 8552/AS4 laminate

Parameter	Value
Shape parameter	31.1
Scale parameter	1
A_{pool}	0.812
B_{pool}	0.900

Figure 4.13 depicts the scale parameter degradation curve of the tensile strength with moisture content for the Hexply 8552/AS4 laminate.

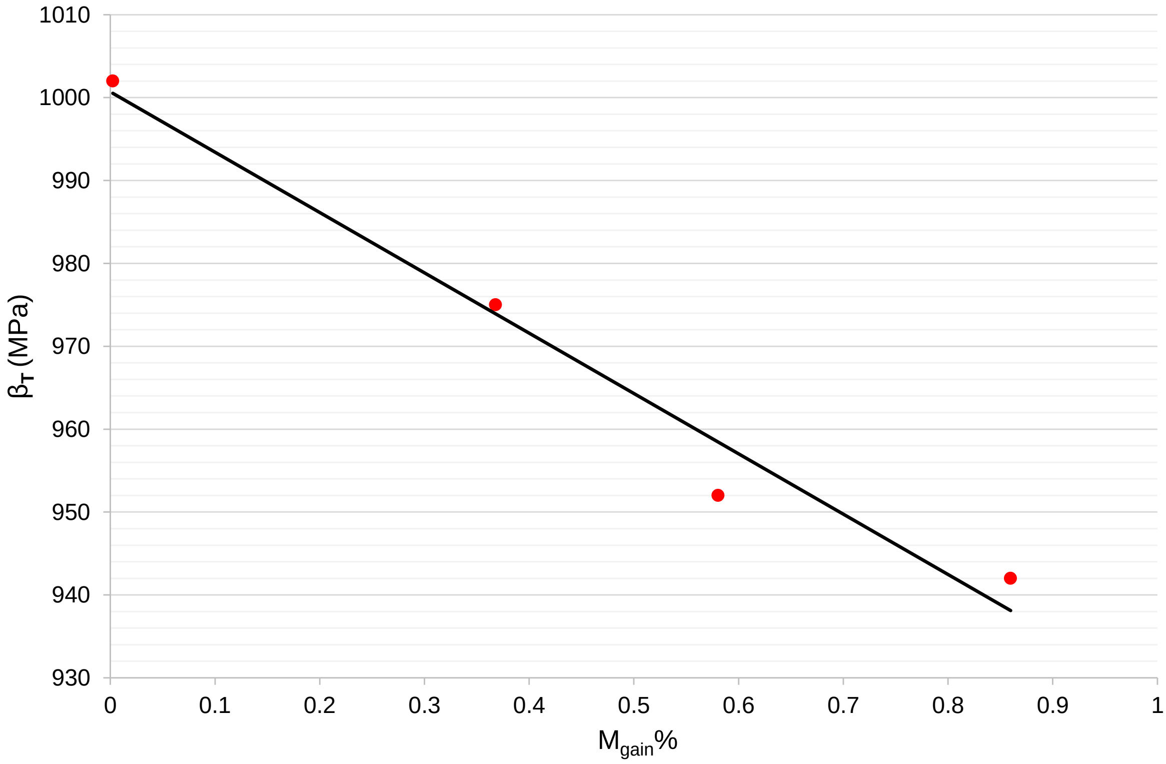

Figure 4.13: Scale parameter degradation curve of the tensile strength for Hexply 8552/AS4 laminate

As mentioned in subsection 4.5.1 for compression tests, the data points for tension tests are similarly fit to a simple linear regression curve, and, is given by Eq. (4.11).

$$\beta_T = -72.783 \cdot M_{gain} + 1000.7 \tag{4.11}$$

Like compressive strength, the degradation curve prediction for the tensile strength at the maximum moisture content is conservative.

4.6 Ideal S-N curves

As mentioned in Section 2.8, the input to the Kassapoglou's model are the static strength of the laminate to plot the S-N curve. In the current study, the Hexply 8552/IM7 laminates are tested in static tension and compression, to determine its corresponding strength values. The layup of the coupon is based on design option B, and, is given by $[0_3, (45/-45)_2, 90_2]s$. The number and dimensions of the coupons are shown in Table 3.10 and Table 3.12 respectively. The static tensile and compression strength results are fit to a Weibull distribution, and, the corresponding results for strength are shown in Table 4.21.

Table 4.21: Static tensile and compressive strength results of Hexply 8552/IM7 laminate

Parameter	Unit	Tension	Compression
Shape parameter	-	16.8	10.9
Scale parameter	MPa	1130	510
A basis	MPa	746	188
B basis	MPa	871	305

4.6.1 S-N curve for Tension-Tension (T-T) fatigue

The shape and scale parameters of the tensile strength, shown in Table 4.21, are substituted in Eq. (2.20), and, the resultant value is substituted in Eq. (2.17), to obtain the S-N curve equation for T-T fatigue and is given by Eq. (4.12).

$$\sigma = \frac{1130}{(N)^{(1/16.8)}} \tag{4.12}$$

4.6.2 S-N curve for Compression-Compression (C-C) fatigue

The shape and scale parameters of compressive strength, shown in Table 4.21, are substituted in Eq. (2.20), and, the resultant value is substituted in Eq. (2.17), to obtain the S-N curve equation for C-C fatigue and is given by Eq. (4.13).

$$\sigma = \frac{510}{(N)^{(1/10.9)}} \tag{4.13}$$

The S-N curves for T-T and C-C fatigues are shown in Figure 4.14.

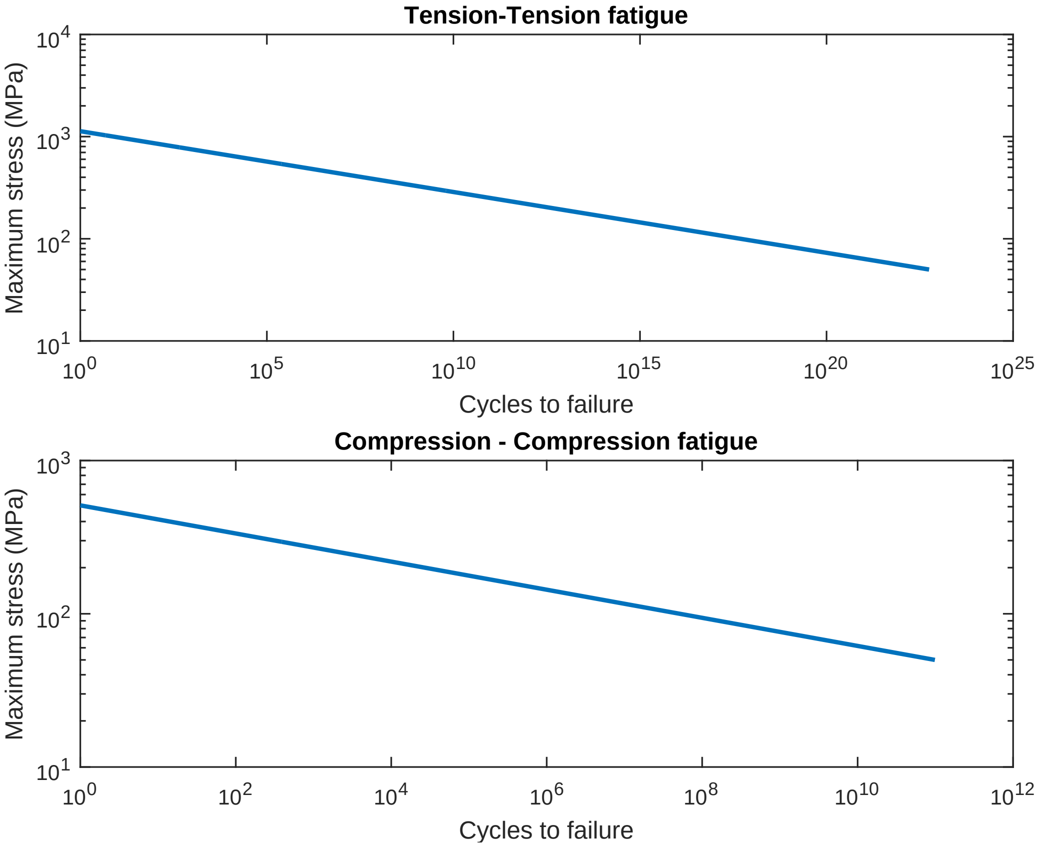

Figure 4.14: S-N curves for T-T and C-C fatigues

It can be inferred from the S-N curves , shown in Figure 4.14, that C-C fatigue is more critical than T-T fatigue because composites are not good against compressive loads. Another interesting observation is that, there is no endurance limit for the composite in T-T and C-C fatigues in principle. It is possible to derive an endurance limit for this model by assigning a low value for the probability of failure that corresponds to zero failure probability. Hence, for the fatigue critical areas of the composite T-boom, a stress allowable can be suggested based on its required life. Finally, as the S-N curves does not take into account the effect of temperature and moisture, they have to be modified based on the methodology discussed in Section 3.5.

4.7 Modified Kassapoglou's model results

The modified S-N curves for the Hexply 8552/IM7 laminate are based on the following assumptions:

- The slope of the degradation curve for the tensile and compressive strengths of the Hexply 8552/IM7 laminate and Hexply 8552/AS4 laminate are equal as mentioned in Section 3.4.

- The shape parameter of the pooled data for the tensile and compressive strengths of the Hexply 8552/IM7 and Hexply 8552/AS4 laminate are equal.

The second assumption is based on the premise that the scatter of the pooled strength values across environment conditions is mostly dependant on the matrix properties. This assumption might be limiting as the shape parameter also depends on the scatter due to fibre properties. Due to time constraints to procure the Hexply 8552/IM7 material, the Hexyply 8552/AS4 material was used for testing across environment conditions and subsequent analysis.

4.7.1 Modified S-N curves for T-T fatigue

The dependency of the scale parameter of the tensile strength for the Hexply 8552/IM7 laminate with moisture content is derived based on Eq. (4.11) and is given by Eq. (4.14).

$$\beta_T = -72.783 \cdot M_{gain} + 1130 \tag{4.14}$$

The shape parameter of the pooled tensile strength is given by Table 4.20, and, the S-N curve equation for the T-T fatigue is given by Eq. (4.15).

$$\sigma = \frac{\beta_T}{(N)^{(1/31.1)}} \tag{4.15}$$

4.7.2 Modified S-N curves for C-C fatigue

The dependency of the scale parameter of the compressive strength for the Hexply 8552/IM7 laminate with moisture content is derived based on Eq. (4.10) and is given by Eq. (4.16).

$$\beta_C = -62.666 \cdot M_{gain} + 510 \tag{4.16}$$

The shape parameter of the pooled compressive strength is given by Table 4.19, and, the S-N curve equation for the C-C fatigue is given by Eq. (4.17).

$$\sigma = \frac{\beta_C}{(N)^{(1/37.7)}} \tag{4.17}$$

The S-N curves for the T-T and C-C fatigue are plotted for moisture contents of 0 and 0.86%, and, are shown in Figure 4.15 and Figure 4.16.

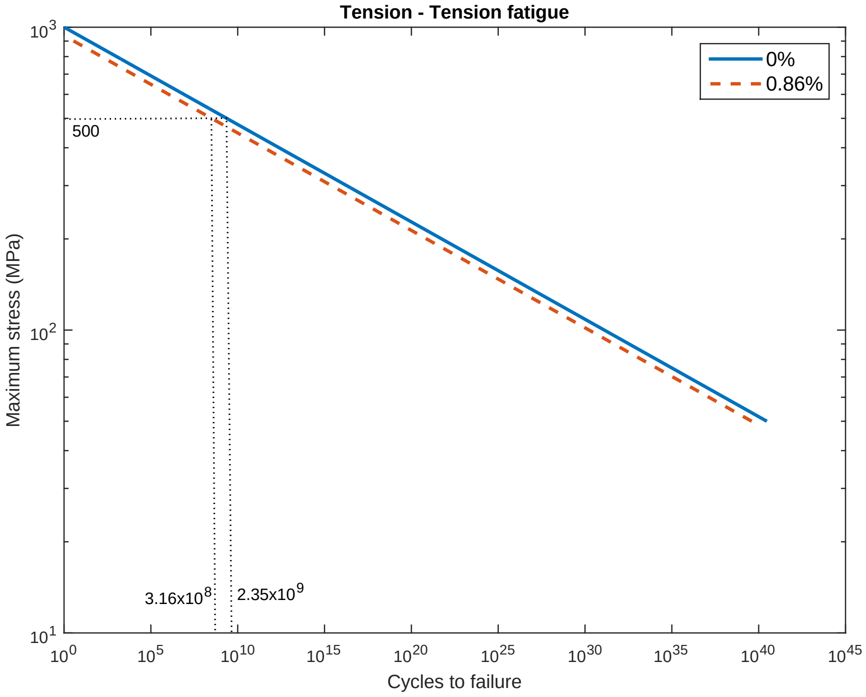

Figure 4.15: Modified S-N curve for T-T fatigue

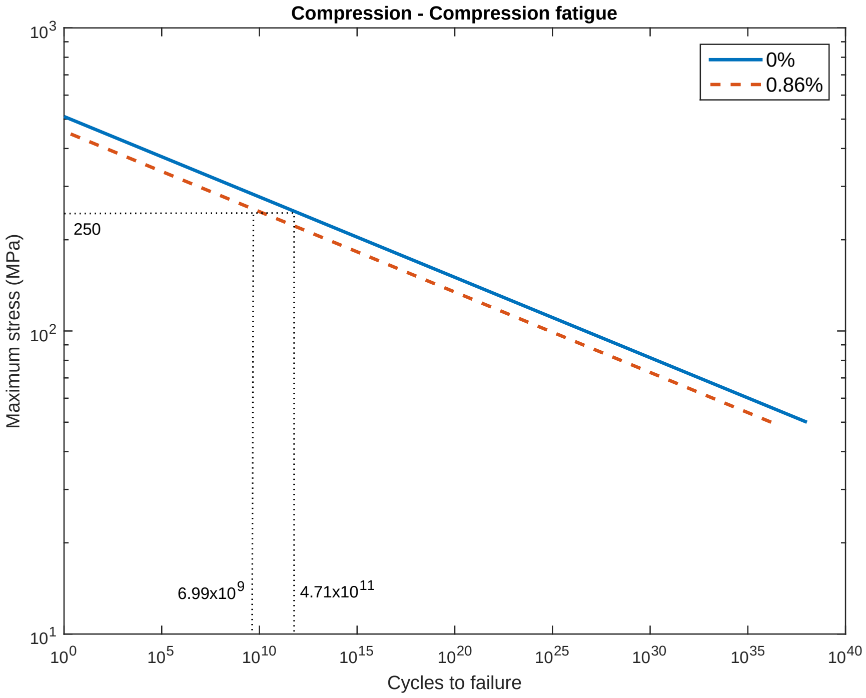

Figure 4.16: Modified S-N curve for C-C fatigue

Based on Figure 4.15 and Figure 4.16, it can be concluded that the effect of moisture and temperature degrades the T-T and C-C fatigue life of the structure. For the T-T fatigue, the cycles to failure for the ideal S-N curve for a maximum stress of 500 MPa is 2.35×10^{9} cycles, while it is 3.16×10^{8} cycles for the modified S-N curve. Similarly, for the C-C fatigue, the cycles to failure for the ideal S-N curve for a maximum stress of 250 MPa is 4.71×10^{11} cycles, while it is 6.99×10^{9} cycles for the modified S-N curve. The percentage reduction in cycles to failure due to moisture and temperature for the T-T and C-C fatigue are approximately 86.6% and 98.5 %, and, should not be neglected in the fatigue analysis.

As mentioned in Section 2.5, the safety factor for the design takes into account a knockdown factor of 0.8 for the effect of environment. Since the reduction in tensile and compressive strength for the moisture content of 0.86%, shown in Figure 4.13 and Figure 4.12 respectively, are less than the reduction in the strength value due to the environment knockdown, it can be concluded the design is conservative against the effect of environment.

The modified S-N curve is based on the assumption that the shape parameter of the pooled data for the tensile and compressive strengths of the Hexply 8552/AS4 and Hexply 8552/IM7 laminate are equal. This assumption leads to non-conservative results since the shape parameter of the former is greater than the latter, shown in Table 4.19, Table 4.20 and Table 4.21 respectively. This is evident from the ideal S-N curves plotted for the T-T and C-C fatigue shown in Figure 4.15, Figure 4.16 for the former and Figure 4.14 for the latter. This is because the S-N curve becomes steeper if the shape parameter decreases resulting in a lower fatigue life for the same maximum stress. This can be solved by testing the Hexply 8552/IM7 laminate for different environment conditions, and, pooling the tests results.

It is difficult to comment about the accuracy of the predictions as the modified fatigue model is not validated. Kassapoglou [28] observes that the model does not give accurate predictions when the static and fatigue failure modes are different. Hence, it is important to test the coupons at low and high cycle fatigue to check if the effect of moisture and temperature have an influence on the fatigue failure mode. The accuracy of the predictions of the modified Kassapoglou's model can be improved by modelling p as a function of the damage present [28].

4.8 Constraints in fatigue life estimation

The fatigue life of the composite T-boom is not estimated in the study due to several constraints which are listed below:

- The fatigue critical areas of the composite T-boom are in a multiaxial state of stress. In order to use the modified Kassapoglou's model to estimate its fatigue life, multiaxial static tests have to be performed to determine the static probability of failure. Due to time constraints and lack of infrastructure in the *DASML* lab to do these tests, the fatigue life is not estimated.
- As Kassapoglou's model is based on residual strength, it is difficult to determine the stiffness degradation during fatigue loading. The gradual deterioration of stiffness in the damaged zones may redistribute the stresses, and, reduce the stress concentrations in the structure which may increase its life. But, as the T-boom is a stiffness based design, the loss of stiffness may also lead to premature buckling at lower loads which

may reduce the life of the structure. Hence, it is quite important to couple a stiffness degradation model with the Kassapoglou's model to accurately estimate the life of the composite T-boom.

4.8.1 Fatigue model proposal to account the multi-axial stress state

Based on the literature study on various residual strength models in Section 2.8, it was concluded that most fatigue models require extensive experimental effort to determine model parameters which limits their applicability to a specific loading condition, layup and material. Hence, the Kassapoglou's model was chosen as it does not require any curve fitting or experimentally determined parameters for predicting the fatigue damage. As mentioned earlier, the limitation of the Kassapoglou's model is that it is difficult to predict the fatigue life of a structure in a multiaxial state of stress as it requires static strength data for multiaxial loading. Hence a proposal is made to modify the existing Kassapoglou's model to make it easier to predict the fatigue life of a structure in a multiaxial stress state.

Philippidis and Vassilopoulos [57] developed a multi-axial fatigue failure criterion based on the Tsai-Wu failure criterion for static loading, and, validated its predictions with various uniaxial and multiaxial experimental fatigue data. The fatigue failure criterion is similar to Eq. (2.15) and is given by Eq. (4.18).

$$\frac{\sigma_1^2}{X_n^t X_n^c} + \frac{\sigma_2^2}{Y_n^t Y_n^c} - \sqrt{\frac{1}{X_n^t X_n^c} + \frac{1}{Y_n^t Y_n^c}} \cdot \sigma_1 \sigma_2 + ..$$

$$.. \left(\frac{1}{X_n^t} - \frac{1}{X_n^c}\right) \cdot \sigma_1 + \left(\frac{1}{Y_n^t} - \frac{1}{Y_n^c}\right) \cdot \sigma_2 + \frac{\tau_{12}^2}{S_n^2} - 1 <= 0 \tag{4.18}$$

where X_n^t, X_n^c, Y_n^t, Y_n^c and S_n are the respective strength values of the ply in MPa, and, are functions of number of cycles, N, the stress ratio, R, and the frequency, ν of the loading. The downside of this approach is that the S-N curves for the ply strength values have to determined experimentally, and, require extensive experimental effort.

The experimental effort for the Philippidis and Vassilopoulos's quadratic fatigue failure tensor polynomial criterion can be significantly reduced by coupling it with the Kassapoglou's model. The S-N curves for the ply strength values can be easily estimated by determining the static probability of failure for the ply in the longitudinal, transverse and shear directions by static tests, and, subsequently applying the Kassapoglou's model. For example, the static probability of failure for the transverse properties of a 0° unidirectional ply can be estimated by uniaxial static tests of 90° unidirectional laminate.

The advantage of using this approach is that the experimental effort required to characterize the S-N curves is considerably reduced, and, the propagation of damage is evaluated at the ply level. Also, no complicated infrastructure/equipment is required to do multiaxial static tests as the fatigue life can be estimated using uniaxial strength data. But at present, it is difficult to comment about the validity of the fatigue failure criterion for the combined loading and variable amplitude loading scenarios, and, has to be researched further which is beyond the scope of the Master thesis.

4.9 Cost estimation

As mentioned in Section 2.5, it is considered relevant to compare the composite T-boom with an equivalent pedestrian bridge. As there are no cost related information for the composite gangways, it is assumed that the cost breakdown for the composite T-boom and pedestrian bridge are the same. Due to time constraints, only the overall cost incurred by Ampelmann to manufacture and maintain the composite T-boom are estimated instead of the life cycle cost. In the analysis, it is assumed that pultrusion is used to manufacture the truss members of the composite T-boom. The cost incurred by Ampelmann to manufacture the composite T-boom can be classified as the following:

- Production cost
- Labour installation cost
- Inspection cost
- Repairs
- Certification cost

4.9.1 Production cost

The total cost of a pultruded Carbon Fibre Reinforced Polymer (CFRP) beam is estimated as \$102.5/kg by Meiarashi, et al [45], and, comprises of various parameters like material costs, mold change costs, labor costs and equipment redemption costs. Since the mass of the preliminary design of the composite T-boom is 520 kg, the raw material cost is estimated as \$53300.

As mentioned in Section 4.1, the current design of the composite T-boom does not take into account the effect of joints. If joints are taken into consideration, the overall production cost is expected to increase due to increase in the weight of the structure, and, the assembly costs attributed to the joints. Also, the associated costs for assembling the secondary attachments on the composite T-boom is not taken into account.

4.9.2 Labour installation cost

Kawahara, et al. [58] estimate the cost of installing the Fibre Reinforced Polymer (FRP) bridge installation as \$3/ft^2. The hourly compensation cost for manufacturing in U.S. increased from \$23.65 in 2005 [59] to \$36.34 in 2013 [60], while in Netherlands, it increased to \$42.26 in 2013 [60]. Hence, the adjusted labour cost for installing the FRP bridges in Netherlands is estimated as $42.26/23.65\times3= 5.4/\text{ft}^2$. It is assumed that the installation cost of the composite T-boom is the same and estimated as $5.40\times13.1\times0.87\times10.76$ = \$663.

Based on Ampelmann reports, the combined production and labour installing costs of the existing T-boom is approximately \$84249. The production cost of the existing T-boom includes raw material cost, machining cost, welding cost and labour cost. The transportation and coating costs are not included in the production cost estimate of the composite and existing T-boom.

4.9.3 Inspection cost

Telang, et al. [61] suggest that visual inspection and tap testing in conjunction with ultrasonic testing are the easiest inspection techniques to incorporate into a bridge inspection program, and, recommend load testing to be performed at the end of manufacturing, and, during in-depth inspection. The inspection schedule and its associated cost for the composite T-boom are based on Murphy [46] and are the following:

- Yearly inspection is carried out annually to ensure that the maintenance activities are properly carried out, and, its associated cost is \$120.
- General Inspection is carried out every 3 years to check for cracks and faults, and to follow up on the previous main inspection. The associated cost for general inspection is \$600.
- Main inspection is carried out every 6 years to ensure that the bridge is safe to operate by thorough inspection of structural elements. The associated cost for main inspection is \$1200.

As mentioned in Section 2.5, the lifetime of the composite T-boom should be 20 years, and, the total inspection cost during its lifetime is estimated as \$7200. Due to lack of inspection records of the existing gangway, it is assumed that weld inspection is carried out every year, and, its associated cost is \$570. Hence, during it lifetime, the total inspection cost of the existing T-boom is \$6840.

The inspection cost does not include miscellaneous expenses like transportation of inspector to the offshore location, and, accommodation for the inspector.

4.9.4 Repairs

The maintenance activities of the composite T-boom are typically related to cleaning of the T-boom, repainting, patchworks and joint repairs etc. Hong and Hastak [62] and Hong, et al. [63] observe that the use of FRP materials to bridge decks have led to minimal maintenance issues, thereby making it difficult to collect maintenance records. Nystrom, et al. [47] estimate the maintenance costs as \$6.51/m^2, and, hence the maintenance cost for the composite T-boom is approximately $6.51\times13.1\times0.87 =$ \$74.

Due to lack of records, the repair costs of the existing T-boom are not considered in the cost analysis.

4.9.5 Certification cost

Due to novelty of the application, the certification costs associated with the gangway retrofitted with composite T-boom are expected to be higher than the existing gangway. At this stage, it is difficult to quantify the exact overall certification cost as it depends on the certifying authority and the tests performed to certify the structure.

Hence for this study, it is assumed that the certification cost are equal for both. Based on Ampelmann reports, the certification cost is approximately \$22000.

Table 4.22 summarizes the cost breakdown of the composite and exiting T-boom.

Table 4.22: Cost breakdown of the composite and existing T-boom

Cost ($)	Composite T-boom	Existing T-boom
Production Labour installation	53,300 663	84,249
Inspection	7,200	6,840
Repair	74	-
Certification	22,000	22,000
Total	83,237	135,089
Total in €(€ 1 = $1.15)	72,323.40	117,376.84

The current cost estimate of the composite T-boom results in a cost reduction of approximately 38%. It is difficult to comment about the accuracy of the cost predictions due to the lack of cost related information for the composite gangways. Based on Table 4.22, it can be concluded that the production cost of the composite T-boom is approximately 64% of the total cost, and, hence the primary cost driver. As said earlier, the weight of the composite T-boom is expected to increase due to the presence of joints, and, reinforcements for secondary attachments. As a result, the production cost of the composite T-boom might increase to an extent that the overall cost incurred by Ampelmann to manufacture, maintain and certify the composite T-boom is greater than the existing T-boom. Nevertheless, the preliminary cost estimate of the composite T-boom looks promising to be researched further. The cost breakdown and estimate has to be refined further by incorporating the inputs from FRP bridge manufacturers and the production department during prototyping which is beyond the scope of this project.

4.10 Chapter Summary

This chapter describes the results obtained during the design and fatigue analysis phase of the composite T-boom. Based on the preliminary design, it is observed that the weight reduction of the composite T-boom is approximately 45.3%. It is expected the weight reduction will be lower if the effect of joints are considered. During the FE and detailed analysis phase, the SC is identified as the worst load case scenario, and, it is concluded the composite T-boom satisfies the design requirements for all the load cases. Subsequently, the results obtained during the material characterization tests are discussed. Due to time constraints, the material is not completely saturated with moisture , and, the subsequent analysis is done at the maximum moisture content. The strength degradation curves for tension and compression are plotted based on the results of data pooling and static tests. The modified S-N curves are subsequently plotted using the Kassapoglou's model and degradation curves. Since, the T-boom is in a multiaxial state of stress, the fatigue life is not estimated in this study, and, a model is proposed to perform multiaxial fatigue analysis using Kassapoglou's model. Finally, the cost of the composite T-boom is estimated, and, compared with the existing T-boom.

Chapter 5

Conclusions and recommendations

This chapter concludes the results obtained during the study, and, suggests recommendations for future research.

5.1 Conclusions

Based on the current study, it can be concluded that it is feasible to design a composite Telescoping boom (T-boom) which satisfies the core requirements set forth by Ampelmann in Section 1.3. The composite T-boom design has a preliminary weight and cost savings of 45% and 38% respectively, as compared to the original steel-based truss structure. Due to certain limitations of the fatigue model, the fatigue life of T-boom in not estimated in the study. The immediate implementation of this design, is however not possible because of many reasons like the effects of joints are ignored, the design is not validated and certified, and, the fatigue life of the T-boom is not estimated. Nevertheless, the current estimate of cost and weight looks promising for the composite T-boom, and, the design has to be researched further.

The preliminary design of the composite T-boom was based on the equivalent stiffness approach where each and every truss member of the existing design was replaced by a Fibre Reinforced Polymer (FRP) box beam of equivalent stiffness. The material system selected for the design of the composite T-boom was Hexply 8552/IM7. Subjected to the design space constraints and stiffness requirements, two possible design options: A and B were selected , and, a suitable layup and cross-section dimensions were determined. Since the design did not take into account the effect of joints and cutouts for the secondary attachments, it was concluded that the overall weight reduction for the composite T-boom would be lower.

One of the primary challenges during the Finite Element (FE) analysis phase was to model the entire T-boom as it required extensive modelling and computational effort. Hence, analysis was done only at regions close to the supports as they are the critical areas. S4R, shell elements were used to model the truss members, and, FE analysis was performed for the worst load cases: Emergency Operation- 3 People Transfer (EO-3PT), Emergency Operation- Extra Length + Cargo (EO-ELC) and Stowed Condition (SC). Both the design options: A and B satisfied the deflection and strength requirements of the composite T-boom for the worst load scenarios. Design option B was selected as the final design option for the composite T-boom as it had a higher margin of safety for the SC and stiffness. The major drawback of of the FE model was that it was impossible to study the global buckling of the T-boom, and, global deflection and natural frequency of the gangway. Another limitation of the analysis was that the effect of stress concentrations at the box beam corners were neglected.

In the detailed analysis phase, parameters like global deflection and natural frequency of the gangway retrofitted with the composite T-boom were estimated analytically by modelling the Main Boom (MB) and T-boom as a cantilever beam. Since the composite T-boom was stiffer and lighter, it was concluded that the T-boom design satisfied the global deflection, natural frequency and buckling requirements. It was also observed that the analytical predictions were conservative as the bending stiffness of the T-boom neglected the contribution of the bracings, members 3-6 and the effect of MB/T-boom interface. One criticism of this approach was that the natural frequencies for the gangway were only estimated for the bending modes when other modes like torsion mode and mixed torsion-bending mode were possible.

Material characterization tests were performed to determine the moisture absorption properties, tensile and compressive strengths of the coupons. Due to time constraints, the coupons were only tested at the maximum Elevated Temperature Wet (ETW) offshore environment possible for the Ampelmann system. Due to lack of sufficient Hexply 8552/IM7 material, tests were performed using the Hexply 8552/AS4 laminate by assuming that the environment resistance of polymer composites were mainly dependant on the matrix. During moisture ingression tests, the coupons were ingressed with moisture at 90% Relative Humidity (R.H.) and 55°C for a period of 8 weeks. It was observed that the moisture absorption curve follows a Fickian diffusion pattern, and, the coupons were not saturated after conditioning them for 8 weeks. It was suggested that the coupons should be allowed to condition further in the climate chamber till they were saturated.

The static tensile and compressive tests were performed for different preconditioning periods, and, the data were pooled to determine the effect of moisture and temperature on the static strength properties. It was observed that the static tensile and compressive strength decreased with an increase in the moisture content due to plasticizer effect of the matrix. Subsequently, the degradation curve for the static tensile and compressive strength were obtained by fitting the data to a linear regression line due to lack of information on the degradation behaviour of the laminate and low number of preconditioning periods for which the coupons were tested. Since the analysis was performed only at the maximum moisture content, it was concluded that the degradation curve prediction for the compressive and tensile strength were conservative. It was recommended that the accuracy of the compressive and tensile strength degradation curve could be improved by increasing the number of preconditioning periods for which the coupons were tested at the expense of experimental effort and money.

The ideal S-N curves were obtained by first testing the Hexply 8552/IM7 laminate for static tensile and compressive strengths, and, subsequently substituting the test statistics in the Kassapoglou's model. It was inferred from the S-N curves that Compression-Compression (C-C) fatigue was more critical than Tension-Tension (T-T) fatigue due to poor performance of composites against compressive loads. Another interesting observation was that, there was no endurance limit for the composite in T-T and C-C fatigues. Hence, for the fatigue critical areas of the composite T-boom, a stress allowable could be suggested based on its required life.

The Kassapoglou's model was subsequently modified to incorporate the effect of moisture and temperature by certain assumptions described in Section 4.7. Based on these assumptions, the modified S-N curves were obtained, and, it was observed that moisture and temperature had a significant effect on the T-T and C-C fatigue. Also, as the reduction in strength due to environment knockdown factor was greater than the reduction due to maximum moisture content, it was concluded the design was conservative against the effect of environment. One criticism of this approach was that the assumption was based on the premise that the shape parameter of the pooled data for the tensile and compressive strengths of the Hexply 8552/AS4 and Hexply 8552/IM7 laminate were equal which led to non-conservative predictions of the fatigue life. Another limitation of this model was that the fatigue life of the T-boom was not estimated as the structure was in a multiaxial state of stress. Due to difficulty in performing the multiaxial static tests, a new fatigue model was proposed where multiaxial fatigue life estimation was possible using simple uniaxial strength data.

Finally, the cost of the composite T-boom was calculated and compared against the existing T-boom. An interesting observation was that the production cost of the composite T-boom was approximately 64% of the total cost, and, hence the primary cost driver. As a result, it was expected that the overall cost of the composite T-boom would substantially increase when the effect of joints and the reinforcements for the secondary attachments were taken into account. It was also recommended to incorporate the inputs from FRP bridge manufacturers and the production department during the cost breakdown and estimate.

5.2 Recommendations

Based on the learnings and assumptions done during the study, some important recommendations can be made.

- The effect of the joints on the structural performance and mass of the T-boom should be studied. As mentioned earlier, joints may result in stress concentrations, and, can act as a hotspot for failure. Also stress concentrations at the joints coupled with the effects of offshore environment may lead to early onset of fatigue, and, may deteriorate the fatigue performance of the T-boom. To reduce the stresses at the joints, reinforcements have to be provided which will increase the overall weight of the structure.
- The preliminary design of the composite T-boom can be optimized further to reduce the mass and cost of the composite T-boom. As the T-boom section near the tip is not highly loaded as compared to the section close to the rollers, the cross-section dimensions of the truss members near the tip can be reduced, thereby reducing the mass of the T-boom. Also, the composite T-boom can be made hybrid by designing the critically loaded regions with carbon fibre/epoxy material system, and, the rest with glass fibre/vinylester or glass fibre/polyester system. This might decrease the overall material costs of the composite T-boom at the expense of mass as the above glass fibre composites are heavier and weaker than the carbon/epoxy system used for the design.
- The FE analysis of the T-boom is performed only at the section close to rollers in order to reduce the computational and modelling effort. The downside of this approach is

that it is impossible to evaluate the global buckling of the entire T-boom, and, global deflection and natural frequency of the gangway retrofitted with the composite T-boom. Hence, the entire T-boom can be modelled and analysed to estimate these parameters as it provides a method to validate the corresponding analytical predictions of the design.

- The coupons should be saturated with moisture at elevated temperature, and, subsequently tested for static tensile and compressive strengths. Since the tensile and compressive strength degrades with moisture content shown in Figure 4.13 and Figure 4.12 respectively, it can be concluded that the maximum reduction in static strength values are expected for the effective moisture content, M_m, resulting in conservative predictions of fatigue life.

- The modified Kassapoglou's model should be validated by testing the coupons at low and high cycle fatigue.

- The degradation curve for the Hexply 8552/IM7 laminate due to ETW condition should be studied to modify the S-N curves obtained during the study. The modified S-N curves were based on the assumption that the shape parameter of the pooled data for the tensile and compressive strengths of the Hexply 8552/AS4 and Hexply 8552/IM7 laminate are equal which lead to non-conservative results.

- In the project, the degradation curves are fit to a simple linear regression curve due to limited number of data points tested at different preconditioning periods. The predictions of the static strength tests statistic and degradation curves can be improved by testing more number of coupons at different preconditioning periods. Since, the time and money to perform these tests increase proportionately to the number of coupons tested, it is important to make a sound judgement on the optimal number of coupons and preconditioning periods required to perform these tests.

- The Kassapoglou's model can be made robust by making it easier to predict the fatigue life of a structure in a multiaxial state of stress using the methodology discussed in Section 4.8, and, hence should be studied further.

References

[1] D. J. Cerda Salzmann. *Ampelmann : development of the access system for offshore wind turbines*. BOXPress, Oisterwijk :, 2010.

[2] I. M. Daniel and O. Ishai. *Engineering Mechanics of Composite Materials (2nd Edition)*. Oxford University Press, 2006.

[3] D. W. Chalmers. Experience in design and production of FRP marine structures. *Marine Structures*, 4(2):93–115, 1991.

[4] I. Kimpara. Use of advanced composite materials in marine vehicles. *Marine Structures*, 4(2):117–127, 1991.

[5] D. W. Chalmers. The potential for the use of composite materials in marine structures. *Marine Structures*, 7(2):441–456, 1994.

[6] D. N. Veritas. Offshore standard DNV-OS-C501: Composite Components, 2013.

[7] L. Register. Code for Lifting Appliances in a Marine Environment, 2013.

[8] S. Shroff. *Design, Analysis, Fabrication and Testing of Grid-Stiffened for Fuselage Applications*. Thesis, 2014.

[9] S. M. Huybrechts, S. E. Hahn, and T. E. Meink. Grid stiffened structures: a survey of fabrication, analysis and design methods. In *Proceedings of the 12th International Conference on Composite Materials (ICCM/12). Paris, France*, 1999.

[10] J. S. Groenier, M. Eriksson, and S. Kosmalski. A Guide to Fiber-Reinforced Polymer Trail Bridges. Report, 2011.

[11] AASHTO. *Guide Specifications for Design of FRP Pedestrian Bridge*. American Association of State Highway and Transportation Officials, Washington, D.C., 1st edition, 2008.

[12] C. Kassapoglou. *Design and analysis of composite structures : with applications to aerospace structures*. John Wiley & Sons Inc., Chichester, West Sussex, United Kingdom :, 2nd edition, 2013.

[13] Military Handbook - MIL-HDBK-17-3F: Composite Materials Handbook, Volume 3 - Polymer Matrix Composites Materials Usage, Design, and Analysis. Report N/A, U.S. Department of Defense, 2002.

[14] S. W. Tsai and E. M. Wu. A General Theory of Strength for Anisotropic Materials. *Journal of Composite Materials*, 5(1):58–80, 1971.

[15] C. Bathias. An engineering point of view about fatigue of polymer matrix composite materials. *International Journal of Fatigue*, 28(10):1094–1099, 2006.

[16] R. C. Alderliesten. Critical review on the assessment of fatigue and fracture in composite materials and structures. *Engineering Failure Analysis*, 35:370–379, 2013.

[17] J. Degrieck and W. Van Paepegem. Fatigue damage modeling of fibre-reinforced composite materials: Review. *Applied Mechanics Reviews*, 54(4):279–300, 2001.

[18] M. M. Shokrieh and L. B. Lessard. Progressive fatigue damage modeling of composite materials, Part I: Modeling. *Journal of Composite Materials*, 34(13):1056–1080, 2000.

[19] M. M. Shokrieh and R. Rafiee. Simulation of fatigue failure in a full composite wind turbine blade. *Composite Structures*, 74(3):332–342, 2006.

[20] W. Lian and W. Yao. Fatigue life prediction of composite laminates by FEA simulation method. *International Journal of Fatigue*, 32(1):123–133, 2010.

[21] H. Mao and S. Mahadevan. Fatigue damage modelling of composite materials. *Composite Structures*, 58(4):405–410, 2002.

[22] W. X. Yao and N. Himmel. A new cumulative fatigue damage model for fibre-reinforced plastics. *Composites Science and Technology*, 60(1):59–64, 2000.

[23] A. D'Amore, M. Giorgio, and L. Grassia. Modeling the residual strength of carbon fiber reinforced composites subjected to cyclic loading. *International Journal of Fatigue*, 78:31–37, 2015.

[24] H. Whitworth. Modeling stiffness reduction of graphite/epoxy composite laminates. *Journal of composite materials*, 21(4):362–372, 1987.

[25] F. Wu and W. Yao. A fatigue damage model of composite materials. *International Journal of Fatigue*, 32(1):134–138, 2010.

[26] T. P. Philippidis and V. A. Passipoularidis. Residual strength after fatigue in composites: Theory vs. experiment. *International Journal of Fatigue*, 29(12):2104–2116, 2007.

[27] N. L. Post, S. W. Case, and J. J. Lesko. Modeling the variable amplitude fatigue of composite materials: A review and evaluation of the state of the art for spectrum loading. *International Journal of Fatigue*, 30(12):2064–2086, 2008.

[28] C. Kassapoglou. Fatigue life prediction of composite structures under constant amplitude loading. *Journal of Composite Materials*, 41(22):2737–2754, 2007.

[29] C. Kassapoglou. Fatigue model for composites based on the cycle-by-cycle probability of failure: implications and applications. *Journal of Composite Materials*, 45(3):261–277, 2009.

[30] C. Kassapoglou. Fatigue of composite materials under spectrum loading. *Composites Part A: Applied Science and Manufacturing*, 41(5):663–669, 2010.

[31] A. Kootsookos and A. P. Mouritz. Seawater durability of glass- and carbon-polymer composites. *Composites Science and Technology*, 64(10-11):1503–1511, 2004.

[32] S. Akbar and T. Zhang. Moisture Diffusion in Carbon/Epoxy Composite and the Effect of Cyclic Hygrothermal Fluctuations: Characterization by Dynamic Mechanical analysis (DMA) and Interlaminar Shear strength (ILSS). *The Journal of Adhesion*, 84(7):585–600, 2008.

[33] S. Srihari and R. M. V. G. K. Rao. Hygrothermal Characterization and Diffusion Studies on Carbon/Epoxy Composites. *Journal of Reinforced Plastics and Composites*, 18(10):921–930, 1999.

[34] S. C. George and S. Thomas. Transport phenomena through polymeric systems. *Progress in Polymer Science*, 26(6):985–1017, 2001.

[35] C. Wang, J. Wang, and T. Su. Determination of Water Diffusion Coefficients and Dynamics in Adhesive/Carbon Fiber-Reinforced Phenolic Resin Composite Joints. *The Journal of Adhesion*, 83(3):255–265, 2007.

[36] B. Dao, J. Hodgkin, J. Krstina, J. Mardel, and W. Tian. Accelerated aging versus realistic aging in aerospace composite materials. v. the effects of hot/wet aging in a structural epoxy composite. *Journal of Applied Polymer Science*, 115(2):901–910, 2010.

[37] W. W. Wright. The effect of diffusion of water into epoxy resins and their carbon-fibre reinforced composites. *Composites*, 12(3):201–205, 1981.

[38] Roger Vodicka. Accelerated environmental testing of composite materials. Report, DTIC Document, 1998.

[39] B. C. Ray. Temperature effect during humid ageing on interfaces of glass and carbon fibers reinforced epoxy composites. *Journal of Colloid and Interface Science*, 298(1):111–117, 2006.

[40] Military Handbook - MIL-HDBK-17-1F: Composite Materials Handbook, Volume 1 - Polymer Matrix Composites Guidelines for Characterization of Structural Materials. Report N/A, U.S. Department of Defense, 2002.

[41] P. Shyprykevich. *The role of statistical data reduction in the development of design allowables for composites.* Test Methods and Design Allowables for Fibrous Composites 2nd volume. ASTM International, 1989.

[42] J. S. Tomblin, Y.C. Ng, and K. S. Raju. Material qualification and equivalency for polymer matrix composite material systems. Report, DTIC Document, 2001.

[43] Y. Li, S. Badjie, W. W. Chen, and Y. Chiu. Case study of first all-GFRP pedestrian bridge in Taiwan. *Case Studies in Construction Materials*, 1:83–95, 2014.

[44] Y. Shen, M. Xu, K. Chandrashekhara, and A. Nanni. Finite element analysis of FRP tube assemblies for bridge decks. *Advanced Composite Materials*, 11(2):151–169, 2002.

[45] S. Meiarashi, I. Nishizaki, and T. Kishima. Life-Cycle Cost of All-Composite Suspension Bridge. *Journal of Composites for Construction*, 6(4):206–214, 2002.

[46] N. Murphy. *Feasibility Analysis of a Fiber Reinforced Polymer Bridge.* Thesis, 2013.

[47] H. Nystrom, S. Watkins, A. Nanni, and S. Murray. Financial Viability of Fiber-Reinforced polymer (FRP) Bridges. *Journal of Management in Engineering*, 19(1):2–8, 2002.

[48] J. F. Davalos and P. Qiao. A computational approach for analysis and optimal design of frp beams. *Computers & Structures*, 70(2):169–183, 1999.

[49] J. Lee and S. Lee. Flexural-torsional behavior of thin-walled composite beams. *Thin-Walled Structures*, 42(9):1293–1305, 2004.

[50] N. Kim and D. Choi. Shear deformable finite beam elements for composite box beams. *Acta Mechanica Sinica*, 30(2):223–240, 2014.

[51] S. B. Singh and Himanshu Chawla. *Structural Response of Thin-Walled FRP Laminated Mono-symmetrical I-Beams*, pages 2011–2024. Springer India, New Delhi, 2015.

[52] ABAQUS User's Manual. Version 6.5, Hibbitt, Karlsson and Sorensen. *Inc., Pawtucket, RI*, 2004.

[53] L. C. Bank and P. J. Bednarczyk. A beam theory for thin-walled composite beams. *Composites Science and Technology*, 32(4):265–277, 1988.

[54] T. Irvine. Bending frequencies of beams, rods, and pipes. *Compare*, 500:50, 2012.

[55] K. Marlett, Y. Ng, and J. Tomblin. Hexcel 8552 IM7 unidirectional prepreg 190 gsm & 35 percentage rc qualification material property data report. *National Center for Advanced Materials Performance, Wichita, Kansas. Test Report CAM-RP-2009-015, Rev. A*, pages 1–238, 2011.

[56] C. Kassapoglou. *Modeling the Effect of Damage in Composite Structures Simplified Approaches.* Wiley, Hoboken :, 2015.

[57] T. P. Philippidis and A. P. Vassilopoulos. Fatigue Strength Prediction under Multiaxial Stress. *Journal of Composite Materials*, 33(17):1578–1599, 1999.

[58] B. Kawahara, H. Estrada, and L. S. Lee. *Life-Cycle Cost Comparison for Steel Reinforced Concrete and Fiber Reinforced Polymer Bridge Decks*, pages 237–273. Springer Netherlands, Dordrecht, 2012.

[59] International Comparisons of Hourly Compensation Costs for Production Workers in Manufacting, 2004. Report, BUREAU OF LABOR STATISTICS, 2005.

[60] M. Levinson. U.S. manufacturing in international perspective, 2014.

[61] N. M. Telang, C. Dumlao, A. B. Mehrabi, A. T. Ciolko, and J. Gutierrez. *Field inspection of in-service FRP bridge decks.* Transportation Research Board, 2006.

[62] T. Hong and M. Hastak. Construction, Inspection, and Maintenance of FRP Deck Panels. *Journal of Composites for Construction*, 10(6):561–572, 2006.

[63] T. Hong, S. Han, and S. Lee. Simulation-based determination of optimal life-cycle cost for FRP bridge deck panels. *Automation in Construction*, 16(2):140–152, 2007.

Appendix A

Existing Telescoping boom (T-boom) design

This appendix describes the cross-section details of the existing T-boom, and, calculates the membrane and bending stiffness of the chords and bracings.

A.1 Existing gangway GXL arrangement

A.2 Cross-section details of the existing T-boom

It is assumed that the modulus of steel, $\mathrm{E}_{steel} = 210$ GPa

The cross-section details of member 1 are shown in Figure A.1,

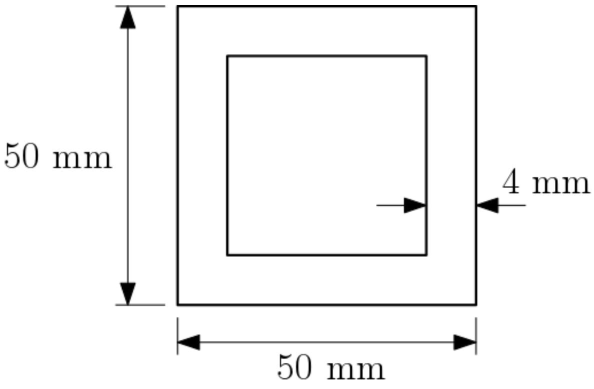

Figure A.1: Cross-section details of member 1

- Area of member 1, $A_{steel} = 736 \text{ mm}^2$

- Moment of inertia of member 1 along x$_1$ axis, $I_{steel,x1} = \frac{1}{12} \cdot (50^4 - 42^4) = 2.62 \cdot 10^5$ mm^4
- Moment of inertia of member 1 along y$_1$ axis, $I_{steel,y1} = 2.62 \cdot 10^5$ mm^4
- Axial stiffness of member 1, $EA_{steel} = 1.55 \cdot 10^8$ N
- Bending stiffness of member 1 along x$_1$ axis, $EI_{steel,x1} = 5.5 \cdot 10^{10}$ N·mm^2
- Bending stiffness of member 1 along y$_1$ axis, $EI_{steel,y1} = 5.5 \cdot 10^{10}$ N·mm^2

The cross-section details of member 2 are shown in Figure A.2,

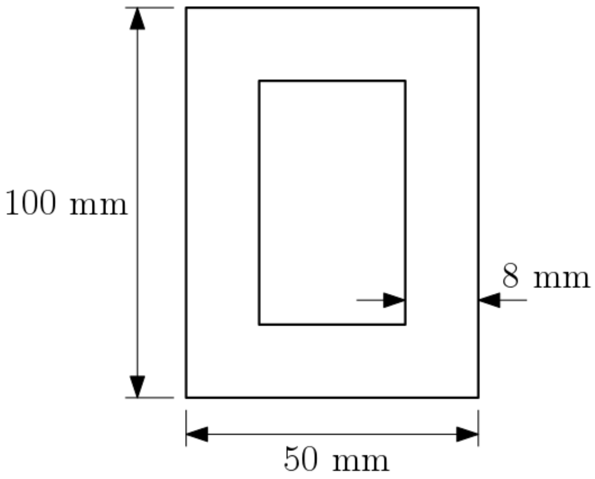

Figure A.2: Cross-section details of member 2

- Area of member 2, $A_{steel} = 2144$ mm^2
- Moment of inertia of member 2 along x$_1$ axis, $I_{steel,x1} = \frac{1}{12} \cdot (50 \cdot 100^3 - 34 \cdot 84^3) = 2.49 \cdot 10^6$ mm^4
- Moment of inertia of member 2 along y$_1$ axis, $I_{steel,y1} = \frac{1}{12} \cdot (50^3 \cdot 100 - 34^3 \cdot 84) = 7.67 \cdot 10^5$ mm^4
- Axial stiffness of member 2, $EA_{steel} = 4.50 \cdot 10^8$ N
- Bending stiffness of member 2 along x$_1$ axis, $EI_{steel,x1} = 5.23 \cdot 10^{11}$ N·mm^2
- Bending stiffness of member 2 along y$_1$ axis, $EI_{steel,y1} = 1.61 \cdot 10^{11}$ N·mm^2

The cross-section details of member 3 are shown in Figure A.3,

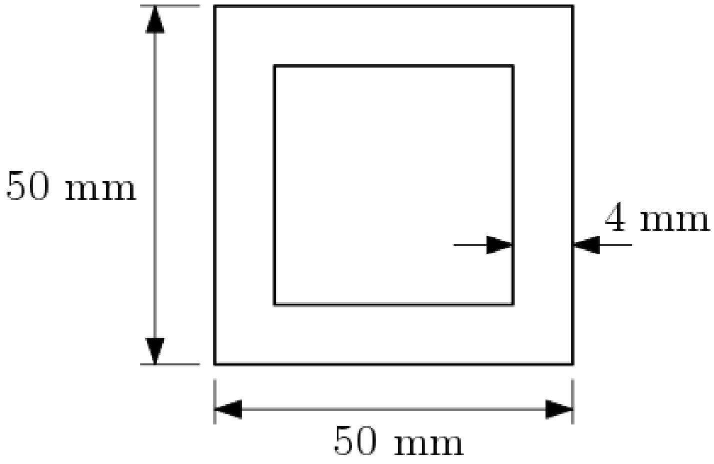

Figure A.3: Cross-section details of member 3

- Area of member 3, $A_{steel} = 736$ mm^2
- Moment of inertia of member 3 along x$_1$ axis, $I_{steel,x1} = \frac{1}{12} \cdot (50^4 - 42^4) = 2.62 \cdot 10^5$ mm^4
- Moment of inertia of member 3 along y$_1$ axis, $I_{steel,y1} = 2.62 \cdot 10^5$ mm^4
- Axial stiffness of member 3, $EA_{steel} = 1.55 \cdot 10^8$ N
- Bending stiffness of member 3 along x$_1$ axis, $EI_{steel,x1} = 5.5 \cdot 10^{10}$ N·mm^2
- Bending stiffness of member 3 along y$_1$ axis, $EI_{steel,y1} = 5.5 \cdot 10^{10}$ N·mm^2

The cross-section details of member 4 are shown in Figure A.4,

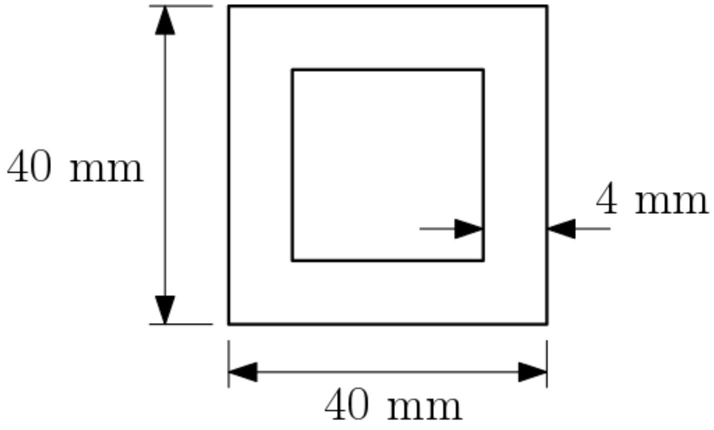

Figure A.4: Cross-section details of member 4

- Area of member 4, $A_{steel} = 576$ mm^2
- Moment of inertia of member 4 along x$_1$ axis, $I_{steel,x1} = \frac{1}{12} \cdot (40^4 - 32^4) = 1.26 \cdot 10^5$ mm^4

- Moment of inertia of member 4 along y_1 axis, $I_{steel,y1} = 1.26 \cdot 10^5$ mm^4
- Axial stiffness of member 4, $EA_{steel} = 1.21 \cdot 10^8$ N
- Bending stiffness of member 4 along x_1 axis, $EI_{steel,x1} = 2.64 \cdot 10^{10}$ N·mm^2
- Bending stiffness of member 4 along y_1 axis, $EI_{steel,y1} = 2.64 \cdot 10^{10}$ N·mm^2

The cross-section details of member 5 are shown in Figure A.5,

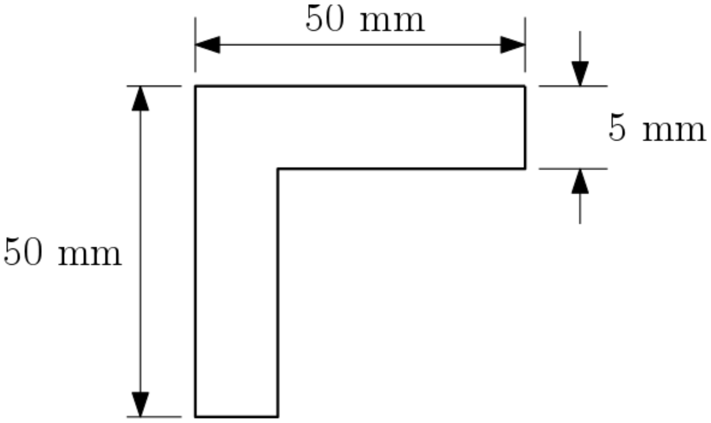

Figure A.5: Cross-section details of member 5

- Area of member 5, $A_{steel} = 475$ mm^2
- Moment of inertia of member 5 along x_1 axis, $I_{steel,x1} = 1.13 \cdot 10^5$ mm^4
- Moment of inertia of member 5 along y_1 axis, $I_{steel,y1} = 1.13 \cdot 10^5$ mm^4
- Axial stiffness of member 5, $EA_{steel} = 9.98 \cdot 10^7$ N
- Bending stiffness of member 5 along x_1 axis, $EI_{steel,x1} = 2.37 \cdot 10^{10}$ N·mm^2
- Bending stiffness of member 5 along y_1 axis, $EI_{steel,y1} = 2.37 \cdot 10^{10}$ N·mm^2

The cross-section details of member 6 are shown in Figure A.6,

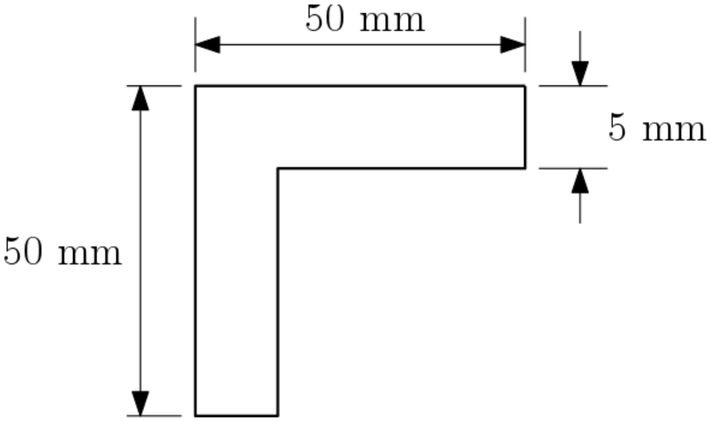

Figure A.6: Cross-section details of member 6

- Area of member 6, $A_{steel} = 475$ mm^2
- Moment of inertia of member 6 along x$_1$ axis, $I_{steel,x1} = 1.13 \cdot 10^5$ mm^4
- Moment of inertia of member 6 along y$_1$ axis, $I_{steel,y1} = 1.13 \cdot 10^5$ mm^4 item
- Axial stiffness of member 6, $EA_{steel} = 9.98 \cdot 10^7$ N
- Bending stiffness of member 6 along x$_1$ axis, $EI_{steel,x1} = 2.37 \cdot 10^{10}$ N·mm^2
- Bending stiffness of member 6 along y$_1$ axis, $EI_{steel,y1} = 2.37 \cdot 10^{10}$ N·mm^2

A.3 Bending stiffness of the existing T-boom

Figure A.7 shows the cross-section of the steel T-boom considered for the bending stiffness calculation.

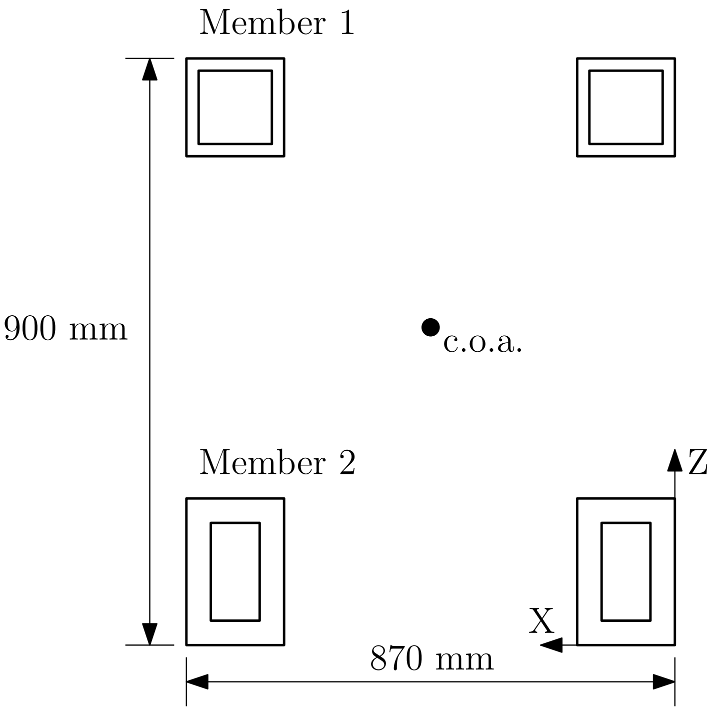

Figure A.7: Cross-section of the T-boom for bending stiffness calculation

The centre of area (c.o.a.) of the cross-section in the x and z direction is given by Eq. (A.1) and Eq. (A.2) respectively.

$$x_{coa} = \frac{(25 \cdot 736 + 25 \cdot 2144 + 845 \cdot 2144 + 845 \cdot 736)}{2 \cdot (736 + 2144)} = 435\ mm \tag{A.1}$$

$$z_{coa} = \frac{(875 \cdot 736 + 50 \cdot 2144 + 50 \cdot 2144 + 875 \cdot 736)}{2 \cdot (736 + 2144)} = 260.833\ mm \tag{A.2}$$

The moment of inertia of the members about the c.o.a. is given from Eq. (A.3) to Eq. (A.6).

For member 1,

$$I_{1,coa,x} = 2.62 \cdot 10^5 + 736 \cdot (875 - 260.833)^2 = 2.78 \cdot 10^8 \ mm^4 \tag{A.3}$$

$$I_{1,coa,z} = 2.62 \cdot 10^5 + 736 \cdot (435 - 25)^2 = 1.24 \cdot 10^8 \ mm^4 \tag{A.4}$$

For member 2,

$$I_{2,coa,x} = 2.49 \cdot 10^6 + 2144 \cdot (260.833 - 50)^2 = 9.78 \cdot 10^7 \ mm^4 \tag{A.5}$$

$$I_{2,coa,z} = 7.67 \cdot 10^5 + 2144 \cdot (435 - 25)^2 = 3.612 \cdot 10^8 \ mm^4 \tag{A.6}$$

Hence, the moment of inertia of the cross-section about its c.o.a. in the x and z axis is given by Eq. (A.7) and Eq. (A.8) respectively.

$$I_{coa,x} = 2 \cdot (I_{1,coa,x} + I_{2,coa,x}) = 7.52 \cdot 10^8 \ mm^4 \tag{A.7}$$

$$I_{coa,z} = 2 \cdot (Iz_{1,coa,z} + Iz_{2,coa,z}) = 9.7 \cdot 10^8 \ mm^4 \tag{A.8}$$

Finally, the bending stiffness of the cross-section in the x and z axis is given by Eq. (A.9) and Eq. (A.10) respectively.

$$EI_{Tboom,x} = E_{steel} \cdot I_{coa,x} = 1.57 \cdot 10^{14} \ N \cdot mm^2 \tag{A.9}$$

$$EI_{Tboom,z} = E_{steel} \cdot I_{coa,z} = 2.04 \cdot 10^{14} \ N \cdot mm^2 \tag{A.10}$$

Appendix B

Technical data sheet : Hexcel

The technical data sheet of the Hexcel 8552 prepregs are given below.

HexPly® 8552

Epoxy matrix (180°C/356°F curing matrix)

Product Data

Description

HexPly® 8552 is a high performance tough epoxy matrix for use in primary aerospace structures. It exhibits good impact resistance and damage tolerance for a wide range of applications.

HexPly® 8552 is an amine cured, toughened epoxy resin system supplied with unidirectional or woven carbon or glass fibres.

HexPly® 8552 was developed as a controlled flow system to operate in environments up to 121°C *(250°F)*.

Benefits and Features

- Toughened epoxy matrix with excellent mechanical properties
- Elevated temperature performance
- Good translation of fibre properties
- Controlled matrix flow in processing
- Available on various reinforcements
- Excellent drape and tack

Resin Matrix Properties

Rheology

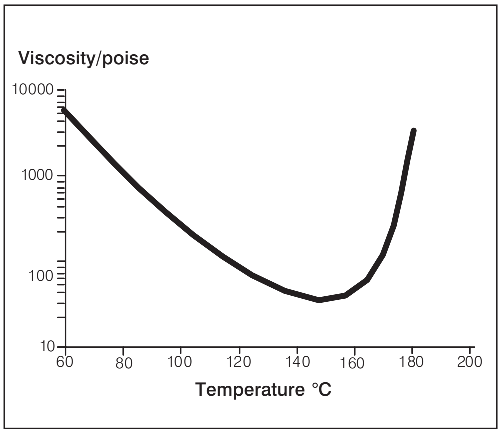

Gel Time

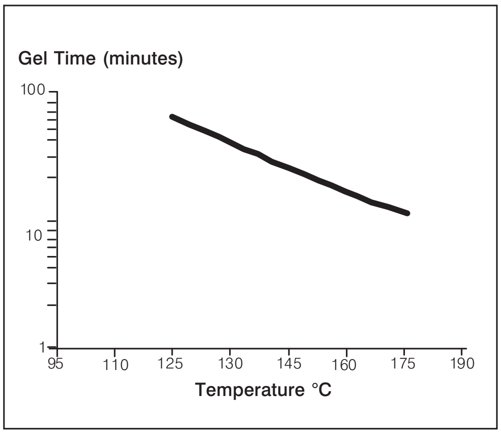

HexPly® 8552

Prepreg Properties - HexPly® 8552 UD Carbon Prepregs

Physical Properties

	Units	AS4	IM7
Fibre Density Filiament count/tow Resin density	g/cm^3 *(lb/in^3)* g/cm^3 *(lb/in^3)*	1.79 *(0.065)* 12K 1.30 *(0.047)*	1.77 *(0.064)* 12K 1.30 *(0.047)*
Nominal Cured Ply Thickness 8552 /35%/134	mm *(inch)*	0.130 *(0.0051)*	0.131 *(0.0052)*
Nominal Fibre Volume	%	57.42	57.70
Nominal Laminate Density	g/cm^3 *(lb/in^3)*	1.58 *(0.057)*	1.57 *(0.057)*

Mechanical Properties

Test	Units	Temp °C *(°F)*	Condition	AS4	IM7
0°Tensile Strength	MPa *(ksi)*	-55*(-67)* 25*(77)* 91*(195)*	Dry Dry Dry	1903 *(267)* 2207 *(320)* -	2572 *(373)* 2724 *(395)* **2538 *(368)****
90°Tensile Strength	MPa *(ksi)*	-55*(-67)* 25*(77)* 93*(200)*	Dry Dry Dry	- 81 *(11.7)* 75 *(10.9)*	174 *(25.3)* 64 *(9.3)* **92 *(13.3)****
0°Tensile Modulus	GPa *(msi)*	-55*(-67)* 25*(77)* 91*(195)*	Dry Dry Dry	134 *(19.4)* 141 *(20.5)* -	163 *(23.7)* 164 *(23.8)* **163 *(23.7)****
90°Tensile Modulus	GPa *(msi)*	- 25*(77)* 93*(200)*	- Dry Dry	- 10 *(1.39)* 8 *(1.22)*	- 12 *(1.7)* **10 *(1.5)****
0°Compression Strength	MPa *(ksi)*	-55*(-67)* 25*(77)* 91*(195)*	Dry Dry Dry	1586 *(230)* 1531 *(222)* 1296 *(184)*	- 1690 *(245)* 1483 *(215)*
0°Compression Modulus	GPa *(msi)*	-55*(-67)* 25*(77)* 91*(195)*	Dry Dry Dry	124 *(18)* 128 *(18.6)* 122 *(17.7)*	- 150 *(21.7)* 162 *(23.5)*
0° ILSS (Shortbeam shear)	MPa *(ksi)*	-55*(-67)* 25*(77)* 91*(195)* 25*(77)* 71*(160)* 91*(195)*	Dry Dry Dry Wet Wet Wet	164 *(23.8)* 128 *(18.5)* 122 *(14.7)* 117 *(16.9)* 84 *(12.2)* 78 *(11.3)*	- 137 *(19.9)* **94 *(13.6)**** 115 *(16.7)* **80 *(11.6)***** -
In-plane Shear Strength	MPa *(ksi)*	25*(77)* 93*(200)*	Dry Dry	114 *(16.6)* 105 *(15.2)*	120 *(17.4)* **106 *(15.4)****

Bold 93°C *(200°F)* **Bold* 104°C *(220°F)*** **Bold** 82°C *(180°F)***

Prepreg Properties - HexPly® 8552 Woven Carbon Prepregs (AS4 Fibre)

Physical Properties

	Units	AGP193-PW	AGP 280-5H
Fibre Type	-	AS4 3K	AS4 3K
Fibre density	g/cm³ *(lb/in³)*	1.77 *(0.065)*	1.77 *(0.065)*
Weave	-	Plain	5HS
Mass	g/m² *(oz/yd²)*	193 *(5.69)*	286 *(8.44)*
Weight Ratio, Warp : Fill		50 :50	50 :50
Nominal cured ply thickness @ 37% resin content	mm *(inch)*	0.195 *(0.0076)*	0.289 *(0.0114)*
Nominal Fibre Volume	%	55.29	55.29
Nominal Laminate Density	g/cm³ *(lb/in³)*	1.57 *(0.057)*	1.57 *(0.057)*

Mechanical Properties

Test	Units	Temp°C (°F)	Condition	AGP193-PW	AGP280- 5H
0°Tensile Strength	MPa *(ksi)*	-55*(-67)*	Dry	766 *(111)*	828 *(120)*
		25*(77)*	Dry	828 *(120)*	876 *(127)*
		91*(195)*	Dry	-	903 *(131)*
90°Tensile Strength	MPa *(ksi)*	-55*(-67)*	Dry	710 *(103)*	752 *(109)*
		25*(77)*	Dry	793 *(115)*	800 *(116)*
		93*(200)*	Dry	759 *(110)*	772 *(112)*
0°Tensile Modulus	GPa *(msi)*	-55*(-67)*	Dry	66 *(9.5)*	70 *(10.2)*
		25*(77)*	Dry	68 *(9.8)*	67 *(9.7)*
		91*(195)*	Dry	-	69 *(10)*
90°Tensile Modulus	GPa *(msi)*	-55*(-67)*	Dry	66 *(9.6)*	67 *(9.7)*
		25*(77)*	Dry	66 *(9.5)*	66 *(9.5)*
		93*(200)*	Dry	68 *(9.8)*	65 *(9.4)*
0°Compression Strength	MPa *(ksi)*	-55*(-67)*	Dry	959 *(139)*	-
		25*(77)*	Dry	883 *(128)*	924 *(134)*
		91*(195)*	Dry	759 *(110)*	**752 *(109)***
0°Compression Modulus	GPa *(msi)*	-55*(-67)*	Dry	60 *(8.7)*	-
		25*(77)*	Dry	60 *(8.7)*	64 *(9.3)*
		91*(195)*	Dry	61 *(8.8)*	**67*(9.7)***
0° ILSS (Shortbeam shear)	MPa *(ksi)*	-55*(-67)*	Dry	101 *(14.6)*	-
		25*(77)*	Dry	84 *(12.2)*	79 *(11.4)*
		91*(195)*	Dry	70 *(10.2)*	-
		25*(77)*	Wet	75 *(10.9)*	69 *(10)*
		71*(160)*	Wet	72 *(10.4)*	-
		91*(195)*	Wet	59 *(8.5)*	-

Bold 93°C *(200°F)* **Bold*** 104°C *(220°F)* **Bold**** 82°C *(180°F)*

HexPly® 8552

Prepreg Properties - HexPly® 8552 Woven Carbon Prepregs (IM7 Fibre)

Physical Properties

	Units	SPG 196-P	SPG 370-8H
Fibre Type	-	IM7 6K	IM7 6K
Fibre density	g/cm³ *(lb/in³)*	1.77 *(0.064)*	1.77 *(0.064)*
Weave	-	Plain	8HS
Mass	g/m² *(oz/yd²)*	196 *(5.78)*	374 *(11.03)*
Weight Ratio, Warp : Fill		50 :50	49 :51
Nominal cured ply thickness @ 37% resin content	mm *(inch)*	0.199 *(0.0078)*	0.380 *(0.0150)*
Nominal Fibre Volume	%	55.57	55.57
Nominal Laminate Density	g/cm³ *(lb/in³)*	1.56 *(0.056)*	1.56 *(0.056)*

Mechanical Properties

Test	Units	Temp°C (°F)	Condition	SPG 196-PW	SPG 370-8H
0°Tensile Strength	MPa *(ksi)*	-55*(-67)*	Dry	979 *(142)*	965 *(140)*
		25*(77)*	Dry	1090 *(158)*	1014 *(147)*
		91*(195)*	Dry	-	-
90°Tensile Strength	MPa *(ksi)*	-55*(-67)*	Dry	862 *(125)*	903 *(131)*
		25*(77)*	Dry	945 *(137)*	959 *(139)*
		93*(200)*	Dry	**979 (142)***	**879 (130)***
0°Tensile Modulus	GPa *(msi)*	-55*(-67)*	Dry	85 *(12.3)*	86 *(12.5)*
		25*(77)*	Dry	85 *(12.3)*	86 *(12.4)*
		91*(195)*	Dry	-	-
90°Tensile Modulus	GPa *(msi)*	-55*(-67)*	Dry	80 *(11.6)*	81 *(11.7)*
		25*(77)*	Dry	80 *(11.6)*	81 *(11.7)*
		93*(200)*	Dry	**79 (11.5)***	**79 (11.5)***
0° ILSS (Shortbeam shear)	MPa *(ksi)*	-55*(-67)*	Dry	-	-
		25*(77)*	Dry	88 *(12.7)*	90 *(13)*
		91*(195)*	Dry	**69 (10)***	**74 (10.8)***
		25*(77)*	Wet	80 *(11.6)*	83 *(12.1)*
		71*(160)*	Wet	**61 (8.8)****	**63 (9.1)****
		91*(195)*	Wet	-	-

Bold 93°C *(200°F)*   Bold* 104°C *(220°F)*   Bold 82°C *(180°F)***

Typical Neat Resin Data

Colour	Yellow	
Density	1.301 g/cc	*(0.0470 lb/in³)*
Glass Transition Temperature, Tg dry	200°C	*(392°F)*
Glass Transistion Temperature, Tg wet	154°C	*(309°F)*
Tensile Strength	121 MPa	*(17.5 ksi)*
Tensile Modulus	4670 MPa	*(0.677 msi)*

Curing Conditions

Cure cycle for monolithic components

1. Apply full vacuum (1 bar).
2. Apply 7 bar gauge autoclave pressure.
3. Reduce the vacuum to a safety value of 0.2 bar when the autoclave pressure reaches approximately 1 bar gauge.
4. Heat at 1- 3°C/min *(2-8°F/min)* to 110°C ± 5°C *(230°F ± 9°F)*
5. Hold at 110°C ± 5°C *(230°F ± 9°F)* for 60 minutes ± 5 minutes.
6. Heat at 1-3°C/min *(2-8°F/min)* to 180°C ± 5°C *(356°F ± 9°F)*
7. Hold at 180°C ± 5°C *(356°F ± 9°F)* for 120 minutes ± 5 minutes.
8. Cool at 2 - 5°C *(4-9°F)* per minute
9. Vent autoclave pressure when the component reaches 60°C *(140°F)* or below.

Cure cycle for honeycomb sandwich components

1. Apply full vacuum (1 bar).
2. Apply 3.2 bar gauge autoclave pressure.
3. Reduce the vacuum to a safety value of 0.2 bar when the autoclave pressure reaches approximately 1 bar gauge.
4. Heat at 1- 3°C/min *(2-8°F/min)* to 110°C ± 5°C *(230°F ± 9°F)*
5. Hold at 110°C ± 5°C *(230°F ± 9°F)* for 60 minutes ± 5 minutes.
6. Heat at 1-3°C/min *(2-8°F/min)* to 180°C ± 5°C *(356°F ± 9°F)*
7. Hold at 180°C ± 5°C *(356°F ± 9°F)* for 120 minutes ± 5 minutes.
8. Cool at 2 - 5°C *(4-9°F)* per minute
9. Vent autoclave pressure when the component reaches 60°C *(140°F)* or below.

Note: For both cure cycles – at each stage, use the temperature shown by the leading thermocouple.

Heat-up rates are dependent on component thickness, eg, slow heat-up rates should be used for thicker components and large tools. Accurate temperature measurements of the component should be made during the cure cycles by using thermocouples.

Performance testing should accompany alternative cure cycles to ensure suitability for the particular application.

Curing Cycle for Honeycomb and Monolithic Components

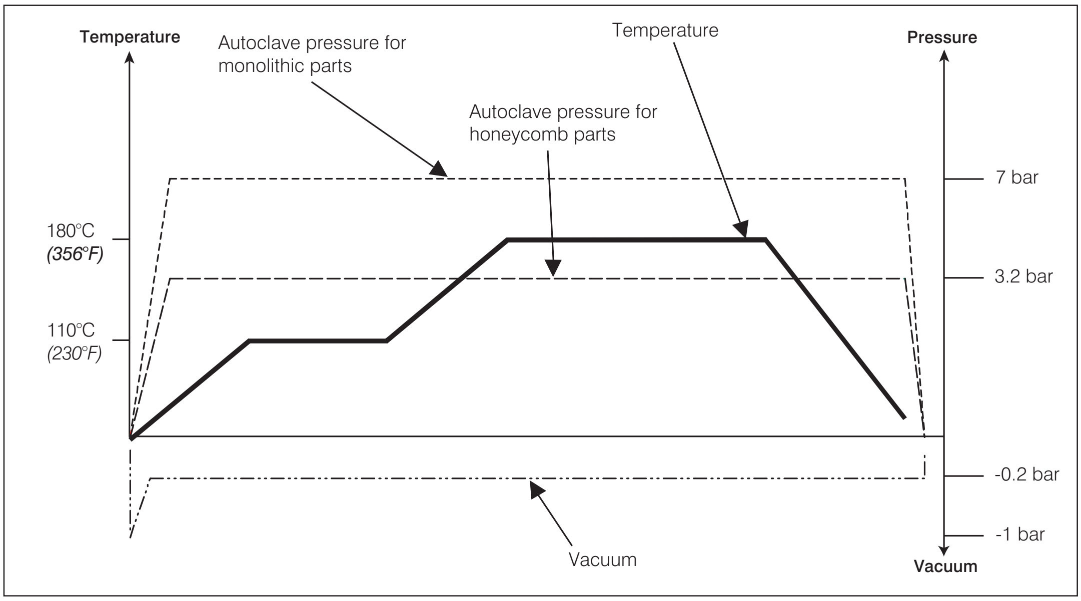

Prepreg Storage Life

Tack Life:	10 days at RT *(23°C/73°F)*
Out Life:	30 days at RT *(23°C/73°F)*
Shelf Life:	12 months at -18°C*(0°F)* (from date of manufacture)

Definitions:

Shelf Life:	The maximum storage life for HexPly® Prepreg, upon receipt by the customer, when stored continuously, in a sealed moisture-proof bag, at -18°C*(0°F)*. To accurately establish the exact expiry date, consult the box label.
Tack Life:	The time, at room temperature, during which prepreg retains enough tack for easy component lay-up.
Out Life:	The maximum accumulated time allowed at room temperature between removal from the freezer and cure.

Precautions for Use

The usual precautions when handling uncured synthetic resins and fine fibrous materials should be observed, and a Safety Data Sheet is available for this product. The use of clean disposable inert gloves provides protection for the operator and avoids contamination of material and components.

Important
All information is believed to be accurate but is given without acceptance of liability. Users should make their own assessment of the suitability of any product for the purposes required. All sales are made subject to our standard terms of sale which include limitations on liability and other important terms.

®Copyright Hexcel Composites
Publication FTA 072e (Feb 2013)

For More Information

Hexcel is a leading worldwide supplier of composite materials to aerospace and other demanding industries. Our comprehensive product range includes:

- Carbon Fibre
- RTM Materials
- Honeycomb Cores
- Carbon, glass, aramid and hybrid prepregs
- HexTOOL® composite tooling material
- Structural Film Adhesives
- Honeycomb Sandwich Panels
- Engineered Core
- Reinforcement Fabrics

For US quotes, orders and product information call toll-free 1-800-688-7734

For other worldwide sales office telephone numbers and a full address list please go to:

http://www.hexcel.com/OurCompany/sales-offices

Appendix C

Preliminary design : Matlab code

This appendix explains the Matlab algorithm used to calculate the axial and bending stiffness of the Fibre Reinforced Polymer (FRP) box beam.

C.1 Matlab algorithm

```matlab
%% Material Properties in MPa

E1 = 1.641e5;
E2 = 1.172e4;
G12 = 5.171e03;
v12 = 0.32;
v21 = E2/E1*v12;

%% Strength Parameters in MPa

Xt = 2723.43;  % Longitudinal Tensile failure load
Xc = 1689.22;  % Longitudinal Compressive failure load
Yt = 111;    % Transverse Tensile failure load
Yc = 222.7007;   % Transverse Compressive failure load
Sh = 119.97;   % Shear failure load

%% Input for box section

num_plies = input('Enter number of plies for web and flange ');
a = input('Enter outside width dimension of box in mm ');
b = input('Enter outside height dimension of box in mm ');
L = input('Enter length of the box section in mm ');
tp = 0.1524; % thickness of ply in mm

total_thickness = tp * num_plies;  %% total thickness of the web and ...
    flange in mm

```

```
a1 = a - 2*total_thickness; % inside box width dimension in mm
b1 = b - 2*total_thickness; % inside box height dimension in mm
```

In this section of the Matlab code, the material properties of Hexcel 8552/IM7 and dimensions of the box beam cross-section are given as input.

```
%% Weight check

rho_steel = 7.6 ; % in gm/cm3
rho_ply = 1.57; % in gm/cm3


%% Current design section dimension

steel_area = 576 ; % in mm2
massperlength_steel = 7.6/1000*10^6*576/10^6; % in kg/m

composite_area = a*b-a1*b1;
massperlength_composite = 1.57/1000*10^6*composite_area/10^6; % in kg/m

if massperlength_composite≥massperlength_steel
h = msgbox(sprintf('There is no weight reduction than Black Aluminum '));
break;
end
```

Subsequently, the mass of the FRP box beam is calculated and compared with the corresponding mass of the steel member. If the mass of the former is greater than the latter, the Matlab code stops and asks the user to input the values of the box beam again.

```
%% Layup for the flange

counter = 1;

if rem(num_plies,2)==0


    fprintf('Input for Skin layup, enter only symmetric half\n');


    for counter=1:num_plies*0.5
        fprintf('Enter %d ply ',counter);
        flange_layup(counter)=input('');
    end


else

        fprintf('Input for  flange layup till mirror \n');

    for counter=1:(num_plies+1)/2
        fprintf('Enter %d ply ',counter);
        flange_layup(counter)=input('');
    end

```

```
end

kill =2;
if rem(num_plies,2)==0
    flange_layup_box=[flange_layup fliplr(flange_layup)];
else
    for j=1:num_plies
        if (j≤(num_plies+1)/2)
            flange_layup_box(1,j) = flange_layup(1,j);
        else
            flange_layup_box(1,j) = flange_layup(1,j-kill);
            kill = kill+2;
        end
    end

end

web_layup_box = flange_layup_box; % Web layup assignment
```

Here, the Matlab code asks the user to input the layup of the flanges. The Matlab code subsequently assigns the same layup for the web.

```
function [ ABD,E_axial,E_bending,Q,tl] = ABDmatrix_calculator( num_plies, ...
    tp , E1, E2,G12,v12,v21,layup )

% Calculation of ABD matrix, axial stiffness and bending stiffness
% Assumption 1 : Plane Stress in each ply
% Assumption 2 : Thick Laminate


%% Stiffness matrix of a ply in the material direction

Q11 = E1/(1-v12*v21);
Q12 = v12*E2/(1-v12*v21);
Q21 = Q12;
Q22 = E2/(1-v12*v21);
Q66 = G12;
Q = [Q11 Q12 0; Q21 Q22 0; 0 0 Q66];

%% Layups and Laminate

tl_total = num_plies*tp; % Total Thickness
tl = zeros(1,num_plies+1);
t = zeros(1,num_plies);

for i = 1:length(tl)
    tl(1,i)= (i-1)*tp-tl_total/2; % Location of the laminae w.r.t midline
end

Laminate = layup;

for i=1:num_plies
    t(1,i) = tp;
end

%% ABD matrix
```

```

A = zeros(3,3);
B = zeros(3,3);
D = zeros(3,3);

for i =1:length(t)
    theta = Laminate(1,i)*pi/180; % Coverting degree to radian
    m = cos(-theta);
    n = sin(-theta);
    M = [m^2 n^2 2*m*n; n^2 m^2 -2*m*n; -m*n m*n m^2-n^2];
    N = [m^2 n^2 m*n; n^2 m^2 -m*n; -2*m*n 2*m*n m^2-n^2];
    Q_theta = M*Q*M';
    A = A + Q_theta*t(i);
    B = B + Q_theta*0.5*((tl(1,i+1))^2-(tl(1,i))^2);
    D = D + Q_theta*1/3*((tl(1,i+1))^3-(tl(1,i))^3);

end
ABD = [A B; B D];
% Aterms = [ABD(1,1) ABD(1,2) ABD(2,2)];
% Dterms = [ABD(4,4) ABD(4,5) ABD(5,5) ABD(6,6)];


%% Modulus Calculation

E_axial = 1/tl_total * (ABD(1,1)-ABD(1,2)^2/ABD(2,2)); % Axial Stiffness
E_bending = 12/tl_total^3 * (ABD(4,4)-ABD(4,5)^2/ABD(5,5)); % Bending ...
    stiffness


end
```

Based on the input layup and cross-section dimensions of the box beam, the ABD matrix of the flange and web are calculated to estimate the axial and bending modulus of the FRP box beam.

```
%% Stiffness Calculation

I_box_x1 = 1/12*(a^3*b - a1^3*b1); % Moment of Inertia in the x1 axis
I_box_y1 = 1/12*(a*b^3 - a1*b1^3); % Moment of Inertia in the y1 axis

A_box = a*b - a1*b1; % Area of the box

Axial_Stiffness = E_axial_flange_box*A_box;
Bending_Stiffness_x1 = E_bending_flange_box*I_box_x1; % in x1 axis
Bending_Stiffness_y1 = E_bending_flange_box*I_box_y1; %in y1 axis
```

Finally, the axial and bending stiffness are calculated for the FRP box beam.

Appendix D

Composite Telescoping boom (T-boom) design

This appendix describes the cross-section details of the composite T-boom, and, calculates the membrane and bending stiffness of the chords and bracings.

D.1 Composite T-boom drawing

The drawing of the composite T-boom is in third angle projection.

D.2 Cross-section details of the composite T-boom

The cross-section details of members 1,3,4,5 and 6 are shown in Figure D.1,

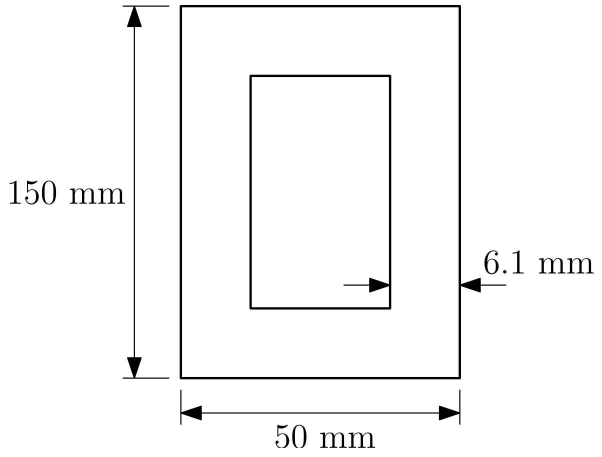

Figure D.1: Cross-section details of member 1,3,4,5 and 6

The membrane and bending modulus of the members are 82.3 GPa and 103.4 GPa respectively, shown in Table 4.4.

- Area of member, $A_{box} = 2291.16$ mm^2
- Moment of inertia of member along x$_1$ axis, $I_{box,x1} = \frac{1}{12} \cdot \left(50 \cdot 150^3 - 37.8 \cdot 137.8^3\right) = 5.82 \cdot 10^6$ mm^4
- Moment of inertia of member along y$_1$ axis, $I_{box,y1} = \frac{1}{12} \cdot \left(50^3 \cdot 150 - 37.8^3 \cdot 137.8\right) = 9.42 \cdot 10^5$ mm^4
- Axial stiffness of member, $E_{1m}A_{box} = 1.89 \cdot 10^8$ N
- Bending stiffness of member along x$_1$ axis, $E_{1b}I_{box,x1} = 6.02 \cdot 10^{11}$ N·mm^2
- Bending stiffness of member 1 along y$_1$ axis, $E_{1b}I_{box,y1} = 9.74 \cdot 10^{10}$ N·mm^2

The cross-section details of member 2 is shown in Figure D.2,

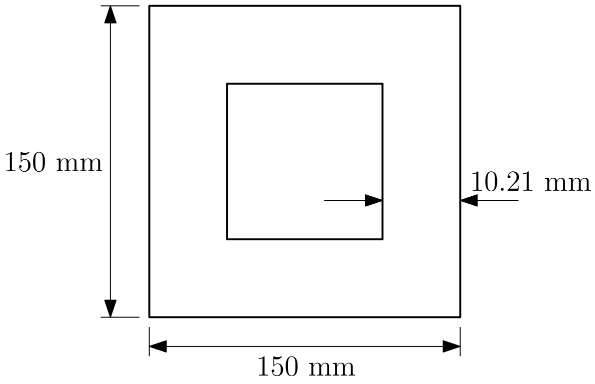

Figure D.2: Cross-section details of member 2

The membrane and bending modulus of the members are 76.52 GPa and 82.57 GPa respectively, shown in Table 4.4.

- Area of member, $A_{box} = 5709.02$ mm^2
- Moment of inertia of member along x$_1$ axis, $I_{box,x1} = \frac{1}{12} \cdot \left(150^4 - 129.58^4\right) = 1.87 \cdot 10^8$ mm^4
- Moment of inertia of member along y$_1$ axis, $I_{box,y1} = 1.87 \cdot 10^8$ mm^4
- Axial stiffness of member, $E_{1m}A_{box} = 4.4 \cdot 10^8$ N
- Bending stiffness of member along x$_1$ axis, $E_{1b}I_{box,x1} = 1.54 \cdot 10^{12}$ N·mm^2
- Bending stiffness of member 1 along y$_1$ axis, $E_{1b}I_{box,y1} = 1.54 \cdot 10^{12}$ N·mm^2

D.3 Bending stiffness of the composite T-boom

Figure D.3 shows the cross-section of the composite T-boom considered for the bending stiffness calculation.

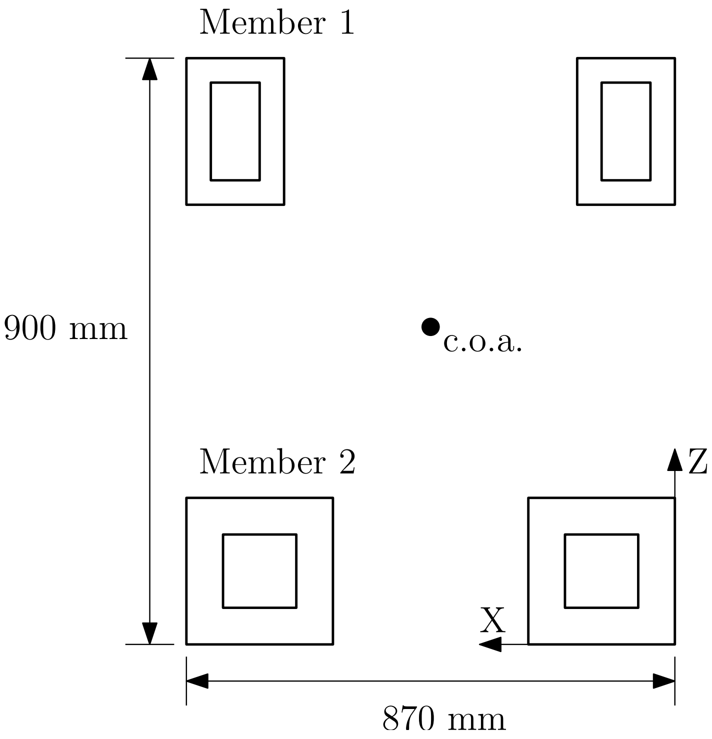

Figure D.3: Cross-section of the composite T-boom for bending stiffness calculation

The centre of area (c.o.a.) of the cross-section in the x and z direction is given by Eq. (D.1) and Eq. (D.2) respectively.

$$x_{coa} = \frac{(25 \cdot 2291.16 + 75 \cdot 5709.02 + 795 \cdot 5709.02 + 845 \cdot 2291.16)}{2 \cdot (2291.16 + 5709.02)} = 435\ mm \tag{D.1}$$

$$z_{coa} = \frac{(825 \cdot 2291.16 + 75 \cdot 5709.02 + 75 \cdot 5709.02 + 825 \cdot 2291.16)}{2 \cdot (2291.16 + 5709.02)} = 289.7914\ mm \tag{D.2}$$

The moment of inertia of the members about the c.o.a. is given from Eq. (D.3) to Eq. (D.6).

For member 1,

$$I_{1,coa,x} = 5.82 \cdot 10^6 + 2291.16 \cdot (825 - 289.7914)^2 = 6.62 \cdot 10^8\ mm^4 \tag{D.3}$$

$$I_{1,coa,z} = 9.42 \cdot 10^5 + 2291.16 \cdot (435 - 25)^2 = 3.86 \cdot 10^8\ mm^4 \tag{D.4}$$

For member 2,

$$I_{2,coa,x} = 1.87 \cdot 10^8 + 5709.02 \cdot (289.7914 - 75)^2 = 4.504 \cdot 10^8\ mm^4 \tag{D.5}$$

$$I_{2,coa,z} = 1.87 \cdot 10^8 + 5709.02 \cdot (435 - 75)^2 = 9.27 \cdot 10^8 \ mm^4 \tag{D.6}$$

Finally, the bending stiffness of the cross-section in the x and z axis is given by Eq. (D.7) and Eq. (D.8) respectively.

$$EI_{Tboom,x} = 2.13 \cdot 10^{14} \ N \cdot mm^2 \tag{D.7}$$

$$EI_{Tboom,z} = 2.33 \cdot 10^{14} \ N \cdot mm^2 \tag{D.8}$$

Appendix E

Verification of the shell model

This chapter discusses the deflection results obtained for a cantilever Fibre Reinforced Polymer (FRP) beam using shell elements with the values available in literature.

E.1 Beam model

As discussed in Section 3.2, S4R elements are used to model the FRP box beam and the deflection is compared with results published by Bank and Bednarczyk [53]. The dimensions of the box beam are shown in Table E.1.

Table E.1: Box beam dimensions

Parameter	Value
a_{box}	100
b_{box}	25
t_{box}	1
L_{box}	1000

The composite material system used to model the FRP beam is graphite/epoxy T300/5208 and the material properties are shown in Table E.2.

Table E.2: Graphite/epoxy T300/5208 properties [53]

Parameter	Value
E_1	181
E_2	13
G_{12}	7.17
ν_{12}	0.28

where E_1 is the tensile modulus of the ply in the fibre direction (GPa) , E_2 is the tensile modulus of the ply perpendicular to the fibre direction (GPa), G_{12} is the shear modulus of the ply (GPa) and ν_{12} is the Poisson's ratio of the ply.

The box beam is modelled in ABAQUS by Three Dimensional (3-D) shell extrusion and meshed using S4R elements of global mesh size = 5 mm. In the analysis, the layup of the FRP beam is unidirectional. The Finite Element (FE) model of the FRP box beam is shown in Figure E.1.

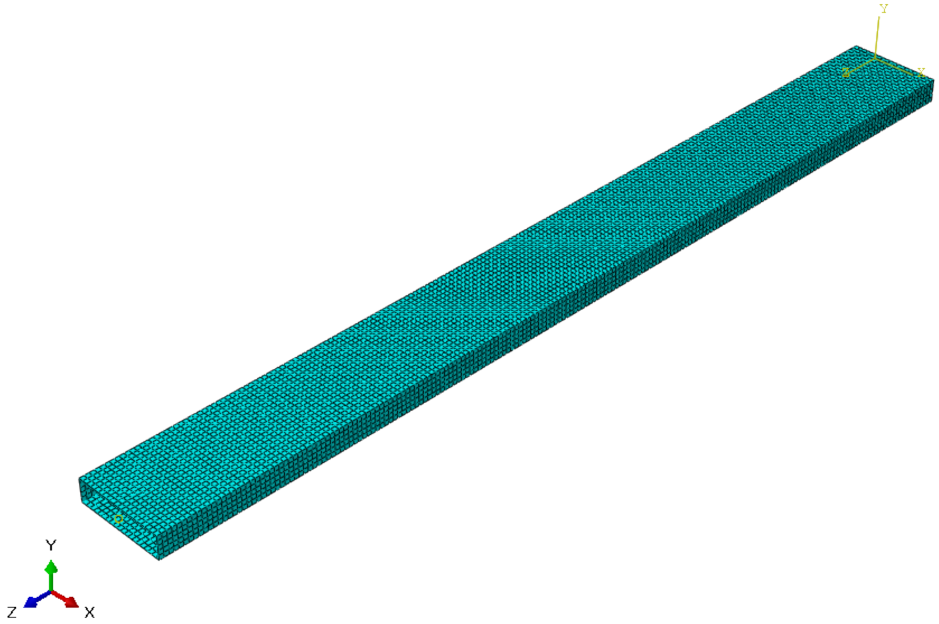

Figure E.1: FE model of the FRP box beam of mesh size = 5 mm

A load of 100 N is applied at the centre of mass of the box cross-section at one end while the other end is clamped.

E.2 Displacement results and conclusion

The maximum vertical displacement of the tip point lying on the neutral axis at the load application end is 6.286 mm. Table E.3 compares the FE result with the analytical solution published for a tip loaded cantilever box beam by Bank and Bednarczyk [53].

Table E.3: Displacement results comparison between FE and analytical model

FE solution	Analytical solution [53]	% error
6.286	6.034	4.2

Figure E.2 shows the displacements results of the FRP box beam subjected to a tip load and clamped support.

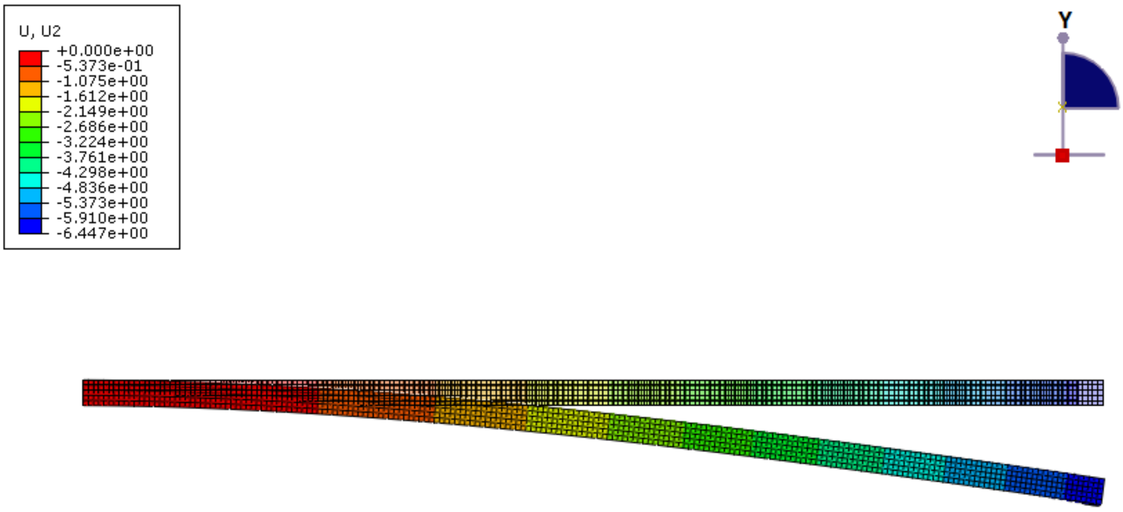
U, U2
+0.000e+00
-5.373e-01
-1.075e+00
-1.612e+00
-2.149e+00
-2.686e+00
-3.224e+00
-3.761e+00
-4.298e+00
-4.836e+00
-5.373e+00
-5.910e+00
-6.447e+00
Y

Figure E.2: Vertical displacement result of the FRP box beam

The maximum tip displacement at the same point on the neutral axis is 6.26 mm for S8R elements. Hence, the solution accuracy did not significantly improve by shifting to S8R elements, although, the model became computationally expensive. It can be concluded that S4R shell element predicts the response of the FRP box beam with reasonable accuracy without much computational effort. Hence, S4R element is used to model the composite Telescoping boom (T-boom) for FE analysis. An important observation from the analysis is that the load application location has a significant influence on the displacement results, and, the stress concentration locations. Hence, sound engineering judgement is essential before neglecting the stress raiser locations.

Appendix F

Load cases for the Finite Element (FE) model

This appendix summarizes the calculation procedure to estimate the shear forces and bending moments acting at the Telescoping boom (T-boom) section used for the FE analysis.

F.1 Introduction

As in Section 3.2, the shear force and bending moments are evaluated only for the worst load cases which are Emergency Operation- 3 People Transfer (EO-3PT), Emergency Operation-Extra Length + Cargo (EO-ELC) and Stowed Condition (SC). The mass and length of the remaining section of the T-boom are 306.037 kg and 7885 mm respectively. The remaining section of the T-boom is shown in Figure F.1.

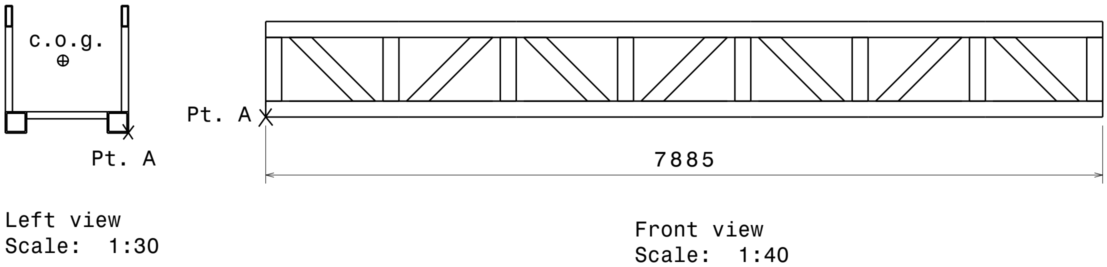

Figure F.1: Remaining section of the T-boom

The centre of gravity (c.o.g.) of the remaining section is estimated with respect to Pt. A, shown in Figure F.1, in Catia and is given by Eq. (F.1).

$$(x, y, z)_{c.o.g.} = (-435, 3942.5, 309.7) \tag{F.1}$$

As mentioned in Section 2.2, the load cases for the T-boom are defined in Table 2.2 and its design is based on Eq. (2.1).

F.2 EO-3PT

For this load case,

- $F_d = 1$ and F_h=1.15
- Live mass accounting F_d and F_h, $m_{live} = F_d \cdot F_h \cdot 300 = 345$ kg
- Dead mass accounting F_d, $m_{dead} = F_d \cdot 306$= 306 kg
- Tip mass accounting F_d, $m_{tip} = F_d \cdot 182$= 182 kg
- Wind speed, $v_{wind} = 20$ m/s

It is assumed that the personnel are standing at the tip of the gangway. Hence, the distance between the FE section and the personnel is the sum of the length of the remaining section of the T-boom and tip, and, is given by 8985 mm.

The total accelerations in m/s^2 for the load case are shown in Table F.1

Table F.1: Total accelerations for EO-3PT

	a_x	a_y	a_z
Gravity	0	0	-9.81
Ship to Ship (S2S) acceleration	0	-1.21	-1.14
Residual acceleration	-0.5	-0.5	-0.5
Total acceleration	-0.5	-1.71	-11.45

The shear forces and bending moments due to live mass are shown in Table F.2.

Table F.2: Shear forces and bending moments due to live mass for EO-3PT

	Unit	EO-3PT
SF_x	N	345×-0.5 = -172.5
SF_y	N	345×-1.71 = -590
SF_z	N	345×-11.45 = -3,950.3
BM_x	N·mm	-3950.3×8985= -3.55×10^7
BM_z	N·mm	172.5×8985= 1.55×10^6

The shear forces and bending moments due to slewing and telescopping are shown in Table F.3.

Table F.3: Shear forces and bending moments due to slewing and telescopping for EO-3PT

	Unit	EO-3PT
SF_x	N	-10^3
SF_y	N	-10^4
SF_z	N	-10^3
BM_x	N·mm	$-1000\times8985= -8.99\times10^6$
BM_z	N·mm	$1000\times8985= 8.99\times10^6$

The shear forces and bending moments due to self-weight of the remaining section are shown in Table F.4.

Table F.4: Shear forces and bending moments due to self-weight for EO-3PT

	Unit	EO-3PT
SF_x	N	$-306\times0.5 = -153$
SF_y	N	$-306\times1.71 = -523.3$
SF_z	N	$-306\times11.45 = -3504$
BM_x	N·mm	$-3504\times3942.5 = -1.38\times10^7$
BM_z	N·mm	$153\times3942.5 = 6.04\times10^5$

The shear forces and bending moments due to tip weight of the remaining section are shown in Table F.5.

Table F.5: Shear forces and bending moments due to tip weight for EO-3PT

	Unit	EO-3PT
SF_x	N	$-182\times0.5 = -91$
SF_y	N	$-182\times1.71 = -311.2$
SF_z	N	$-182\times11.45 = -2.08\times10^3$
BM_x	N·mm	$-2080\times8435 = -1.76\times10^7$
BM_z	N·mm	$91\times8435 = 7.68\times10^5$

The wind loads are estimated based on a set guidelines defined by CLAME [7].

The pressure due to wind load is given by, $p_{wind} = 0.613\times\ v_{wind}^2 = 245.2\ \mathrm{N/m^2}$

The members exposed to the wind are Members 1, 2, 3 and 4. The force coefficients, C_f, for the truss members are shown in Table F.6.

Table F.6: Force coefficients of the truss members

	C_f
Member 1	2.26
Member 2	1.97
Member 3	1.79
Member 4	1.79

The wind load in N on the member is given by Eq. (F.2).

$$F_{wind} = A \times C_f \times p_{wind} \times \left(\frac{1-\eta^n}{1-\eta}\right) \tag{F.2}$$

where A is the area of the truss member exposed to the wind, n is the number of truss members, η is the shielding factor which is 0.145 in this case. The value of C_f and η are defined for different cross-sections in CLAME [7]. The force on the members are shown in Table F.7.

Table F.7: Wind loads on the truss members

	F_{wind}
Member 1	656.12
Member 2	571.93
Member 3	41.62
Member 4	58.67

Shear forces and bending moments of the total wind load are shown in Table F.8. The centre of area (c.o.a.) of the truss members exposed to wind load is obtained from Catia and is given by (0, 3942.5, 450) mm.

Table F.8: Shear forces and bending moments due to wind load for EO-3PT

	Unit	EO-3PT
SF_x	N	-2.01×10^3
BM_z	N·mm	$2010\times3942.5 = 7.93\times10^6$

F.3 EO-ELC

For this load case,

- $F_d = 1.2$ and F_h=1.15
- Live mass accounting F_d and F_h, $m_{live} = F_d \cdot F_h \cdot 200 = 276$ kg
- Dead mass accounting F_d, $m_{dead} = F_d \cdot 306.037$= 367.2 kg

- Tip mass accounting F_d, $m_{tip} = F_d \cdot 182$= 218.4 kg
- Wind speed, $v_{wind} = 20$ m/s

The total accelerations in m/s^2 for the load case is given by Table F.9

Table F.9: Total accelerations for EO-ELC

	a$_x$	a$_y$	a$_z$
Gravity	0	0	-9.81
Slewing acceleration	-0.6	0	0
Residual acceleration	-0.5	-0.5	-0.5
Total acceleration	-1.1	-0.5	-10.31

The shear forces and bending moments due to live mass are shown in Table F.10.

Table F.10: Shear forces and bending moments due to live mass for EO-ELC

	Unit	EO-ELC
SF_x	N	276×-1.1 = -303.6
SF_y	N	276×-0.5 = -138
SF_z	N	276×-10.31 = -2.85×10^3
BM_x	N·mm	-2850×8985= -2.56×10^7
BM_z	N·mm	303.6×8985= 2.73×10^6

The shear forces and bending moments due to self-weight of the remaining section are shown in Table F.11.

Table F.11: Shear forces and bending moments due to self-weight for EO-ELC

	Unit	EO-3PT
SF_x	N	-367.2×1.1 = -404
SF_y	N	-367.2×0.5 = -184
SF_z	N	-367.2×10.31 = -3.79×10^3
BM_x	N·mm	-3790×3942.5 = -1.49×10^7
BM_z	N·mm	404×3942.5 = -1.59×10^6

The shear forces and bending moments due to tip weight of the remaining section are shown in Table F.12.

Table F.12: Shear forces and bending moments due to tip weight for EO-ELC

	Unit	EO-ELC
SF_x	N	-218.4×1.1 = -240
SF_y	N	-218.4×0.5=-109
SF_z	N	-218.4×10.31 = -2.25×10^3
BM_x	N·mm	-2250×8435 = -1.90×10^7
BM_z	N·mm	240×8435 = 2.03×10^6

Shear forces and bending moments of the total wind load for EO-ELC are same as EO-3PT and are shown in Table F.8.

F.4 SC

For this load case,

- $F_d = 1$ and F_h= 1
- Live mass accounting F_d and F_h, $m_{live} = F_d \cdot F_h \cdot 200 = 0$ kg
- Dead mass accounting F_d, $m_{dead} = F_d \cdot 306.037$= 306 kg
- Tip mass accounting F_d, $m_{tip} = F_d \cdot 182$= 182 kg
- Wind speed, $v_{wind} = 63$ m/s

The total accelerations in m/s^2 for the load case is shown in Table F.13

Table F.13: Total accelerations for SC

	a_x	a_y	a_z
Gravity	0	0	-9.81
Acceleration	0	-4.91	-9.81
Total acceleration	0	-4.91	-19.62

The shear forces and bending moments due to reaction forces at the tip are shown in Table F.14.

Table F.14: Shear forces and bending moments due to reaction forces at tip for SC

	Unit	SC
SF_x	N	4.96×10^4
SF_y	N	5.05×10^3
SF_z	N	2.02×10^3
BM_x	N·mm	1.81×10^8
BM_z	N·mm	-4.45×10^8

The shear forces and bending moments due to self-weight of the remaining section are shown in Table F.15.

Table F.15: Shear forces and bending moments due to self-weight for SC

	Unit	SC
SF_x	N	0
SF_y	N	$-306\times4.91 = -1.51\times10^3$
SF_z	N	$-306\times19.62 = -6.02\times10^3$
BM_x	N·mm	$-6020\times3942.5 = -2.37\times10^7$

The shear forces and bending moments due to tip weight of the remaining section are shown in Table F.16.

Table F.16: Shear forces and bending moments due to tip weight for SC

	Unit	SC
SF_x	N	0
SF_y	N	$-182\times4.91=-894$
SF_z	N	$-182\times19.62 = -3571$
BM_x	N·mm	$-3571\times8435 = -3.01\times10^7$

Shear forces and bending moments of the total wind load for the SC are shown in Table F.17.

Table F.17: Shear forces and bending moments due to wind load for SC

	Unit	SC
SF_x	N	-1.96×10^4
BM_z	N·mm	$1.96\times10^4 \times3942.5 = 7.71\times10^7$

Appendix G

Experimental setup

This appendix describes the experimental procedure used to manufacture and test the coupons to determine the moisture absorption properties and static strength.

G.1 Manufacturing of coupons

The coupons for testing are manufactured by the autoclave technique. The step by step procedure to manufacture the coupons are described below.

1. The carbon fibre-epoxy prepreg in the form of rolls, are cut to a dimension of 450×450 mm using the Gerber cutting machine.
2. The bottom baseplate is placed on the workbench and a sandpaper is used to clean its edges and corners. Subsequently, PFQD, a cleaning agent, is used to clean it.
3. A yellow seal tape, of type AT-200 Y and a maximum temperature of 204°C, is pasted along the edges of the bottom base plate in a way that the tape overlaps at the corners.
4. A reinforcement Teflon release foil, of type Bisca Texa 25-500 and a maximum temperature of 280°C, is pasted on the base plate using a blue tape of maximum temperature of 204°C.
5. The topmost ply of the laminate is placed on the release foil with the backing paper side facing upwards. In this case, the topmost ply of the laminate is a 0° ply.
6. Carefully peel away the backing paper, and, assemble the remaining plies onto the first ply in a similar method mentioned in Step 5. To avoid resin surplus areas, it is important to ensure that there is an intimate contact between the plies and the base plate. The final layup of the laminate used for testing is $[0_3, (45/-45)_2, 90_2]s$.

7. A rectangular plate of dimensions 450×450×2 mm is wrapped with the same release foil layer, and, placed on the laminate. This procedure is carried out to ensure even heating of the laminate from the top and the bottom.

8. A breeder blanket/ breather, of type Air weave N10 and a maximum temperature of 204°C, is placed on top of the mould in such a way that it covers the entire laminate. The breeder blanket is subsequently pasted onto the bottombase plate using a blue tape of maximum temperature of 204°C. .

9. A vacuum bag, of type WL 7400 and a maximum temperature of 204°, is cut and placed on the base plate. A vacuum valve is positioned on the breather near the laminate, and, a circular hole is cut on the vacuum foil to allow the threaded part of the valve to pass through it. The purpose of using a vacuum valve is to connect the vacuum bag to the vacuum pump.

10. The tacky tape film is removed and the vacuum foil is placed on the base plate so that it sticks to the tacky tape. It should be ensured that the corners are airtight, and, there are no leaks.

11. A vacuum pump is subsequently connected to the vacuum valve, and, a full vacuum is applied to check for leaks.

12. The laminate is subsequently cured inside an autoclave, and, the curing cycle applied on the laminate is shown in Appendix B.

13. The manufactured laminate is checked for defects in a C-scan. If there are any defects in the laminate, the defective regions are cut-off, and, not used for testing.

14. The laminate is cut using the carat wet diamond cutter and proth cutting-grinding machines to produce the moisture, tensile and compression coupons of the required dimensions.

The detailed procedure to manufacture the laminate in autoclave is available in Hexcel website. Figure G.1 shows the C-scan results of the manufactured laminate, and, Figure G.2 shows few illustrations depicting the methodology to manufacture the coupons.

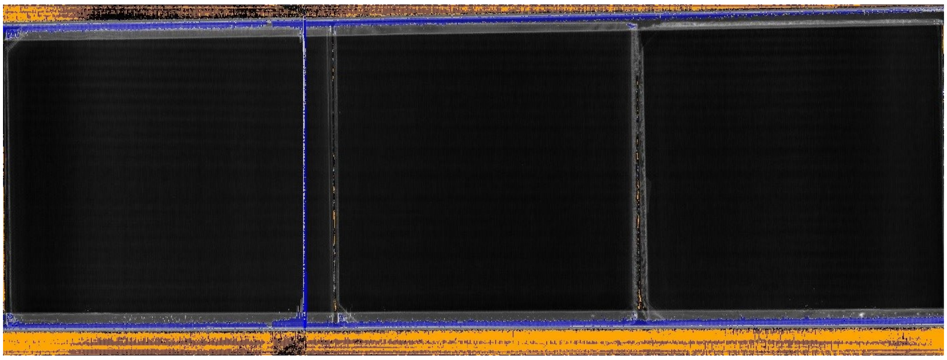

Figure G.1: C-scan results

Based on Figure G.1, it can be concluded that there are no defects in the manufactured laminate.

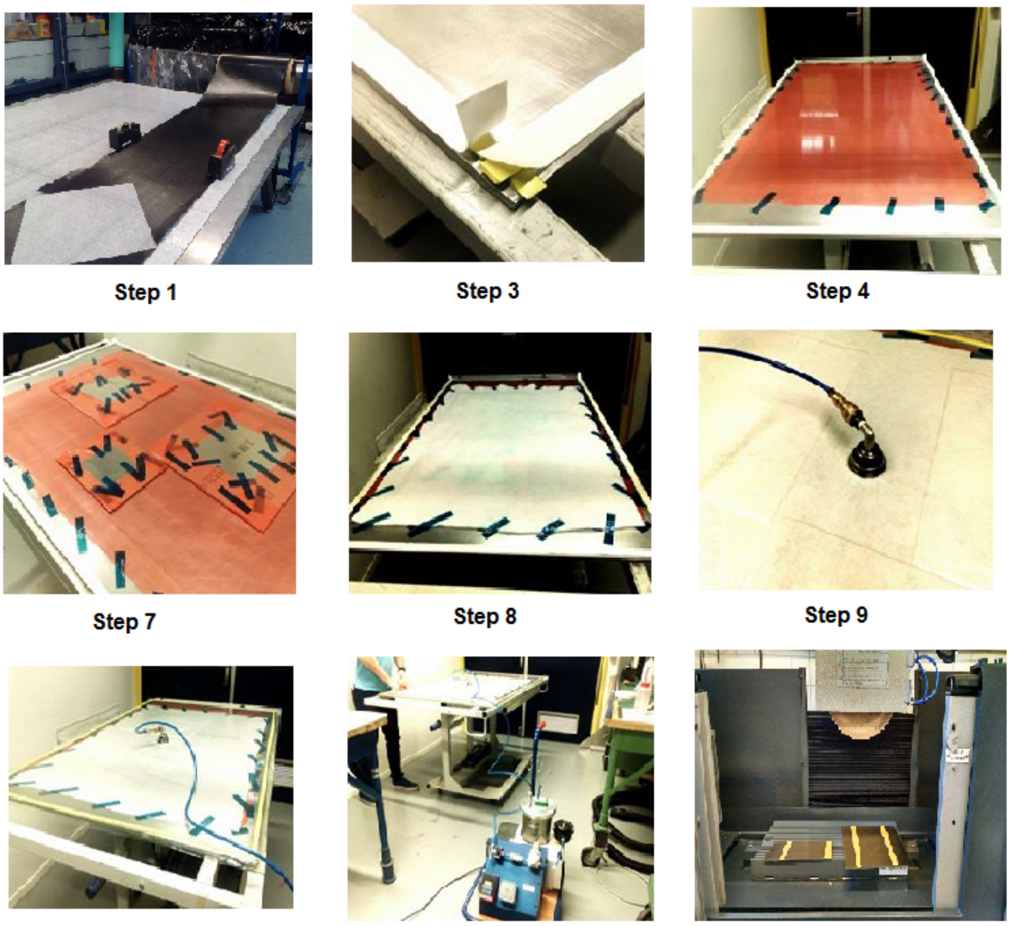

Step 1 Step 3 Step 4

Step 7 Step 8 Step 9

Step 9 Step 11 Step 14

Figure G.2: Illustrations depicting the methodology to manufacture the coupons

G.2 Preconditioning of the specimens

The coupons are pre-conditioned at 90% Relative Humidity (R.H.) and 55°C for a period of 8 weeks in a climate chamber. The purposes for pre-conditioning the specimens are two folds:

- Firstly, to determine the moisture absorption properties of the coupons and,
- finally, to determine the tensile and compressive properties of the coupons sat different preconditioning periods

The moisture absorption properties are determined based on the ASTM D 5229/D 5229M —92 standard. The number of coupons tested for each preconditioning period are shown in Table 3.10 and the dimensions of the coupons are shown in Table 3.11.

G.3 Static strength tests

As discussed in Section 3.4, the static tension and compression properties of the coupons at different preconditioning periods: 0,15,30 and 60 days, are determined by testing them on the Zwick 250 kN machine.

G.3.1 Tension test

The tensile test of the coupons are performed based on the ASTM D 3039/D 3039M standard. Zwick 250 kN machine equipped with hydraulic clamps is used to test the coupons where the force-strain data are determined by using an extensiometer and a strain gauge. The extensiometer used during the testing is able to measure the strain only in the longitudinal direction. Paper tabs of dimensions 50×25×1.5 mm are bonded at the ends, to ensure proper gripping and load introduction into the coupons. Figure G.3 shows an illustration of a tensile coupon used for testing. The dimensions of a tensile test coupon are shown in Table 3.12.

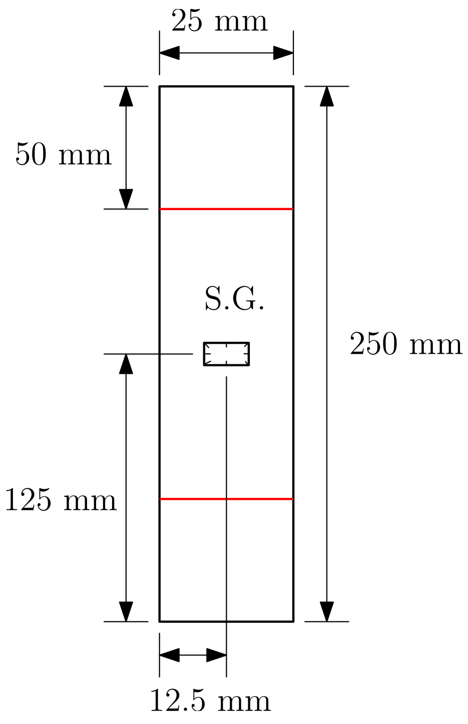

Figure G.3: Illustration of a tensile coupon

The strain gauge, S.G., used for the tensile testing is from the company, Micro-Measurements, with gage factor of 2.14. It is bonded in the transverse direction, shown in Figure G.3. The number of tensile coupons tested for each preconditioning period is shown in Table 3.10. Figure G.4 shows the experimental setup used for tension testing.

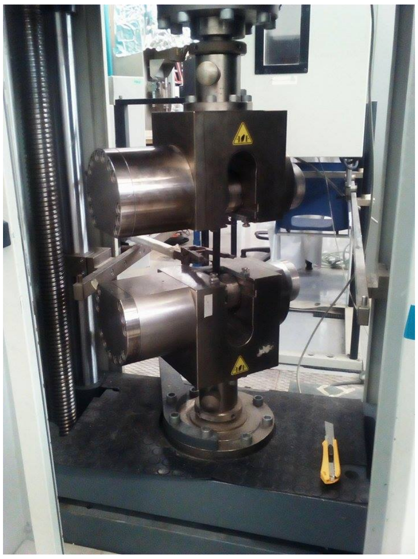

Figure G.4: Tension test setup

G.3.2 Compression test

The compression test of the coupons are performed based on the ASTM D 6641/D 6641M standard. The coupon is mounted on a Combined Loading Compression (CLC) fixture, and, a compression load is applied on the it to measure the force versus crosshead displacement. No tabs are used for the compression coupons. Figure G.5 shows an illustration of a tensile coupon used for testing. The dimensions of a compression test coupon are shown in Table 3.12.

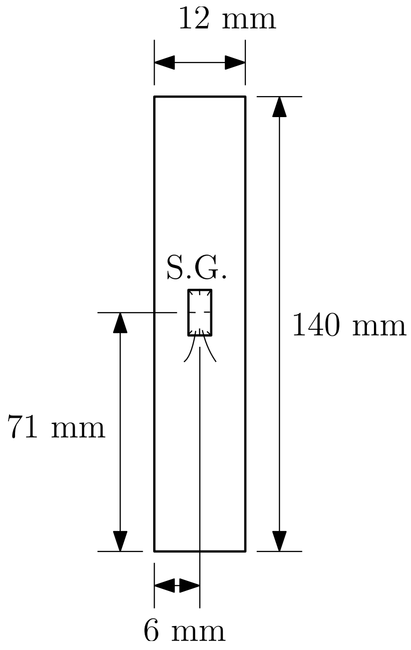

Figure G.5: Illustration of a compression coupon

The strain gauge, S.G., used for the compression testing is from the company, Kyowa Electronic Instruments, with gage length of 2 mm and gage factor of 2.09. It is bonded in the longitudinal direction, shown in Figure G.5. The number of compression coupons tested for each preconditioning period is shown in Table 3.10. Figure G.6 shows the CLC fixture used for the compression testing of the coupons.

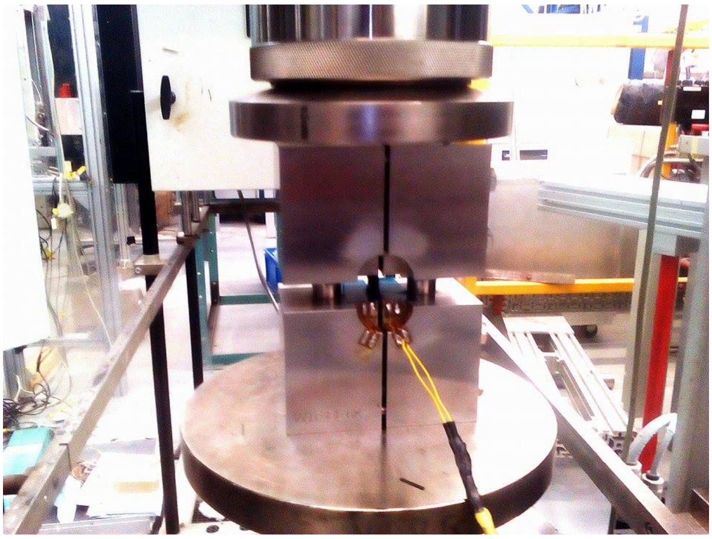

Figure G.6: CLC fixture for the compression test

G.4 Experimental results

The experimental results for the moisture ingression, tensile and compressions tests are discussed in this section.

G.4.1 Moisture ingression tests data for the Hexply 8552/AS4 laminate

Table G.1 shows the mass of the coupons in mg measured every 7 days for a period of 8 weeks during the moisture ingression tests.

Table G.1: Mass of the coupons in mg for different preconditioning periods

Week	MC1	MC2	MC3	MC4	MC5	MC6
0	7288.7	7252.3	7438.1	7614.2	7179.1	7337
1	7310.4	7274.2	7460.8	7637.3	7200.4	7359.9
2	7319.9	7284.1	7470.7	7647.4	7209.1	7369.7
3	7328.4	7290.4	7478.3	7656.8	7218	7376.8
4	7335.3	7298.2	7484.6	7663.8	7223	7383.1
5	7340.6	7304.2	7491.3	7668.6	7229.2	7389.5
6	7344.9	7308.6	7496.7	7673.6	7232.9	7394.3
7	7349.5	7313.5	7499	7677.6	7237.2	7399
8	7350.7	7315	7500.9	7680.6	7240.7	7400.9

MCi corresponds to the ith moisture coupon in Table G.1.

G.4.2 Tension test results

Table G.2 shows the tension strength results in MPa for the Hexply 8552/AS4 laminate preconditioned for 0, 10, 25 and 55 days.

Table G.2: Tension strength results in MPa for the Hexply 8552/AS4 laminate for different preconditioning periods

Coupon	W1	W2	W3	W4
1	934	976	941	957
2	1018	979	1005	898
3	1001	936	877	922
4	988	960	930	934
5	1007	877	955	903
6	-	1009	857	949
7	-	-	946	957

Due to wrong equipment setting, the 6th and 7th coupons of W1, and, 7th coupon of W2 failed prematurely, and, are not considered for subsequent analysis.

G.4.3 Compression test results for the Hexply 8552/AS4 laminate

Table G.3 shows the compression strength results in MPa for the Hexply 8552/AS4 laminate preconditioned for 0, 10, 25 and 55 days.

Table G.3: Compression strength results in MPa for the Hexply 8552/AS4 laminate for different preconditioning periods

Coupon	W1	W2	W3	W4
1	518	504	504	470
2	521	509	497	456
3	524	485	451	481
4	512	508	488	493
5	540	495	479	479
6	545	535	491	480
7	524	496	456	471

G.4.4 Static strength results for the Hexply 8552/IM7 laminate

Table G.4 shows the static strength results in MPa for the Hexply 8552/IM7 laminate used to plot the ideal S-N curves using the Kassapoglou's model.

Table G.4: Static strength results in MPa for the Hexply 8552/IM7 laminate

Coupon	Tension	Compression
1	1204	567
2	1148	479
3	978	512
4	1059	481
5	1136	507
6	1047	499
7	-	388

Due to user error, the 7^{th} coupon for tension test failed prematurely, and, is not considered for subsequent analysis.

Appendix H

Statistical tests

This appendix describes the statistical methods used to perform data pooling. The detailed explanation of the statistical test methods along with examples can be found in military handbook MIL-HDBK-17-1F [40].

H.1 2-parameter Weibull distribution

A 2-parameter Weibull distribution is described by α and β, and, its probability density and cumulative distribution functions are given by Eq. (H.1) and Eq. (H.2) respectively.

$$pdf = \begin{cases} \frac{\alpha}{\beta} \cdot \left(\frac{x}{\beta}\right)^{\alpha-1} \cdot \mathrm{e}^{-(x/\beta)^{\alpha}} & \text{if } x \geq 0 \\ 0 & \text{if } x < 0 \end{cases} \tag{H.1}$$

$$cdf = 1 - \mathrm{e}^{-(x/\beta)^{\alpha}} \tag{H.2}$$

Scale parameter, β corresponds to 63.2 percentile of the data. So, if β is 520 MPa for the tensile strength, it means that 63.2% of the coupons will fail within 520 MPa during tensile testing. Shape parameter, α corresponds to the distribution of the data. For example, if there is a high variation in strength data for a compression test, the shape parameter will be low. This implies that the strength values are distributed/scattered, and, cant be represented by a single strength value. Figure H.1 shows the effect of the scale parameter for the same shape parameter, and, Figure H.2 shows the effect of the shape parameter for the same scale parameter of the Weibull distribution to the right.

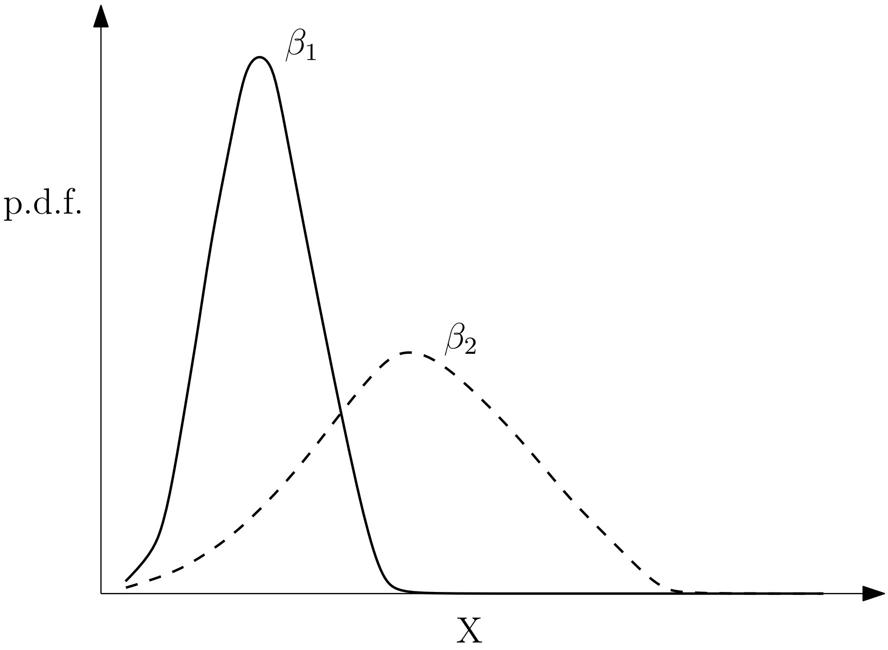

Figure H.1: Effect of scale parameter for the Weibull distribution

The scale parameter defines the Weibull distribution curve position relative to the threshold value. As seen in Figure H.1, for the same α, when $\beta_2 > \beta_1$, the threshold value shifts to the right for the former which subsequently shifts the Weibull curve.

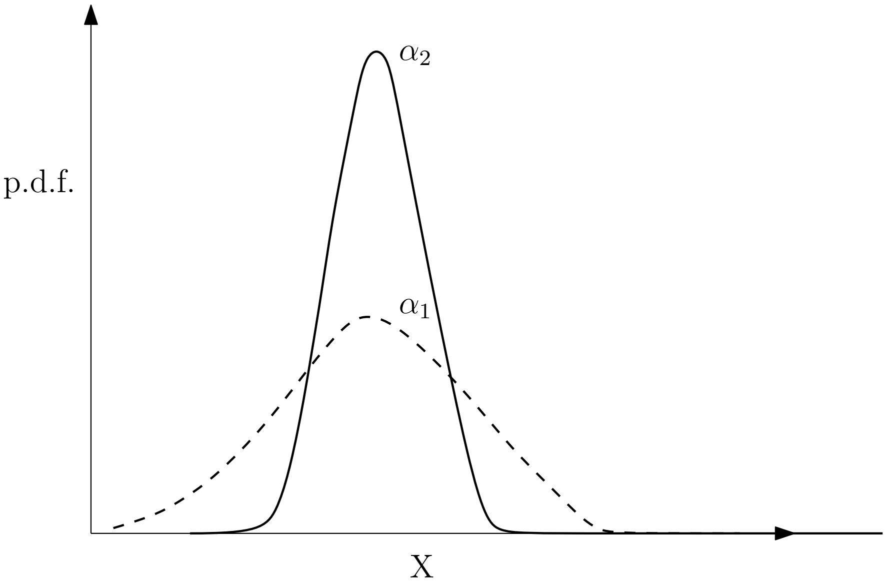

Figure H.2: Effect of shape parameter for the Weibull distribution

As seen in Figure H.2, for the same β, when $\alpha_1 < \alpha_2$, the data is more distributed and scattered for the former.

H.2 k-sample Anderson-Darling test

The k-sample Anderson-Darling test is a statistical procedure used to check if the data drawn from different populations are identical. Let x_{ij} denote the data where i corresponds to the group and j corresponds to the observation within that group. If there are n_i data values within the i^{th} of k groups, the total number of observation is given by Eq. (H.3).

$$n_{obs} = n_1 + n_2 + ... + n_k \tag{H.3}$$

Let z_1, z_2,...,z_L correspond to distinct data values in the combined set of data sorted in the ascending order. Here, L is less than n if there are same observations in different groups. Hence, the k-sample Anderson-Darling statistic is given by (H.4).

$$ADK = \frac{n_{obs}-1}{n_{obs}^2\left(k-1\right)}\sum_{i=1}^{k}\left[\frac{1}{n_i}\cdot\sum_{j=1}^{L}h_j\cdot\frac{\left(n_{obs}\cdot F_{ij}-n_i\cdot H_j\right)^2}{H_j\cdot\left(n_{obs}-H_j\right)-n_{obs}\cdot h_j/4}\right] \tag{H.4}$$

where h_j is the number of values in the combined data set equal to z_j, H_j is the number of values in the combined data less than z_j plus half of the number of values in the combined data set equal to z_j, and, F_{ij} is the number of values in the i^{th} group which are less than z_j plus half of the number of values in this group which are equal to z_j.

The variance and mean of ADK are approximately equal to 1 if there is no difference in the populations. The variance of the ADK is given by Eq. (H.5).

$$\sigma_n^2 = Var\left(ADK\right) = \frac{a\cdot n_{obs}^3 + b\cdot n_{obs}^2 + c\cdot n_{obs} + d}{\left(n_{obs}-1\right)\left(n_{obs}-2\right)\left(n_{obs}-3\right)\left(k-1\right)^2} \tag{H.5}$$

where,

$$a = (4g-6)\cdot(k-1) + (10-6g)\cdot S1 \tag{H.6}$$

$$b = (2g-4)\cdot k^2 + 8T\cdot k + (2g-14T-4)\cdot S1 - 8T + 4g - 6 \tag{H.7}$$

$$c = (6T+2g-2)\cdot k^2 + (4T-4g+6)\cdot k + (2T-6)\cdot S1 + 4T \tag{H.8}$$

$$d = (2T+6)\cdot k^2 - 4T\cdot k \tag{H.9}$$

$$S1 = \sum_{i=1}^{k}\frac{1}{n_i} \tag{H.10}$$

$$T = \sum_{i=1}^{n_{obs}-1}\frac{1}{i} \tag{H.11}$$

$$g = \sum_{i=1}^{n_{obs}-2}\sum_{j=i+1}^{n_{obs}-1}\frac{1}{\left(n_{obs}-i\right)\cdot j} \tag{H.12}$$

The critical value of the Anderson-Darling test is given by Eq. (H.13).

$$ADC = 1 + \sigma_n\cdot\left[1.645 + \frac{0.678}{\sqrt{k-1}} - \frac{0.362}{k-1}\right] \tag{H.13}$$

If $ADC > ADK$, it can be concluded the data are drawn from a similar population.

H.3 Maximum Normed Residual (MNR) test

Outliers are often erroneous data values that are much higher or lower than other observations in a group of data. Outliers may be due to a defective specimen, clerical error etc. It is important to check for outliers in a data set as they have a significant influence on the statistical analysis. MNR test method is used to check for outliers in a data set.

Suppose x_1, x_1, ..., x_n denote the observations in a data set of size n. The MNR test statistic is given by Eq. (H.14).

$$MNR = max\left(\frac{|x_i - \bar{x}|}{s}\right) \tag{H.14}$$

where $\bar{x}$ and s are the mean and standard deviation of the data set.

The critical value for the data set is given by Eq. (H.15).

$$C = \frac{n-1}{\sqrt{n}} \cdot \sqrt{\frac{t^2}{n-2+t^2}} \tag{H.15}$$

where t is the $[1-\alpha_{tdis}/\,(2n)]$ quantile of the t-distribution with $n-2$ degrees of freedom and α_{tdis} is the significance level. The recommended value of α_{tdis} for this tests is 0.05.

If $MNR > C$, it can be concluded that there are no outliers in the data set, otherwise, the observation with the largest $|x_i - \bar{x}|$ is declared as an outlier. Subsequently, the value is discarded from the data set, and, the MNR test method is applied again till there are no outliers in the data set. The mean, standard deviation and critical value during the j^{th} screening of the data set is calculated using a sample size of $n-j-1$.

H.4 Weibull distribution

Weibull distribution is a 2-parameter probability distribution where the probability that a random observation in a population lies between c and d (0<c<d<∞) is defined by Eq. (H.16).

$$e^{[-(c/\beta)^{\alpha}]} - e^{[-(d/\beta)^{\alpha}]} \tag{H.16}$$

H.4.1 Shape and scale parameters

The shape and scale parameters of a Weibull distribution are estimated by Eq. (H.17) and Eq. (H.18) respectively.

$$\frac{n}{\alpha} + \sum_{i=1}^{n} \ln x_i - \left(\frac{n}{\sum_{i=1}^{n} x_i^{\alpha}}\right) \cdot \sum_{i=1}^{n} x_i^{\alpha} \cdot \ln x_i \tag{H.17}$$

$$\beta = \left(\frac{\sum_{i=1}^{n} x_i^{\alpha}}{n}\right)^{\frac{1}{\alpha}} \tag{H.18}$$

H.4.2 Goodness-of-fit test

The Anderson-Darling goodness-of-fit tests is used to compare the cumulative distribution function of a probability distribution with the cumulative distribution of the data. The test computes an Observed Significance Level (OSL) which is the probability of obtaining a value of the test statistic which is atleast equal to the corresponding value obtained from the probability distribution to which the data is fitted. If OSL>0.05, it can be concluded that the data comes from the probability distribution to which it is fitted.

Let,

$$z_i = [x_i/\beta]^{\alpha} \tag{H.19}$$

for i = 1,2,3....n.

The Anderson-Darling test statistic is given by Eq. (H.20).

$$AD = \sum_{i=1}^{n} \frac{(1-2i)}{n} \left[\ln\left[1 - e^{-z_i}\right] - z_{n+1-i}\right] \tag{H.20}$$

The OSL is given by Eq. (H.21)

$$OSL = 1/\left\{1 + e^{[-0.1+1.24\ln(AD^*)+4.48AD^*]}\right\} \tag{H.21}$$

where,

$$AD^* = \left(1 + \frac{0.2}{\sqrt{n}}\right) \cdot AD \tag{H.22}$$

If OSL>0.05, it can be concluded that the data can be fit to a Weibull distribution.

H.4.3 A and B basis values

The B basis value for a Weibull distribution is given by Eq. (H.23).

$$B_{basis} = \hat{q} \cdot \exp\left\{\frac{-V}{\alpha \cdot \sqrt{n}}\right\} \tag{H.23}$$

where,

$$\hat{q} = \beta \cdot (0.10536)^{1/\alpha} \tag{H.24}$$

The value of V can be found in military handbook MIL-HDBK-17-1F [40].

The A_{basis} is estimated by Eq. (H.23), and, the value of $\hat{q}$ is given by Eq. (H.25).

$$\hat{q} = \beta \cdot (0.01005)^{1/\alpha} \tag{H.25}$$

H.5 Levene's test

As mentioned in Section 3.4, data pooling implicitly assumes that the variability across test conditions are negligible. Hence, Levene's F test has to be performed to check if variances across test conditions are equal.

The data is transformed according to Eq. (H.26)

$$w_{ij} = |x_{ij} - \tilde{x}_i| \tag{H.26}$$

where w_{ij} is the transformed data value of the j^{th} observation in the i^{th} group, x_{ij} is the original data value of the j^{th} observation in the i^{th} group and $\tilde{x}_i$ is the median of the i^{th} group.

The F test statistic is calculated by Eq. (H.27).

$$F = \frac{\sum_{i=1}^{k} n_i \cdot (\bar{w}_i - \bar{w})^2 \,/\, (k-1)}{\sum_{i=1}^{k} \sum_{j=1}^{n_i} (w_{ij} - \bar{w}_i)^2 \,/\, (n-k)} \tag{H.27}$$

where $\bar{w}_i$ is the mean of n_i observations in the i^{th} group and $\bar{w}$ is the mean of all n_{obs} observations and k is the number of groups.

If F is greater than the tabulated F-distribution quantile, it can be concluded that the variability across test conditions are significant, and, cannot be neglected. The tabulated F-distribution quantile is given by $1 - \alpha_{ftest}$ quantile of the F-distribution having numerator, $k-1$, and, denominator, $n-k$ degrees of freedom. The value of α_{ftest} for F-test is 0.05.

H.6 Data pooling results

Table H.1 shows that data pooling test statistic results of the tensile and compressive strengths.

Table H.1: Data pooling tests statistic results

	Compression	Tension
Results of k-sample Anderson-Darling test		
$AD_{calculated}$	0.582	0.386
$AD_{critical}$	1.76	1.75
Same population?	Yes	Yes
Results of equality of variances test		
$F_{calculated}$	0.747	0.485
$F_{critical}$	3.17	3.23
Variances equal ?	Yes	Yes

Since the test data for tension and compression pass the k-sample Anderson-Darling and equality of variances tests, it can be concluded that the data can be pooled.